Europa-Universität Flensburg

Development of a Lightweight Hydraulic-Pneumatic Flywheel for Wind Turbine Rotors

---

Doctoral thesis submitted in fulfilment of the requirements for the
degree of Doctor of Philosophy (Ph.D.)

at the
Interdisciplinary Institute for Environmental, Social and Human Sciences
Department of Energy and Environmental Management

by
Laurence Alhrshy

Flensburg
25 April 2024

Reviewers: Prof. Dr. Torsten Faber

               Prof. Dr. Bodo Fiedler

Supervisor: Prof. Dr. Clemens Jauch

Abstract

With an increase in the role that renewable energy resources have to play in power generation, wind turbines, as one of the most important renewable energy resources, have to serve the increasingly variable demands of the grid. Some of these demands cannot be satisfied with the standard control mechanisms of state-of-the-art wind turbines. In this thesis a hydraulic-pneumatic flywheel in a wind turbine rotor is presented as a mechanism that in addition to its various grid services, can also reduce the mechanical loads on the structure of a wind turbine. A hydraulic-pneumatic flywheel functions by varying the inertia of the rotor blades by moving a fluid mass between a piston accumulator near the blade root and one or more piston accumulators near the blade tip. However, evaluating the impact of such a flywheel on the wind turbine behaviour faces two main challenges: on the one hand, the installation of a flywheel into rotor blades increases the weight of the blades, and on the other hand, current state-of-the-art load simulation tools for wind turbines cannot simulate variable blade inertia. This thesis deals with these challenges in two main areas: Firstly, a flexible lightweight design of the flywheel is developed. This design enables the piston accumulators to be bent when the rotor blade bends. The bending capability of this design allows piston accumulators to be integrated into the support structure of the rotor blade. Consequently, the piston accumulator can substitute part of the material used in the spar caps of the blade, i.e., they can take over some of the loads, which would otherwise have to be borne by the original support structure of the blade. This enables the flywheel to be installed into the rotor blades without making the wind turbine significantly heavier. Secondly, three methods are presented for the implementations of variable blade inertia in three structural-dynamics models of load simulation tools of wind turbines. This enables these tools to simulate the dynamic behaviour of a wind turbine with an integrated flywheel in its rotor blades.

Acknowledgments

List of Publications

This thesis is based on the content of four peer-reviewed journal articles. These articles were published during the course of this Ph.D. project. In this thesis, a concise description of the problem definition, the methodology, the step-by-step approach leading to the solutions of the problems, and the resulting outcomes are provided. Consequently, this thesis provides essential information required for a comprehensive understanding of the project and its outcomes. For the sake of convenience, the four articles listed below are referred to in the text with the citing style of, e.g., "Publication 1". The four publications are provided in full in the Appendix.

Publication 1

Alhrshy, L.; Jauch, C.; Kloft, P. Development of a Flexible Lightweight Hydraulic-Pneumatic Flywheel System for Wind Turbine Rotors. Fluids 2020, 5, 162, doi:10.3390/fluids5040162.

Publication 2

Alhrshy, L.; Jauch, C. A Resource-Efficient Design for a Flexible Hydraulic-Pneumatic Flywheel in Wind Turbine Blades. J. Phys.: Conf. Ser. 2022, 2265, 032018, doi:10.1088/1742-6596/2265/3/032018.

Publication 3

Alhrshy, L. Implementation of Variable Blade Inertia in OpenFAST to Integrate a Flywheel System in the Rotor of a Wind Turbine. Energies 2021, 14, 2783, doi:10.3390/en14102783.

Publication 4

Alhrshy, L.; Lippke, A.; Jauch, C. Variable Blade Inertia in State-of-the-Art Wind Turbine Structural-Dynamics Models. Energies 2023, 16, 6061, doi:10.3390/en16166061.

Inhalt

1. Introduction

The utilization of renewable energy resources is significantly increasing in order to reduce the impact of climate change. Wind turbines are one of the most important renewable energy sources and have an important role to play in power generation. They do, however, have to serve the increasingly variable demands of the grid. Some of these demands cannot be satisfied with the standard control mechanisms of state-of-the-art wind turbines. A hydraulic-pneumatic flywheel in a wind turbine rotor [1,2] is one mechanism which, in addition to its various grid services, can also reduce the mechanical loads on the structure of a wind turbine [3].

The hydraulic-pneumatic flywheel functions by moving a fluid mass between a piston accumulator in the blade root and one or more piston accumulators near the blade tip. Figure 1 shows the components of such a flywheel with only one piston accumulator in the blade tip. To charge the hydraulic-pneumatic flywheel at any arbitrary rotor speed, electrically-driven pumps move the fluid to the blade tip. The hydraulic-pneumatic flywheel is discharged by means of compressed nitrogen, which is stored in containers in the blade body.

The general idea of the hydraulic-pneumatic flywheel is based on the inertia variation of wind turbine rotor blades by shifting a fluid between the tank and the piston accumulators [2]. Kinetic energy is stored or released by varying the inertia of the rotor blades. This allows a certain variation of the electrical power of the wind turbine, independent of the prevailing wind conditions [1]. Additionally, and most importantly, the eigenfrequencies of the rotor blades, and thus, the drive train and the tower of the wind turbine can be varied by the flywheel [3,4]. The idea of the hydraulic-pneumatic flywheel was given an excellent innovation award at the Schleswig-Holstein ideas competition in 2016 [5].

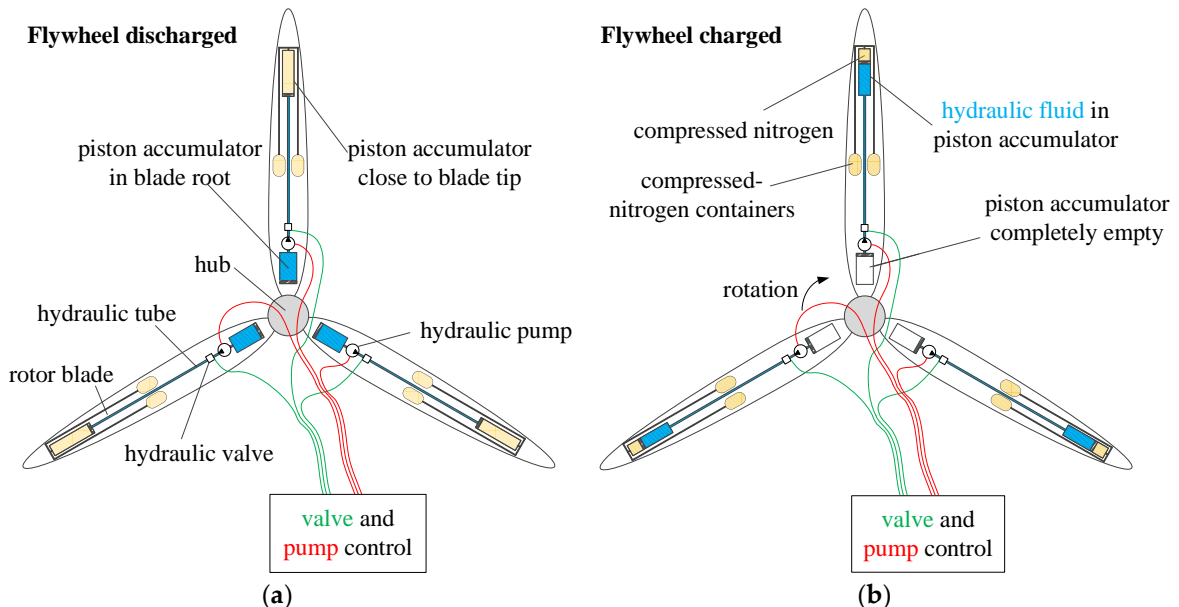*Figure 1: Simplified sketch of the hydraulic-pneumatic flywheel: (a) flywheel in discharged state, and (b) flywheel in charged state.*

Since 2014 the concept of incorporating a flywheel in a wind turbine's rotor has been developed at the Wind Energy Technology Institute (WETI) of Flensburg University of Applied Sciences, Germany. The initial proposal for a flywheel had solid masses in each blade

connected by a spiral spring to the blade tip[1]. In order to improve the feasibility and the response of this flywheel to the dynamic behaviour of rotor blades, a further proposal was made to replace the solid masses and spiral spring with a hydraulic-pneumatic flywheel containing steel piston accumulators [2]. The steel piston accumulators would have been heavy, rigid and unbendable. The configuration of the unbendable steel piston accumulators of the hydraulic-pneumatic flywheel in terms of their geometry, position and number was previously proposed so as to allow the blades to bend without bending the piston accumulators [6]. Due to this restriction, several desirable positions of the steel piston accumulators in the blade would not be feasible. Furthermore, the addition of mass at the blade tip would cause significant increases in ultimate loads as well as in fatigue loads of all wind turbine components, even when the flywheel is fully discharged and not in operation [7].

Previous mechanical load simulations to analyse the impact of a flywheel on wind turbine components could only be done under two conditions: the flywheel is either fully charged or fully discharged [7]. This is due to the fact that state-of-the-art load simulation tools of wind turbines are unable to represent variable blade inertias as they happen in a flywheel, without changing the source code of these tools. Initially, a First Eigenmodes simulation model of a wind turbine with variable blade inertias was developed to enable the design of control algorithms [8]. The model was implemented in Matlab/Simulink and consisted of different subsystems, which described the main components of a wind turbine. Since the goal of this model was to facilitate quick simulations, the description level of the wind turbine components was very simple, e.g., rotor blades and tower consisted of only two mass points. In the case of the tower, this leads to only two degrees of freedom. The rotor blades were represented with three degrees of freedom. Furthermore, the geometrical and the aerodynamical properties of the blade were simplified in the form of a torque coefficient lookup table. Since 2020, a more advanced version of the First Eigenmodes simulation model has been available online [9]. The upgraded version includes, inter alia, the model of an electrically driven hydraulic pump.

This Ph.D. project deals with two research questions:

1- Which mechanical properties should a flywheel within a wind turbine's rotor blades have without making them significantly heavier?
2- How can the dynamic behaviour of a flywheel be implemented in state-of-the-art load simulation tools in order to analyse the impact of the flywheel on the wind turbine components?

The answers to these questions are investigated in the following sections. Section 2 discusses the design of a flexible lightweight piston accumulator for its application in a hydraulic-pneumatic flywheel in a wind turbine rotor. Section 3 presents a design method that incorporates the flexible lightweight piston accumulators of the flywheel in the blade support structure. Section 4 describes the implementation of variable blade inertia in state-of-art load simulation tools of wind turbines

2. Development of a Flexible Lightweight Hydraulic-Pneumatic Flywheel for Wind Turbine Rotors (Publication 1)

As most conventional hydraulic piston accumulators are made of steel, the initial design of the piston accumulator for the flywheel was made of steel, too. This causes the additional stationary masses of the flywheel to be very large, which increases the total mass of the rotor blade enormously. Moreover, conventional steel piston accumulators are not designed to bend as the rotor blade bends. Hence, in the initial design of the flywheel, the dimensions of the piston accumulators, and the location of the piston accumulators in the rotor blades, were chosen such that the piston accumulators never bend, even when the rotor blades are bent the most [6]. Because of these two disadvantages, conventional steel piston accumulators are less suitable for installation in the rotor blades of a wind turbine. Consequently, the intention of this Ph.D. project is to design a new piston accumulator for the flywheel, which is lighter than steel and allows the piston accumulator to bend whenever the rotor blade is bent. The challenge of bending a piston accumulator is to prevent it from getting stuck and to prevent gas leakages across the piston rings. The development of a flexible light weight hydraulic-pneumatic flywheel for wind turbine rotors is discussed in detail in Publication 1.

2.1. Specification of a flexible carbon fibre-reinforced plastic piston accumulator

The problems mentioned above were solved in cooperation with HYDAC Technology GmbH, Germany, who design flexible piston accumulators made of carbon fibre-reinforced plastic (CFRP). CFRP is advantageous because it is anisotropic, and hence, allows the design of components which have different properties in different directions. Furthermore, the use of CFRP should lead to a mass reduction compared to conventional steel piston accumulators. HYDAC, in cooperation with PRONEXOS, Netherlands, designed, manufactured, and tested several prototypes of a flexible CFRP piston accumulator with a metal liner on the inside of the CFRP cylinder.

In the process of manufacturing the CFRP cylinder, the anisotropic properties can be achieved by winding the carbon fibres in certain directions around the cylinder. Figure 2 provides a qualitative illustration of the different winding directions.
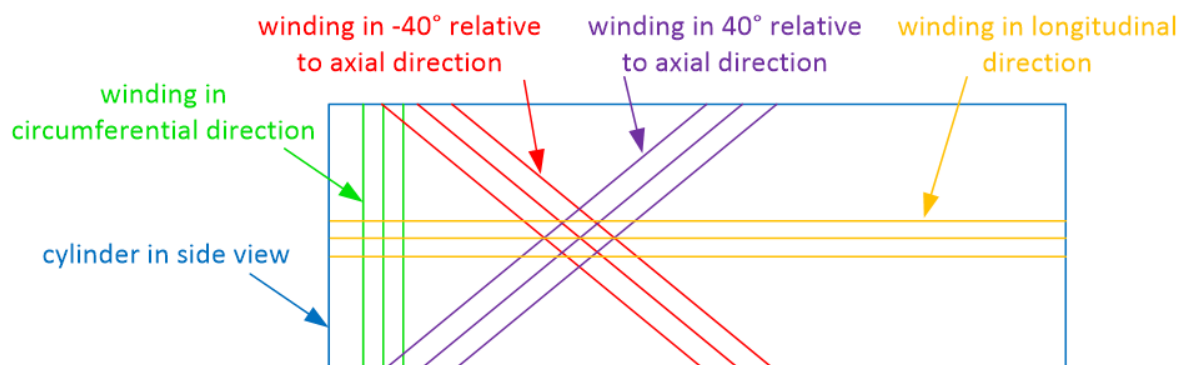

Figure 2: Illustration of the different winding directions that can be applied in the manufacturing process of a CFRP cylinder (the angles are only examples to illustrate the concept).

These winding directions provide the following properties of the laminate:

- Windings in the circumferential direction (90°) increase stiffness in the radial direction. An increase of carbon fibre layers in this direction limits the diameter increase that the cylinder exhibits in the case of internal pressure. Also, the cross-sectional shape is less prone to becoming elliptical in the case of longitudinal bending.

- Windings in the longitudinal direction (0°) increase the stiffness in the axial direction. The number of windings in the longitudinal direction has to be chosen such that these fibres rupture when the bursting pressure inside the cylinder is exceeded.

- Windings at a certain angle (positive and negative, except 0° and 90°), with respect to the longitudinal axis, add to stiffness in both the radial and axial direction, to an extent that depends on the angle. Most importantly, these windings add to the torsional stiffness of the cylinder (the angles shown in Figure 2 are only arbitrary examples for illustration).

The piston accumulator has to be designed such that its movement is not restricted when it bends within the rotor blade. At the same time, the piston has to reliably separate gas from fluid, i.e., the piston rings must not get damaged from the bending of the cylinder. These properties are achieved by making the piston from three flexibly-connected discs, see Figure 3.

(**a**)   (**b**)
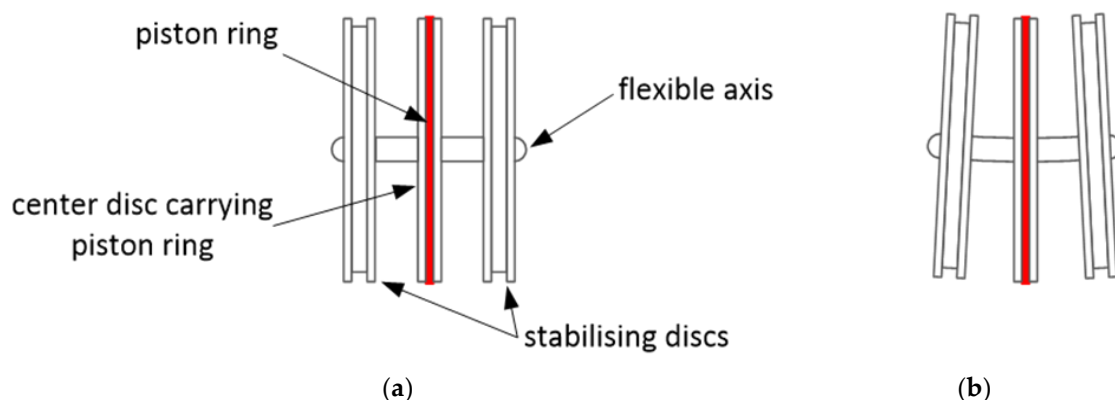
*Figure 3: Flexible piston (**a**) with the names of the components and (**b**) in a bent state.*

The outer discs (stabilising discs) prevent the piston from tilting. The centre disc carries the piston ring, and therefore, separates the gas chamber from the fluid chamber. The three discs are connected to each other via a flexible rod, which can be bent easily when the cylinder around the piston is bent. HYDAC has recently developed a flexible piston with only two discs.

2.2. Masses and load comparisons of steel and CFRP flywheels

The mass and load comparisons between the conventional and the flexible CFRP piston accumulators are limited to three relevant flywheel configurations. These represent the largest, the medium and the lowest impact on the mechanical loads [7]. The considered flywheel configurations are called "types" and are identified with Roman numerals, as introduced in Hippel et al. [6].

Table 1 and Figure 5 compare the properties and masses of both the CFRP and conventional steel piston accumulators for three flywheel types. These types represent the most suitable installation positions of the tip piston accumulators along the blade, see Figure 4.
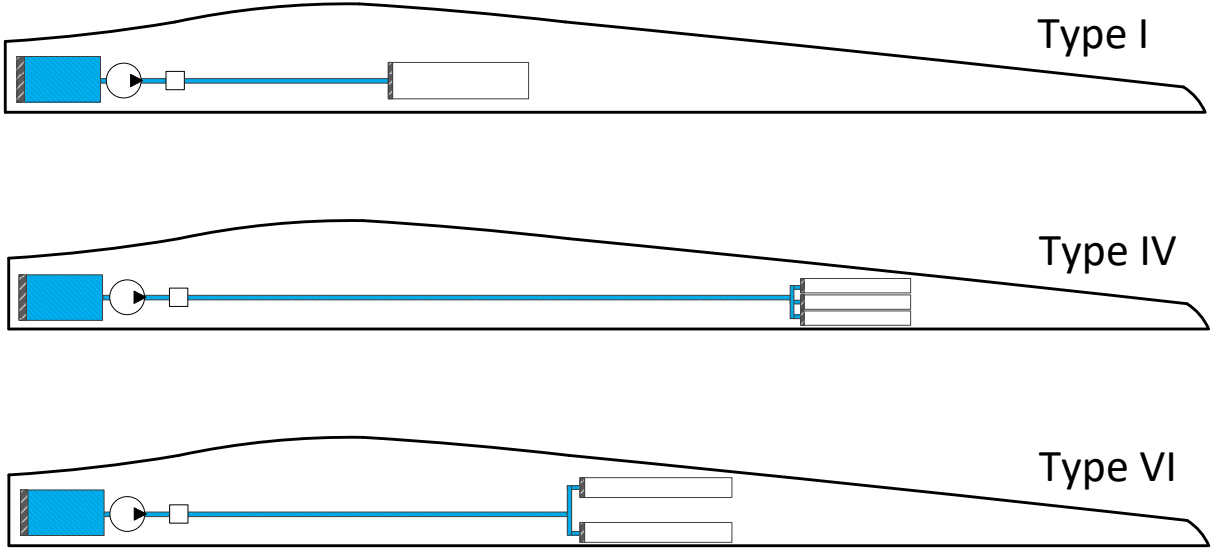
Figure 4: Simplified image of the flywheel types I, IV, and VI.

Table 1: Properties of the CFRP and the conventional piston accumulators of the three flywheel types.

Flywheel types	No. of tip ac.	Rotor radius	Inner diameter	Total length	Wall thickness CFRP	Wall thickness Steel	Material CFRP	Material steel
-	-	M	mm	mm	mm	Mm	-	-
Type I	1	40.01	577	5477	4.24	3	carbon fibre Toho tenax STS40 and S335 steel liner	34CrMo4 steel
Type IV	3	Each at 61.6	224, 209, and 149	5966, 5957, and 5920	Each 3.72	Each 3		
Type VI	2	Each at 46.6	443 and 241	5047 and 4923	Each 3.72	Each 3		

Figure 5 shows the mass reduction of the total stationary masses of the root and the tip piston accumulators for the CFRP design compared to the conventional steel design, for all represented flywheel types.
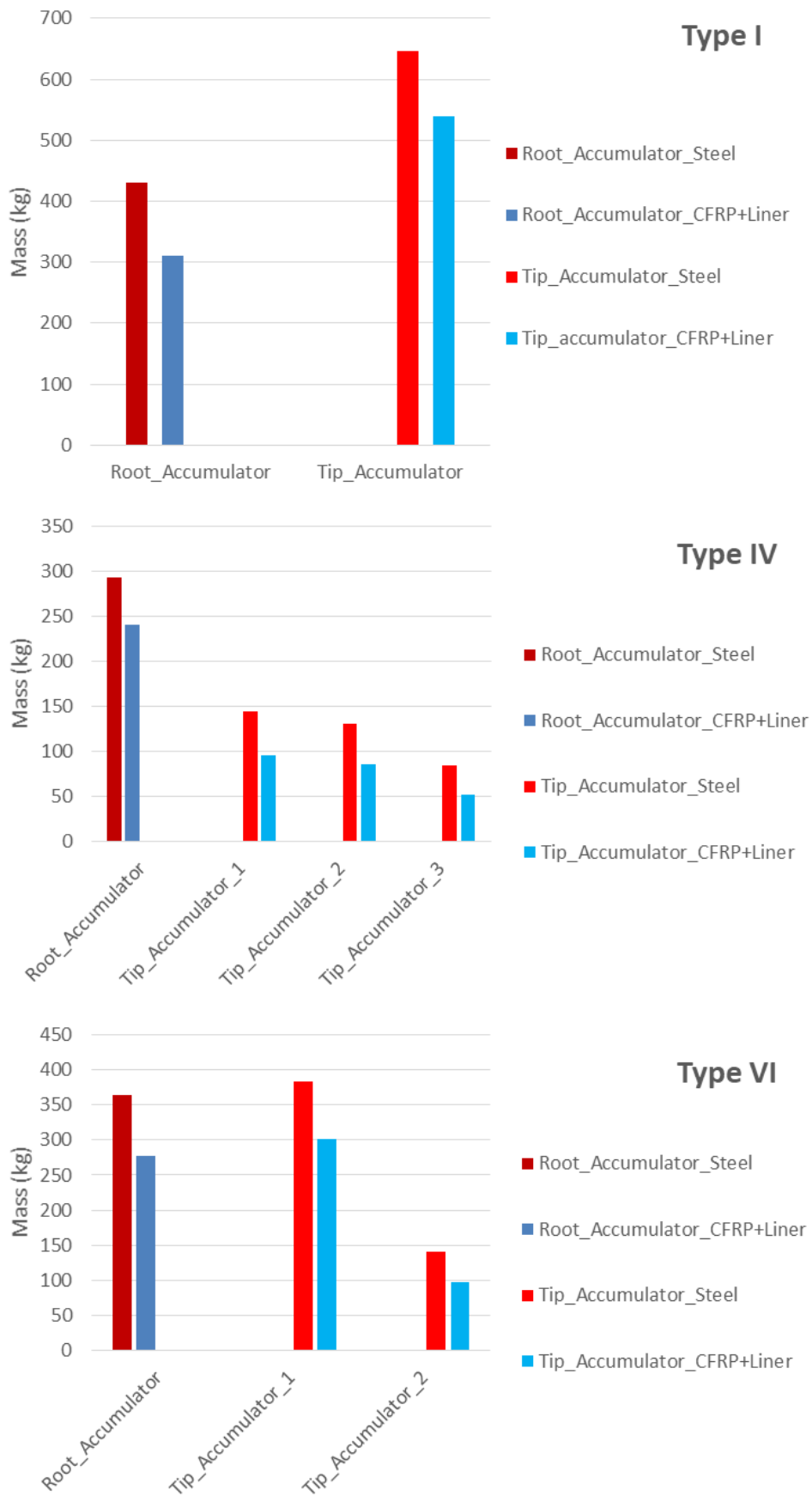
Figure 5: Mass comparison of blade tip and blade root piston accumulators from steel and from CFRP with steel liner for (a) type I, (b) type IV, and (c) type V I.

The load analysis presented in this section aims to quantify the effect of the mass reduction of the CFRP piston accumulators on the impact of the mechanical loads of the National Renewable Energy Laboratory (NREL) 5 megawatt (MW) reference wind turbine [10]. The quantification of loads is achieved firstly by computing the mechanical loads of the original wind turbine without a flywheel in order to obtain reference load values. Subsequently, load simulations are carried out for the wind turbine with a flywheel containing CFRP piston accumulators in the rotor blades as well as one with conventional steel piston accumulators. The deviations of the mechanical loads from the reference values illustrate the impact of the different flywheel designs on the mechanical loads of the wind turbine. For this analysis, the aeroelastic computer-aided-engineering tool FAST was used [11]. As mentioned in the introduction, at this stage, the methodology used to implement the variable behaviour of the flywheel in FAST considers the flywheel statically, i.e., the flywheel is either fully charged or fully discharged. These two scenarios were assessed for the three previously mentioned flywheel types I, IV and VI.

The change in ultimate loads that result from both designs of the flywheel are presented in Figure 6. This depicts the change in ultimate loads of the blades, the drive train, and the tower of the NREL 5 MW reference wind turbine as a percentage increase in bending moments. The charged and the discharged states of the flywheel with CFRP piston accumulators are represented in dark red and dark blue, respectively, whereas the charged and discharged states of the flywheel with conventional steel piston accumulators are shown in light red and light blue, respectively. Figure 5 shows that the increase in bending moments when both flywheel designs are in a charged state are greater than the bending moments when the flywheels are in a discharged state. The reason for this is that the fluid mass in the charged state is added to the stationary mass of the tip piston accumulator, where the lever arm of the gravitation force has a larger distance to the centre of rotation. Also, the larger distance to the centre of rotation leads to larger centrifugal forces created by the fluid mass. Due to the stationary mass reduction of the CFRP piston accumulator, the increase in bending moments of almost all flywheel types is lower for the CFRP design compared to the conventional steel design.

Figure 6: Comparison of changes in ultimate loads in (from top to bottom) blade root bending moment, bending moments at blade cuts, bending moments at tower top, bending moments at tower bottom, and bending moments at drive train, between steel piston accumulator and CFRP with metal liner piston accumulator for flywheel types I, IV, and VI in charged (red) and discharged (blue) state, both with respect to the ultimate loads of the original wind turbine without flywheel.

The first and the second graphs in Figure 6 show the bending moments at the blade cuts, SpnMLxB, and the tower cuts, TwHtML, where the maximum increase of these moments are indicated. The variable names are based on the conventions used in FAST [11].

The change in fatigue loads were analysed in a similar procedure to that used for ultimate loads. Fatigue analysis was performed twice (in charged and discharged states) for each flywheel design over the 20-year lifetime of the wind turbine. Figure 7 compares the change in fatigue loads for both flywheel designs at the rotor blade, the tower, and the drive train of the NREL 5 MW reference wind turbine. The light red and the light blue bars in Figure 7 represent the charged and the discharged states of the conventional design of the flywheel, respectively. The columns in dark red and dark blue represent the charged and the discharged states of the CFRP design of the flywheel, respectively. The change in fatigue-damage equivalent bending moment at the blade, the tower, and the drive train caused by the CFRP design of the flywheel are lower than that for the conventional steel design. This is due to the difference of the stationary masses between the CFRP design and the conventional steel design of the piston accumulators. For flywheel type IV, the fatigue equivalent bending moment at tower top in the discharged state and at tower bottom in charged and discharged states are slightly decreased for both flywheel designs. This can be traced to the low impact of type IV on the tower top and tower bottom during the simulation time of 20 years of operation.

Ultimate and fatigue failures were evaluated to ensure that there is no need for reinforcement in the original rotor blade design of the NREL 5 MW reference wind turbine. The failure evaluation in this study is based on the same methodology used by Hippel and Jauch [7], where the load simulation results were used to indicate ultimate and fatigue failures. The failure evaluation showed that neither ultimate nor fatigue failure of the rotor blade was caused by the presence of the conventional steel piston accumulator flywheel [7]. Figure 6 and Figure 7 show that the loads of the CFRP flywheel design are in general lower than those of the conventional steel flywheel design. This leads to the conclusion that the increase in ultimate and fatigue loads due to the installation of the CFRP flywheel design causes neither ultimate nor fatigue failure of the rotor blade, since the wind turbine model and the rotor blade design are the same for both load simulations. In this context, it is important to note that the evaluation of the ultimate and fatigue failures was performed using the 61.5 m rotor blade design developed by Brian R. Resor [12] and the results are only valid for this design. This design is known to be conservative as it makes the blades heavy and stiff.
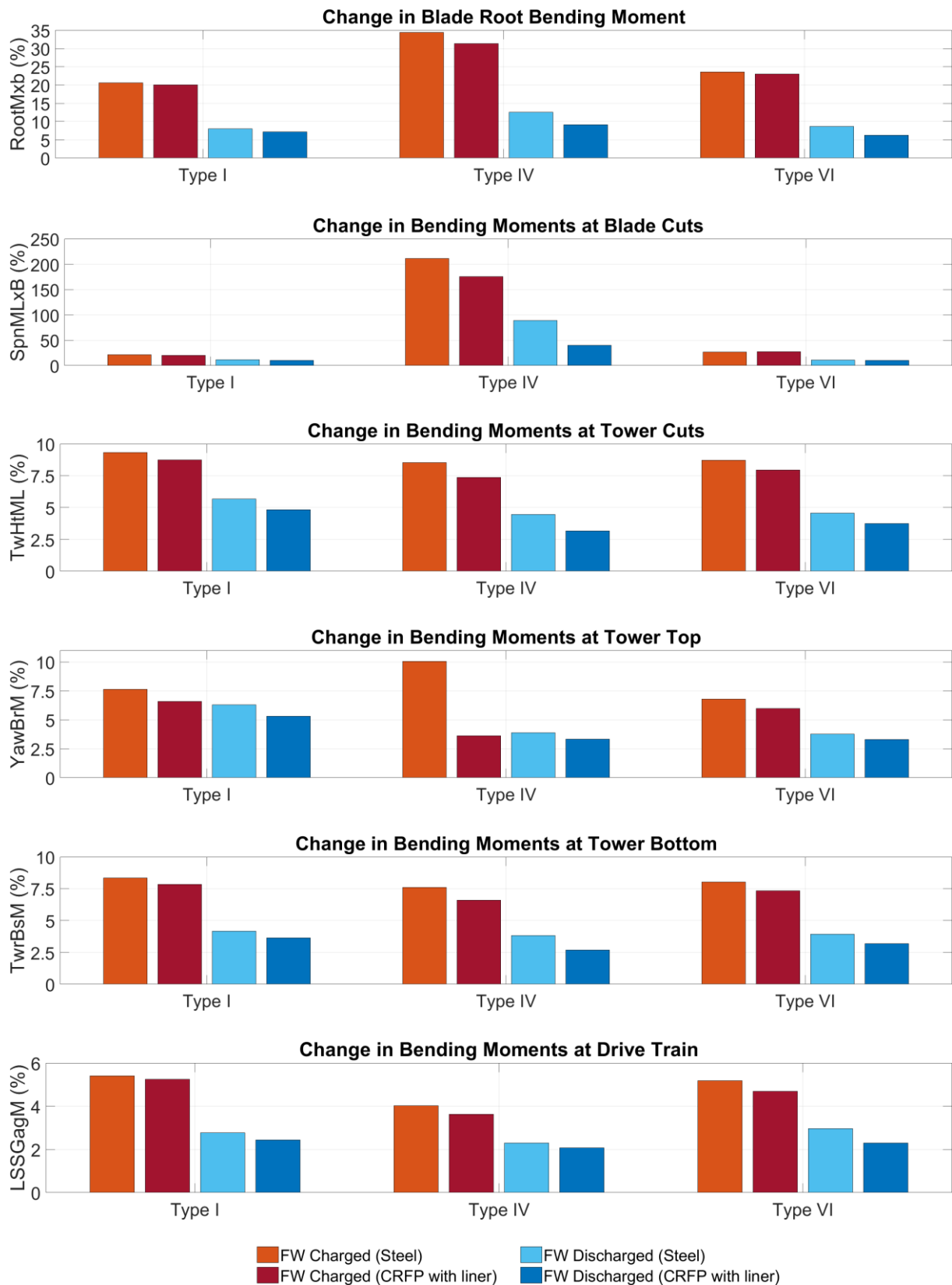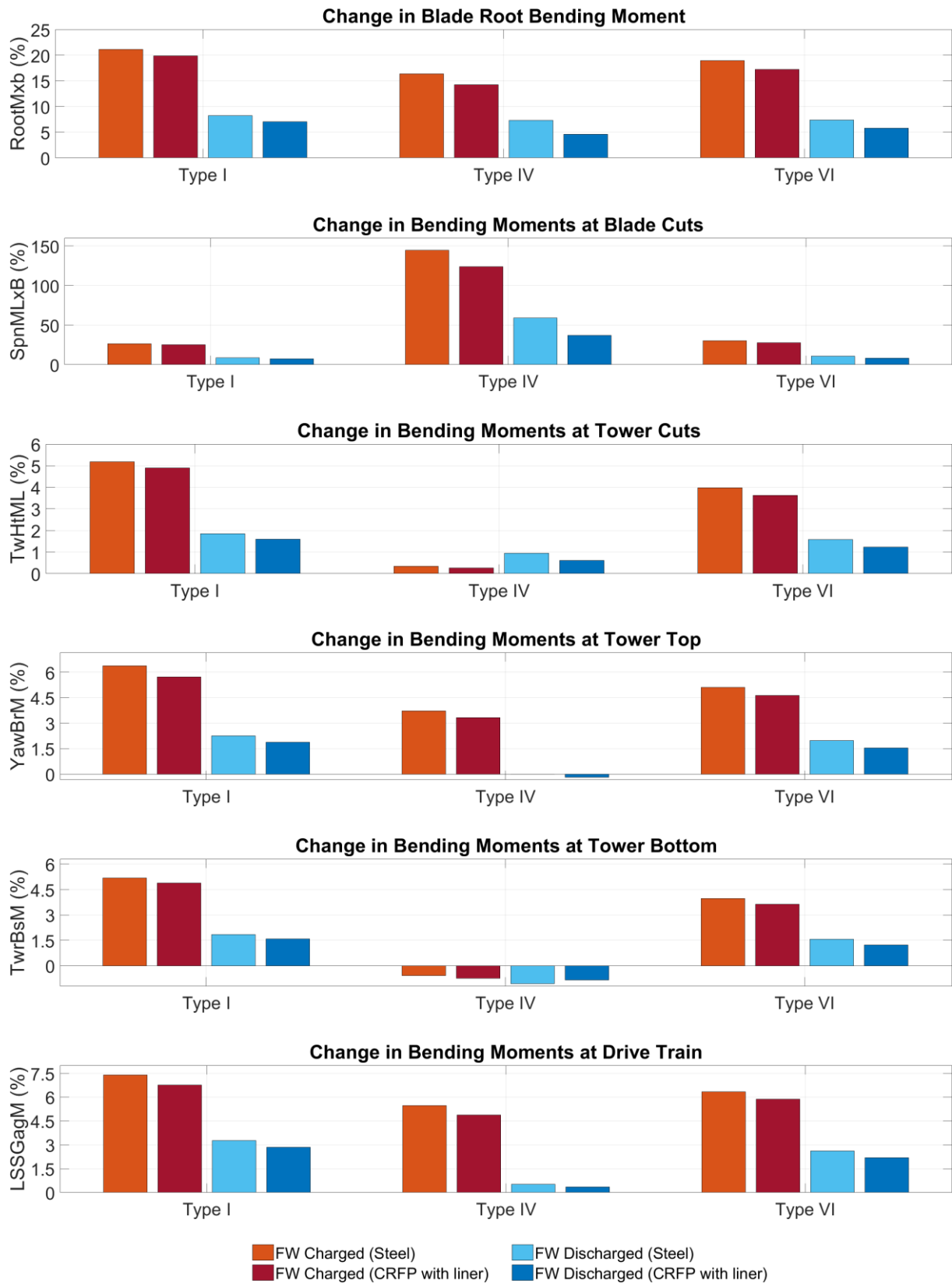
Figure 7: Comparison of changes in fatigue loads in (from top to bottom) blade root bending moment, bending moments at blade cuts, bending moments at tower top, bending moments at tower bottom, and bending moments at drive train, between steel piston accumulator and CFRP with metal liner piston accumulator for flywheel types I, IV, and VI in charged (red) and discharged (blue) state, both with respect to the ultimate loads of the original wind turbine without flywheel.

3. A Resource-Efficient Design for a Flexible Hydraulic-Pneumatic Flywheel in Wind Turbine Blades (Publication 2)

The load analyses in the previous section showed that the mechanical loads increased on all wind turbine components even when the flywheel is fully discharged. This is due to the additional stationary masses of the piston accumulator in the blade tips. As these piston accumulators are designed to be made of composite material and, more importantly, to be bendable, it is possible to incorporate them into the support structure of the rotor blade. The objective in this section is to minimize the additional masses by replacing parts of the blade spar caps with the tip accumulators of the CFRP flywheel. This allows the CFRP flywheel to be installed in the rotor blades without significantly increasing the masses of the blades. The information provided in this section is discussed in detail in Publication 2.

3.1. Incorporating the tip piston accumulator as a part of the blade support structure

To illustrate the effect on the blade structure of replacing spar caps material, Figure 8 provides a blade cross section before and after the modification. Due to the nature of the compact and heavy unidirectional composite material used for the spar caps to support the bending stiffness of the blade, the majority of the total mass of the blade is concentrated in the spar caps [12]. The piston accumulators and the blade spar caps are both made of composite materials, which makes material replacement homogenous. Therefore, it seems an obvious choice to replace unidirectional material of the spar caps rather than the foam or the balsa of the blade with material from the piston accumulator.
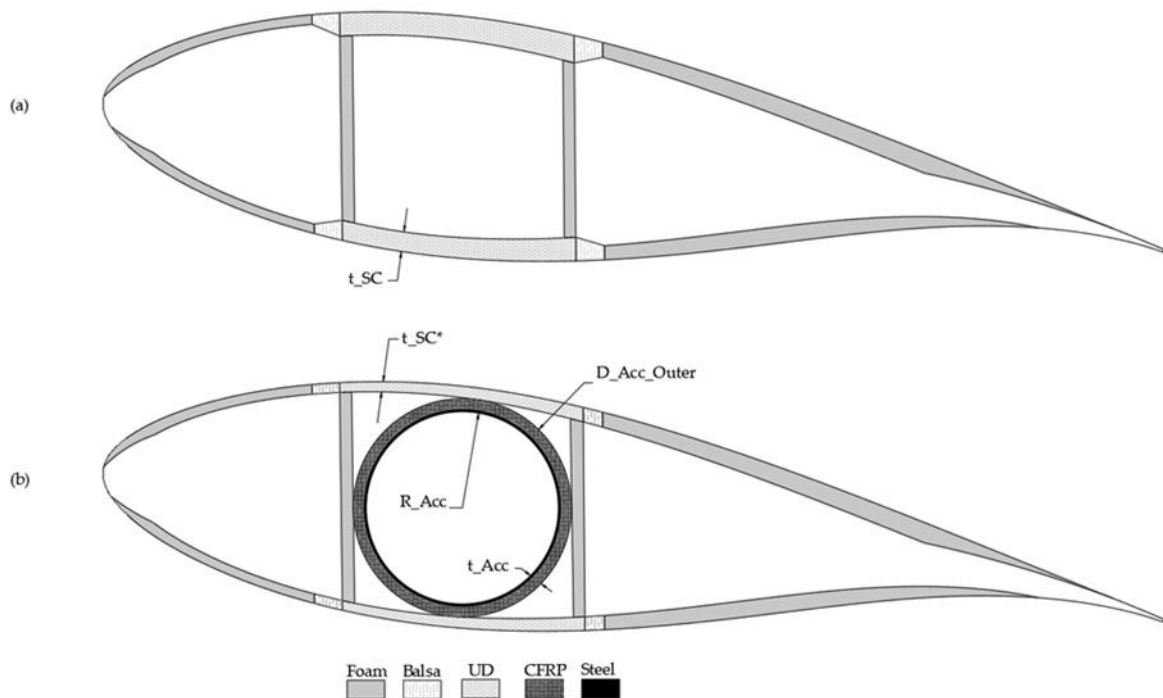
Figure 8: Schematic drawings of (a) initial blade cross-section without tip piston accumulator, (b) modified blade cross-section with tip piston accumulator.

In order to limit the inevitable increase in blade mass to a minimum, the spar cap thicknesses are decreased from t_SC to t_SC*. Figure 8 (b) shows the changes in the cross-sectional structure of the blade due to the installation of a piston accumulator with radius R_Acc and wall thickness t_Acc.

3.2. Configuration of the hydraulic-pneumatic flywheel

The methodology presented in this section is based on an algorithm which applies an iteration loop to acquire optimal flywheel configurations, see Figure 9. The installation radius of the flywheel piston accumulator, R, i.e. the outer radius where the flywheel piston accumulator is closest to the blade tip, is determined at the beginning of the algorithm. This allows for the determination of the available space at every installation radius, R, as the blade narrows towards its tip and the piston accumulator has a constant diameter over its complete length.
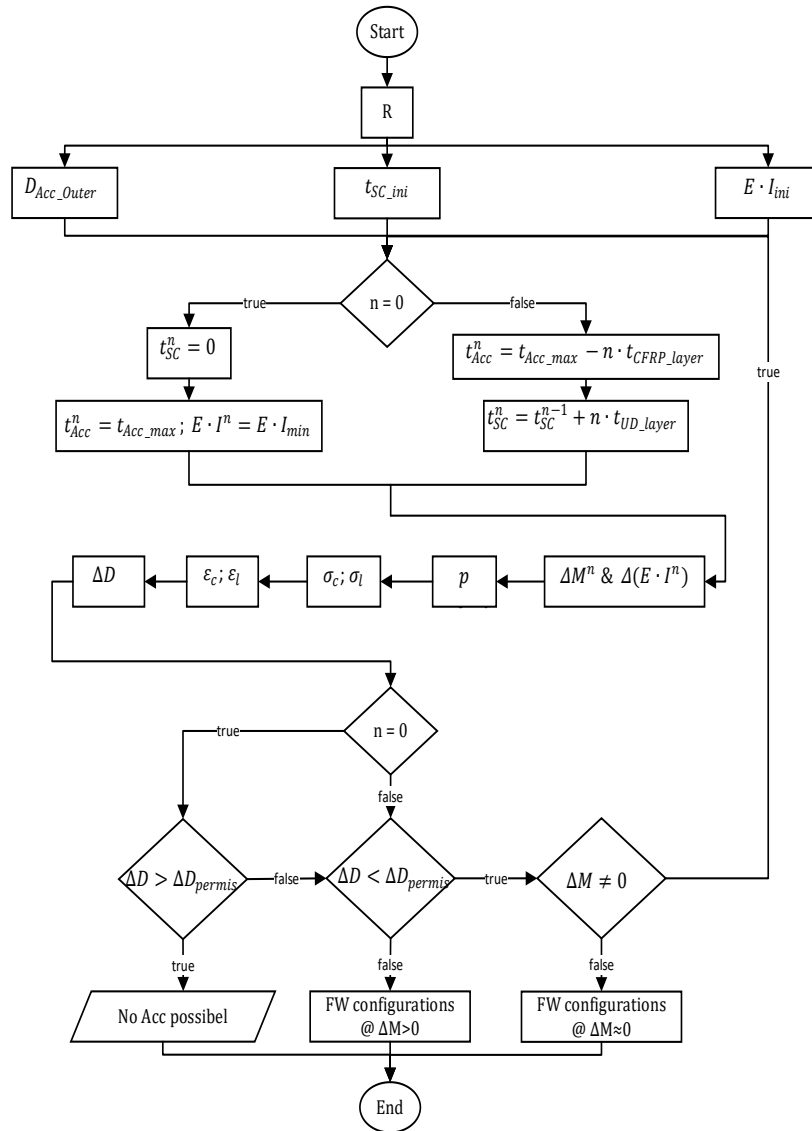
Figure 9: The iterative process for computing the minimum tip piston accumulator thickness and the resulting flywheel configurations.

Based on this radius, the piston accumulator outer diameter, D_{Acc_Outer}, the initial spar cap thickness, t_{SC_ini}, and the initial cross-sectional bending stiffness, $E \cdot I_{ini}$, in terms of Young's modulus, E, of the material and the initial moment of inertia I_{ini} are defined. Initially, the tip piston accumulator was designed to completely replace the spar caps in order to verify

whether a piston accumulator can be installed at this radius. For this initial condition, the maximum tip piston accumulator wall thicknesses. t_{Acc_max}, and the minimum cross-sectional binding stiffness, $E \cdot I_{min}$ were computed. The changes in the mass, M, and the bending stiffness, $E \cdot I$, of the modified cross-section of this initial piston accumulator were quantified in terms of ΔM^n & $\Delta(E \cdot I^n)$, where, n, is the iteration step. Subsequently, the calculated working pressure on the piston accumulator, p, was translated into a circumference stress, σ_c, and a longitudinal stress; σ_l, using Barlow's formula. These stresses were used to calculate the strains in circumferential direction, ε_c and in longitudinal direction, ε_l, based on classical laminate theory. The resulting circumference strain was transformed into an increase in the diameter of the shell of the piston accumulator, ΔD. It should be noted that ΔD should not exceed the permissible diameter increase, ΔD_{permis}, of 0.3 mm; otherwise, the piston accumulator would no longer be able to separate the gas from the fluid in the piston accumulator, i.e. gas from the gas chamber could leak into the fluid chamber and vice versa. In the iteration process, when the increase in diameter, ΔD, was lower than the permissible limit, and the change in the cross-sectional mass, ΔM, was not equal to zero, the wall thickness of the tip piston accumulator, t_{Acc}, was decreased, while the spar caps thickness, t_{SC}, was increased iteratively. This iteration was continued until one of the aforementioned conditions was met. The wall thickness of the piston accumulator and the thickness of the spar caps were modified depending on the thickness of a single layer of the CFRP and the unidirectional composite material. As a result, numerous flywheel configurations were derived, which differ in the length and positioning of the tip piston accumulator and fluid mass, as well as the impact on the cross-sectional bending stiffness of the blade.

To utilize the available space at every blade cross-section to the maximum possible extent, flywheel configurations with more than one piston accumulator are needed. The piston accumulators should have the same diameter to ensure that they behave identically when charging/discharging the flywheel. Moreover, to increase the change in the blade eigenfrequencies, the piston accumulators should be installed near the blade tip. Depending on the flywheel applications [13], the change in the blade eigenfrequencies can be actively used to detune the blade eigenfrequencies in order to mitigate fatigue from vibrations.

The concept presented in this work, which is to minimize the additional mass resulting from incorporation of piston accumulators, was applied to the AE 4.0-68.7 blade design. This blade was designed and developed by AEROVIDE GmbH, Germany. The thickness of the spar caps were reduced in order to keep the blade mass unchanged when the piston accumulators were installed. AEROVIDE performed a stress-strain analysis of the modified structure of the blade containing the piston accumulators. The results of the analysis showed that the strains at the blade sections where the piston accumulators were installed did not exceed 0.5%. This means that the steel liner of the piston accumulator must have a yield strength higher than 1000 megapascal, or the spar caps must be thicker at the sections where the piston accumulators have to be installed. Details about the impact of this concept on the mechanical properties of the AE 4.0-68.7 blade design can be found in Publication 2.

Further investigations on the flywheel will be based on the aforementioned algorithm, the utilization of the available space at every blade cross-section, and the increase in the change of the blade eigenfrequencies. The investigations will focus on flywheel configurations with

multiple piston accumulators that have the same diameter. A schematic drawing of a flywheel configuration with four identical piston accumulators is provided in Figure 10.
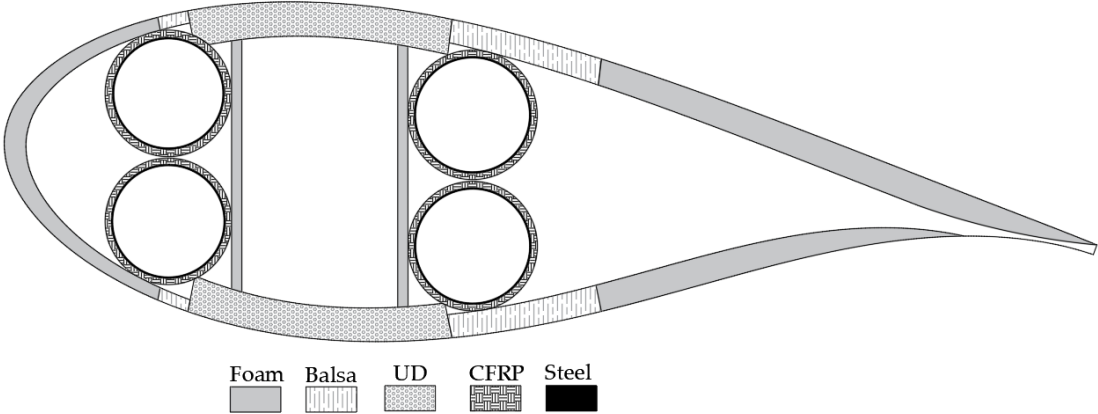

Figure 10: Schematic drawing of a flywheel configuration with four identical piston accumulators near the blade tip.

4. Implementation of variable blade inertia in state-of-the-art load simulation tools of wind turbine (Publications 3 and 4)

In order to analyse the impact of the flexible hydraulic-pneumatic flywheel on the vibratory behaviour of the wind turbine components, the dynamic behaviour of the flywheel should be first implemented in a load simulation tool. As currently all state-of-the-art load simulation tools for wind turbines are unable to represent variable rotor blade inertias as they happen in the flywheel, the dynamic behaviour of the flywheel cannot be represented without changing the source code of these load simulation tools. Therefore, all the previous mechanical load simulations, either for the conventional steel flywheel design [7] or for the flexible CFRP flywheel design in Publication 1, could only be done under two conditions: the flywheel is statically fully charged or the flywheel is statically fully discharged.

The implementation of variable blade inertia in aero-elastic codes of wind turbines has been developed at the WETI since 2014. Initially, a First Eigenmodes simulation model of a wind turbine was developed to enable the design of control algorithms[8]. A more advanced version of this model has been developed since 2020 [9]. As mentioned in the introduction, the method used in this model to describe the wind turbine components is very simplified. Consequently, this model does not provide an exact response of a wind turbine with variable inertias at different nodes along the blade length. To do this, a load simulation tool is required that can describe the structural dynamics of the rotor blades in more detail.

4.1. Implementation method of variable blade inertia in ElastoDyn (Publication 3)

ElastoDyn is a structural-dynamic model developed by NREL for horizontal-axis wind turbines [14]. This model is implemented within the aeroelastic modularization framework FAST [11]. ElastoDyn is based on Bernoulli-Euler beam theory and describes the mechanical properties of a rotor blade in greater detail than the First Eigenmodes simulation model. Just like the First Eigenmodes simulation model, ElastoDyn is free, publicly available, and well documented. ElastoDyn uses Kane's method [15] to set up equations of motion, which can be put into Newton's Second Law (see Equation 1).

$$F = m \cdot a$$
<div align="right">1</div>

Since the functioning of the flywheel is based on the variation of rotor blade inertias during wind turbine operation, this variation is translated in the source code of ElastoDyn by varying the blade element mass within a given simulation. The masses of the blade elements are stored in ElastoDyn blade input files as part of the blade's mechanical properties. The main challenge facing the implementation of blade elements with variable masses is that the blade's mechanical properties are used as time-invariant input parameters, which are applied only once at the model initialization and then erased directly afterwards. Moreover, the data type definition of the masses of the blade elements in the programming language of FAST does not allow any change in their value during the whole simulation time. All details provided in this section can be found in Publication 3.

The flowchart in Figure 11 shows the three stages of iterative solution of the aforementioned problems:
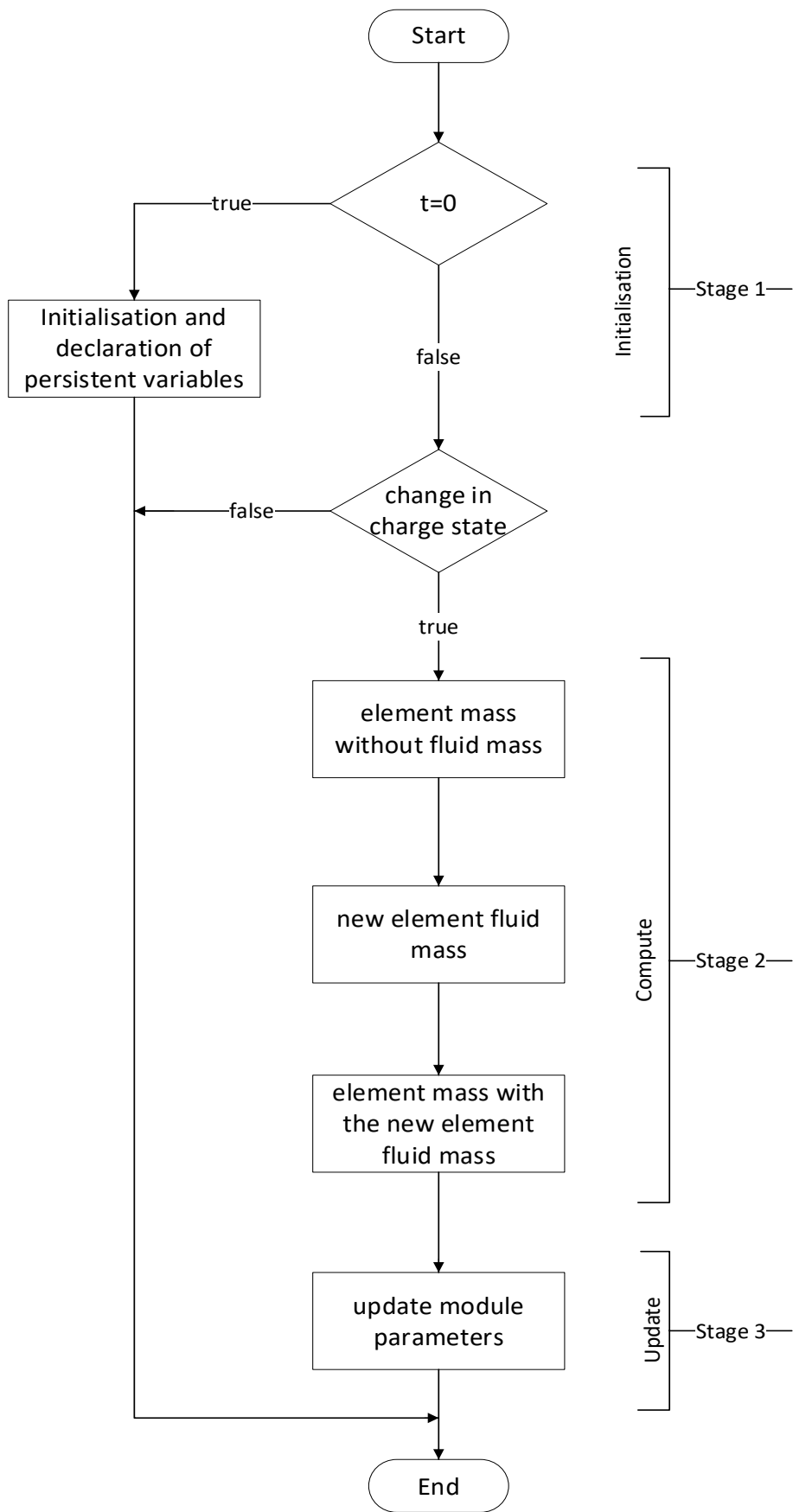
Figure 11: Iterative process for initializing, computing, and updating the change in a blade element mass, and their related parameters.

- Stage 1: As soon as the simulation starts in FAST at simulation time zero, the variables that declare the initial conditions of the flywheel are defined. The definition of these variables is based on the blade input parameters of ElastoDyn. These input parameters are erased after the initialization, whereas the flywheel variables are still accessible at any time during the simulation.

- Stage 2: This stage is responsible for the change in the masses of the blade elements with regard to the charge-index-factor (K). The charge-index-factor determines how much fluid mass must be shifted in a particular blade. At first, the masses of the blade elements are calculated without the additional fluid mass. Subsequently, the new fluid mass of each blade element is calculated depending on the current value of K. Finally, the newly calculated fluid mass is added to the corresponding blade element mass. The initiation of this stage is conditional on a change in K, i.e., the value of K_t from the current simulation step must not be equal to K_{t-1}, the value from the previous simulation step. Such a condition helps to speed up the simulation when there is no change in the charge state of the flywheel in any blade.

- Stage 3: After changing the masses of the blade elements in stage 2, all the parameters that are related to the masses of the blade elements must be updated.

These three stages are translated in the programming language of FAST as additional subroutines, which are applied in the main dynamic calculation of ElastoDyn.

The additional loads from the flywheel due to the stationary change of the masses of the blade elements are intrinsically included in the kinematics and kinetics of ElastoDyn. However, the load resulting from the portable mass between two blade elements at a given time is not considered in the structural dynamics of ElastoDyn as variations in the inertia of the rotor do not happen in state-of-the-art wind turbines. This load has been explained by Jauch [9] as an additional torque, which results from the change in angular momentum. The law of conservation of angular momentum presented in Equations 2 to 4 describes the fact that a torque, T, occurs if the angular momentum, L, changes, in order to keep the kinetic energy, E_{kin}, constant.

$$E_{kin} = \frac{1}{2} \cdot J \cdot \omega^2 \qquad\qquad 2$$

$$L = J \cdot \omega \qquad\qquad 3$$

$$T = \frac{dL}{dt} \qquad\qquad 4$$

where J is the mass moment of inertia, and ω is the rotational angular speed.

Equation 5 expresses the flywheel torque, T_{FW_bl}, in a given blade in terms of the change in the flywheel inertia in a rotor blade, $\frac{d}{dt}(J_{FW\_bl})$.

$$T_{FW\_bl} = -\frac{d}{dt}(J_{FW\_bl}) \cdot \omega \qquad\qquad 5$$

The inertia of the flywheel in a given blade, J_{FW_bl}, changes if the centre of gravity, R_{var}, of the flywheel fluid, m_{fluid}, changes, see Equation 6.

$$J_{FW\_bl} = R_{var}^2 \cdot m_{fluid} \qquad\qquad 6$$

4.2. Application of the flywheel in ElastoDyn for correction of rotor imbalance

This section provides an example of the application of the flywheel in ElastoDyn for rotor imbalance correction. Rotor imbalance in a wind turbine may be the result of aerodynamic imbalances, which could be caused by pitch misalignment of one blade with respect to the other blades, or may be the result of mass imbalance due to a number of causes, for example, ice accretion, blade damage, or poor blade manufacturing tolerances [16]. Vibrations resulting from rotor imbalances significantly affect wind turbine fatigue, which may reduce the efficiency and operational life of a wind turbine. Rotor imbalance correction methods are generally based on the adjustment of the pitch angle of wind turbine rotor blades. This, however, leads to a reduction in the power output of the wind turbine. Since a flywheel has the ability to vary the blade inertia, this advantage can be applied to correct rotor mass imbalances without the need to adjust the pitch angle. The simulation scenario presented in Figure 12 uses the flywheel to correct a mass imbalance in the rotor of the NREL 5 MW reference wind turbine. The rotor mass imbalance is simulated by adding an additional mass of circa 191 kg in blade 1 at a span location of 39.8 m.
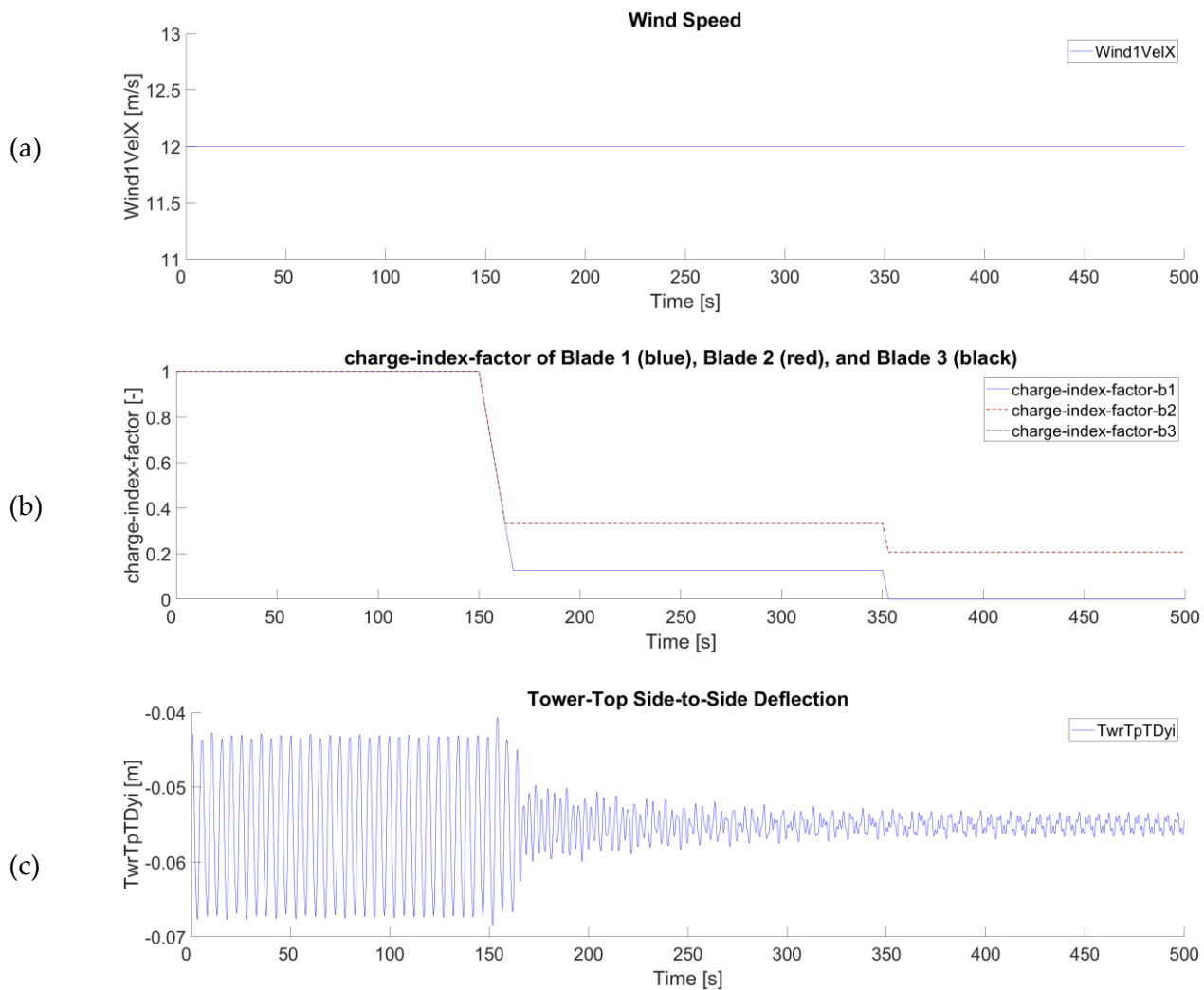
(a)

(b)

(c)

Figure 12: Impact of the flywheel on a tower-top side-to-side deflection by imbalance in the rotor blade.

During the whole simulation time, the wind speed remains constant at the rated value of 12 m/s. The flywheel is initially fully charged in the rotor and is discharged at different times in the three blades, see Figure 12 (b). Although the tip piston accumulator in blade 1 is fully discharged at 354 s, the tip piston accumulators in blades 2 and 3 are not completely discharged so that they keep the rotor balanced until the end of the simulation. The initial rotor imbalance is a 1p excitation, which excites the tower to a lateral vibration. Figure 12 (c) shows this vibration in terms of side-to-side deflection of the tower top, where the vibration amplitudes of the tower top side-to-side deflections are much greater within the period of the rotor imbalance than in the period after the imbalance correction at a simulation time of 167 s.

4.3. Implementation method of variable blade inertia in BeamDyn and HAWC2 (Publication 4)

The method used in ElastoDyn to implement the resulting forces from the fluid movement simplifies these forces by applying a total (accumulative) torque at the hub, as discussed in Publication 3. This simplification does not take the impact of the forces on the blade nodes into consideration. This inhibits several applications of the flywheel from being simulated, e.g. damping of in-plane vibrations of blades, and mitigation of excitations from gravitation and wind shear. Furthermore, ElastoDyn only supports beams constructed from isotropic material without mass or elastic offsets, without axial or torsional degrees of freedom and without shear deformation. For these reasons, it was obvious that the method of variable blade inertia had to be implemented in a more complex structural dynamics model of wind turbine rotor blades. The information provide in this section is discussed in Publication 4.

Two advanced structural dynamics models, HAWC2 [17] and BeamDyn [18], were chosen to compare and validate the implementation method of variable blade inertia. Both models utilize finite beam element theory to enable a very complex and advanced modelling method. This method utilises the nonlinear beam structural dynamics of the blade structure. The mechanical properties of several cross-sections of the blade are defined in these models by tabular mass and stiffness matrices, which are used in the numerical solution of the dynamic equations during a given simulation. In addition to the extensive description of the blade mechanical properties, a previous comparison of HAWC2 and BeamDyn had shown that both models are capable of computing accurate solutions for highly nonlinear effects [19]. The implementation concept for the flywheel is shown schematically in Figure 13 for a simple wind turbine simulation model with flywheel elements at one blade.
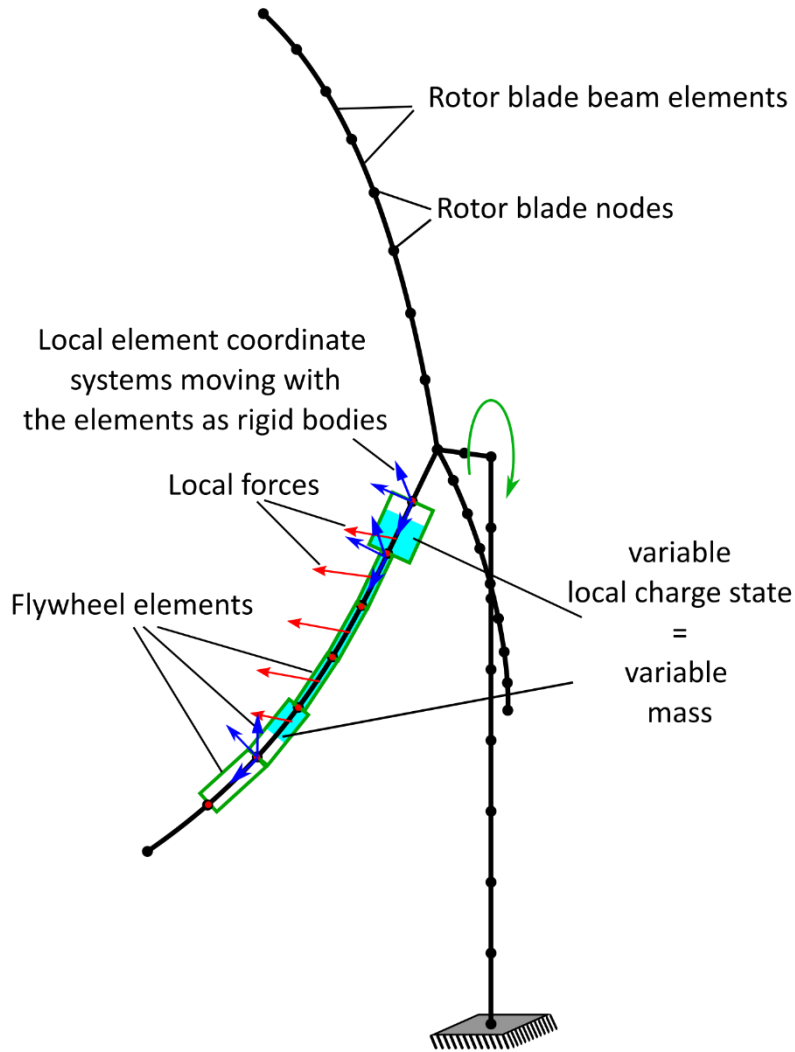
Figure 13: Schematic of a simple wind turbine simulation model with flywheel elements shown at one rotor blade.

Although the definition of beam elements in the HAWC2 and BeamDyn models is different, the mathematical description of the implementation of variable blade inertia itself is the same in both models. However, due to the differences in the program structure and the accessibility of the source codes of these models, two distinct implementation methods are required.

Similar to the charge-index-factor K used in ElastoDyn, the variation of blade inertia in HAWC2 and BeamDyn is based on the change in the global charge state of the tip piston accumulator, γ_{tip}. This control variable indicates whether tip piston accumulators are empty ($\gamma_{tip} = 0$), or either partly ($0 < \gamma_{tip} < 1$) or fully charged with fluid ($\gamma_{tip} = 1$). Based on this variable, its derivatives and the flywheel geometry, the variable properties of the flywheel, such as fluid velocity, mass flow, and Coriolis forces, can be calculated.

It should be noted that in this section vectors quantities are denoted by an underline ($\bullet$) notation.

4.3.1. Additional forces induced by the flywheel

Three types of forces are induced by the relative motion of the fluid inside the flywheel components. The forces correspond to the exchange of the angular momentum between the

blade stationary structure and the fluid masses. Therefore, the implementation of these forces in HAWC2 and BeamDyn is crucial for a correct representation of the operating flywheel. The three forces are graphically presented in Figure 14 and are briefly explained below:

1. **Coriolis forces**

   The radial movement of the fluid in the flywheel as the blades rotate produces Coriolis forces. Equation 7 expresses the Coriolis force, $\underline{F_c}$, that is applied to the centre of gravity of a considered element in terms of cross product, $\times$, the rotational speed of the element, $\underline{\omega}$, with the fluid translational velocity, $\underline{v}_{fl}$, of a fluid mass, m, that is crossing this element.

$$\underline{F_c} = -2 \cdot m \cdot (\underline{\omega} \times \underline{v}_{fl}) \qquad\qquad 7$$

2. **Fluid inertial forces**

   Acceleration or deceleration of fluid in time causes fluid inertial forces. These forces balance the change of the stored momentum inside the fluid due to the change of the mass flow. Equation 8 expresses the fluid inertial forces in terms of the fluid mass, m, and the fluid acceleration, $\underline{a}_{fl}$.

$$\underline{F}_{fl,acc} = -m \cdot \underline{a}_{fl} \qquad\qquad 8$$

3. **Momentum flux forces**

   The change of flow direction or local flow speed of a fluid due to a sudden change in the cross-sectional area causes hydraulic reaction forces to balance the difference in the transported momentum between the inlet and the outlet of a control volume. These forces are called momentum flux forces, $\underline{F}_{fl,mom,i}$, and are shown in Equation 9 as a difference in the hydraulic reaction forces between two neighbouring elements.

$$\underline{F}_{fl,mom,i} = (\dot{m}_{out} \cdot \underline{v}_{fl})_{i-1} - (\dot{m}_{in} \cdot \underline{v}_{fl})_i \qquad\qquad 9$$

where $(\dot{m}_{out})_{i-1}$ is the fluid mass flow at the outlet of the previous element, $i-1$, and $(\dot{m}_{in} \cdot \underline{v}_{fl})_i$ is the fluid mass flow at the inlet of the considered element, i.
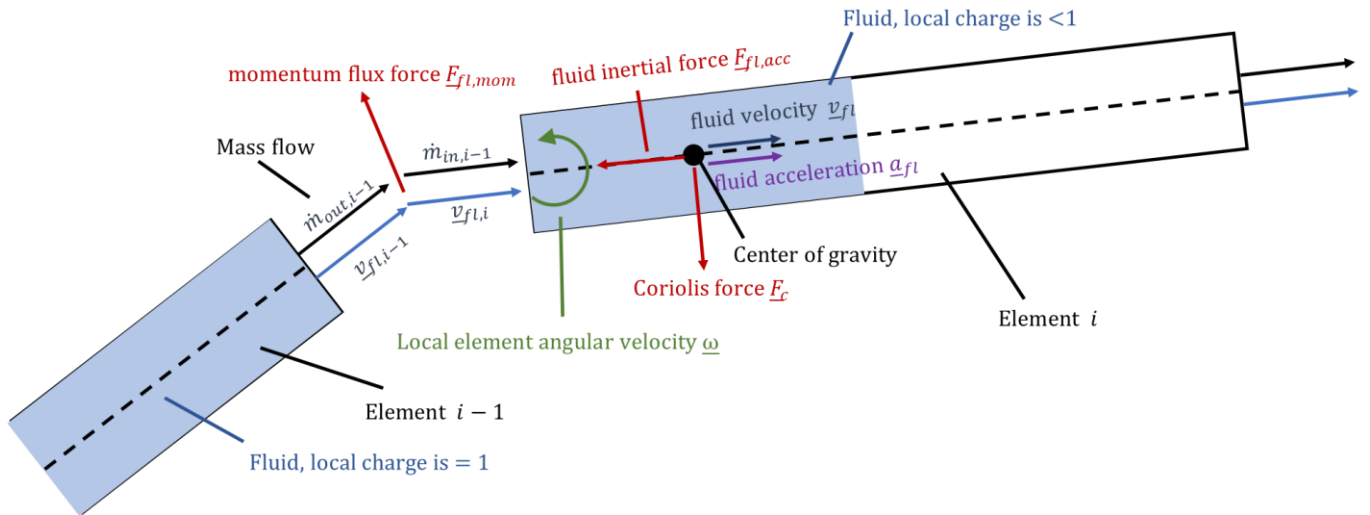
Figure 14: Coriolis force, fluid inertial force, and momentum flux force induced by the flywheel in a free body diagram of two adjacent flywheel elements.

If these three types of forces are treated correctly within the HAWC2 and BeamDyn models, the conservation law of momentum and angular momentum of a wind turbine with a flywheel in its rotor should still hold.

Other forces, which are related to the stationary effects of the additional fluid masses inside the blade are independent of the translational motion of the fluid. These forces, e.g., gravitational, centrifugal, gyroscopic forces, and inertial forces from fluid without relative motion in any arbitrary direction, are handled inside the original implementation methods in HAWC2 and BeamDyn.

4.3.2. Validation of the implementation methods of variable blade inertia in HAWC2 and BeamDyn

The validation of the implementation methods of variable blade inertia in HAWC2 and BeamDyn is based on three benchmarking cases. The complexity of the cases increases gradually, see Figure 15.

Figure 15: Schematic drawing of the three benchmarking cases.

Case 1 concerns the reaction forces and moments of a fixed supported beam that is subjected at its fixed end to a constant rotational speed around the x axis and axial fluid movement along the z axis. Case 2 uses the same beam that is used in Case 1 but the beam is pinned supported. The beam simulated in Case 3 is flexible, initially curved, and has similar mechanical properties of a wind turbine's rotor blade. Case 3 uses the same pinned support as in Case 2.
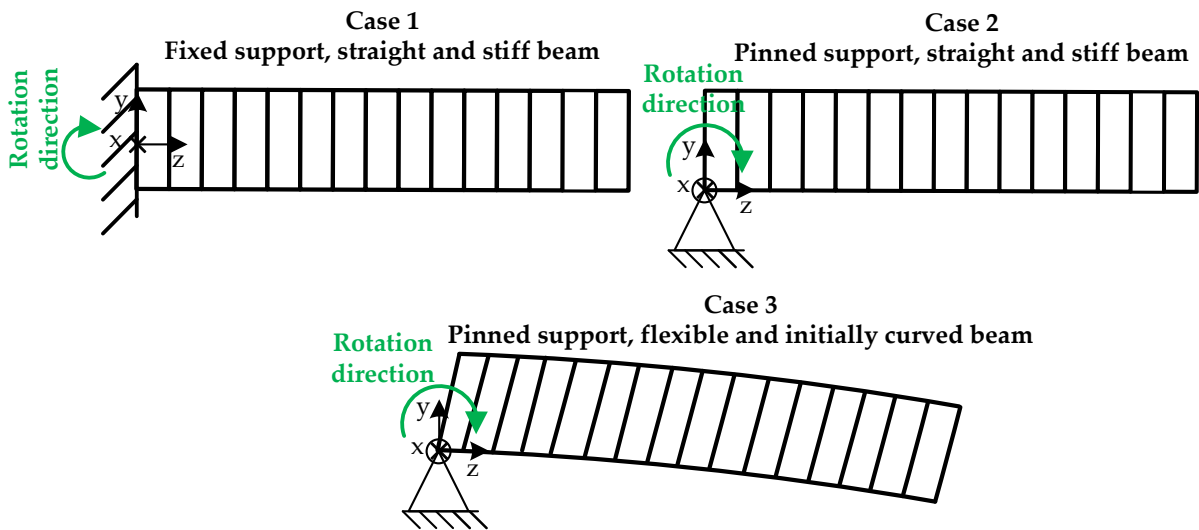
The main objective of these cases is to validate the method used in HAWC2 and BeamDyn to implement variable blade inertia. The validation is based on the proof of the physical laws of the equilibrium conditions and the conservation of angular momentum. In all three cases, the physical laws were analytically computed and compared with simulation results from the modified HAWC2 and BeamDyn models. Case 1 is presented in this section to illustrate the validation concept. Cases 2 and 3 have been discussed in detail in Publication 4.

4.3.3. Case 1

The beam used in Case 1 is straight and discretized in 15 elements of 1 m in length. Three hydraulic components are integrated into the beam: pipe, root and tip piston accumulators. Each component has 5 elements. The total fluid mass that is moved between the root and the tip piston accumulators equals 500 kg. A schematic drawing of the beam in charge states 0 and 1 is shown in Figure 16 (a) and (b), respectively.
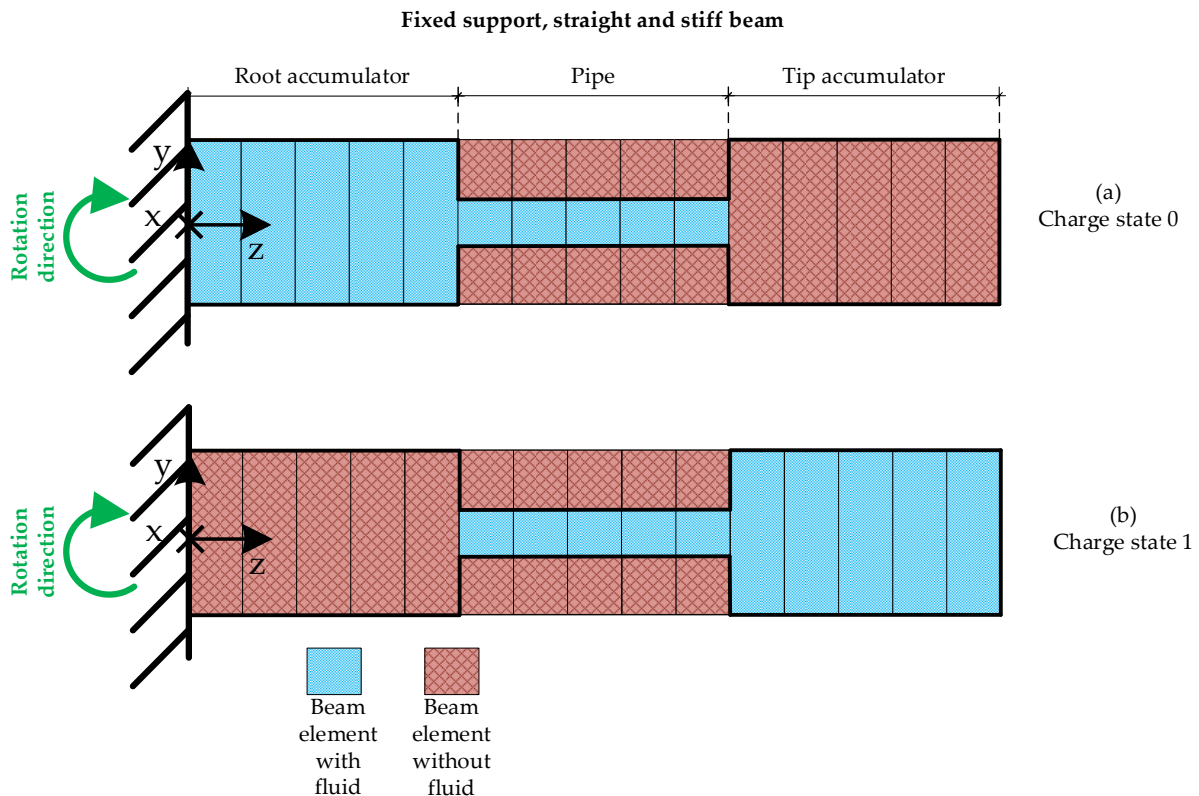
Figure 16: Schematic drawing of the pipe, root and tip piston accumulators in a fix supported, straight and stiff beam in, (a) a discharged state and (b) a fully charged state.

When the charge state equals 0, the root piston accumulator is full and the tip piston accumulator is empty. Conversely, the root piston accumulator is empty and the tip piston accumulator is full, when the charge state equals 1. The charge state therefore varies between 0 and 1 as the fluid moves between the root and the tip piston accumulators.

The input cross-sectional mass and stiffness parameters of the beam are presented in Table 2. In Case 1, the beam stiffnesses are set to very high values to prevent the beam from bending. This keeps the local coordinates of the beam elements synchronized with the root coordinates of the beam at the fixed end coordinates of the beam, and simplifies the analytical calculation of the reaction forces and moments.

Table 2: Cross-sectional mechanical properties of the straight and stiff beam.

Beam element mass density	Flap and edge mass moments of inertia per unit span	Flap stiffness	Edge stiffness	Flap shear stiffness	Edge shear stiffness	Torsional stiffness
kg/m	kg·m	N·m^2	N·m^2	N·m^2	N·m^2	N·m^2
50	50	1.00E+10	1.00E+10	5.00E+08	5.00E+08	1.00E+09

For Case 1, the simulation scenario presented in Figure 17 sets the rotational speed to a constant value of 10 rpm. The charge state rises from 0 to 1 between 10 s and 50 s and remains constant till 60 s. Between 60 s and 100 s the charge state is reduced from 1 to zero and remains at 0 until the end of the simulation. Reaction forces and moments result from the fluid movement. The x, y and z components of these forces and moments were analytically calculated and compared with the corresponding simulation results from HAWC2 and BeamDyn. The comparisons in Figure 17 show a very good agreement between the analytical and the simulated results of all components. The in-crease/decrease of the y component of the reaction force is due to the Coriolis forces that result from the change in the charge state. Hence, a reaction moment around the x axis results from these Coriolis forces. The z component of the reaction force illustrates the sum of the centrifugal forces and the fluid inertial forces. The variation in the centrifugal forces results from the change in the centre of gravity of the beam due to the fluid motion. The fluid inertial forces (Equation 8) can be seen when the fluid accelerates, e.g. from 10 to 11 s, or deaccelerates, e.g. from 50 to 51 s.

x-component of the root reaction force

y-component of the root reaction force

z-component of the root reaction force

x-component of the root reaction moment

y-component of the root reaction moment
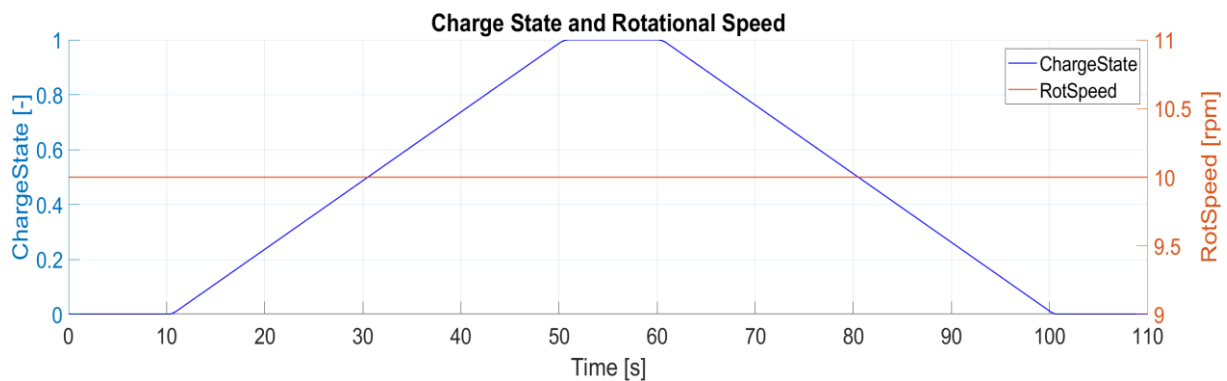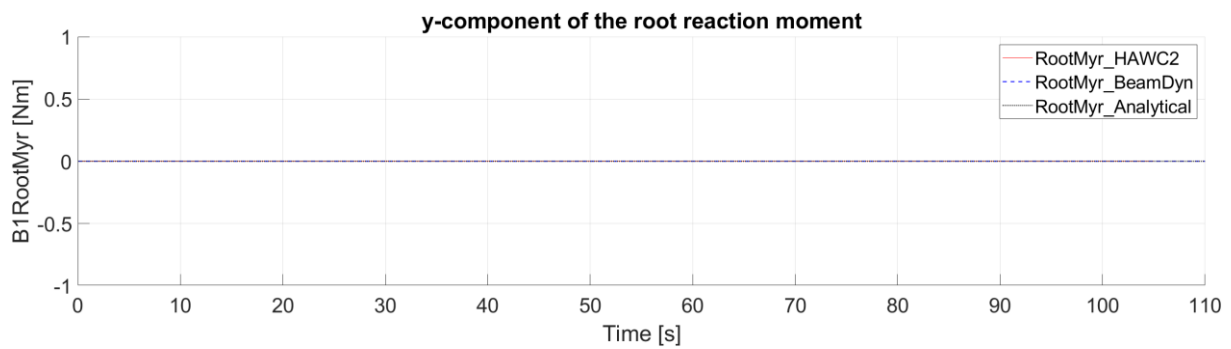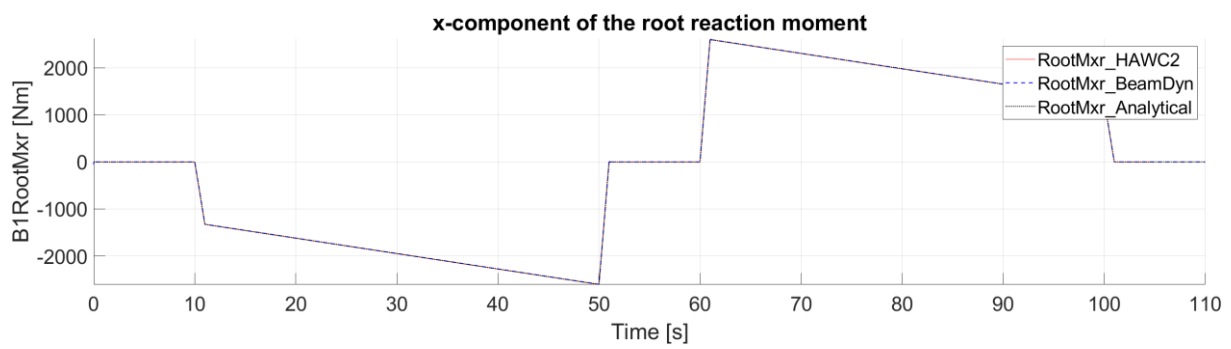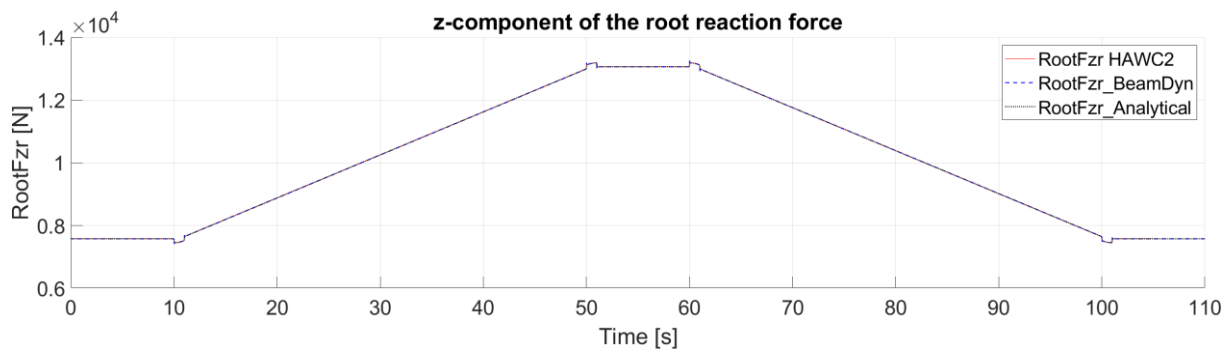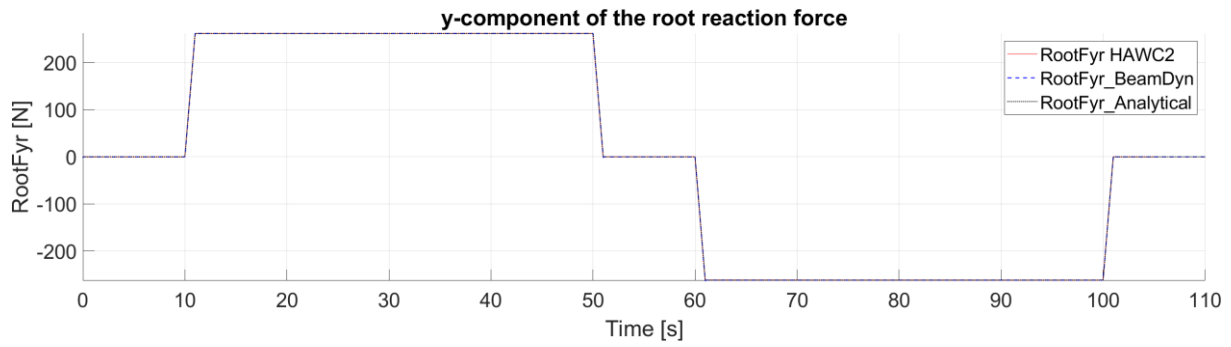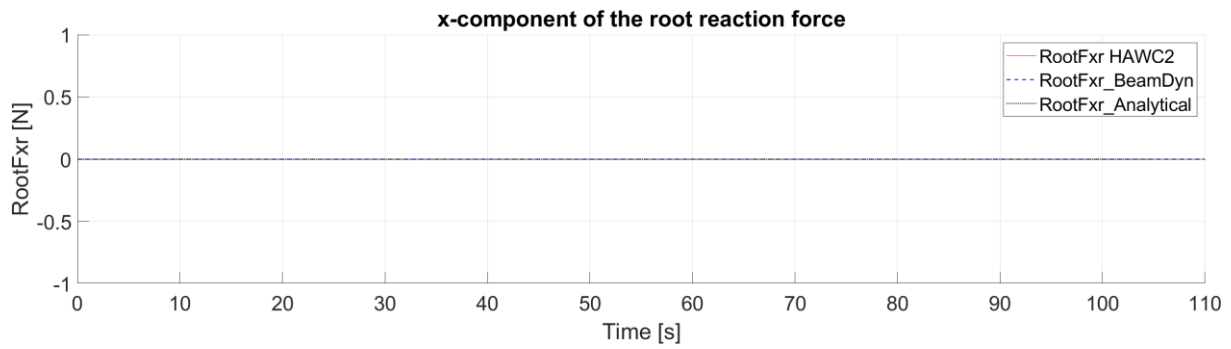
Figure 17: Change in the charge state with a fixed rotational speed. Comparison of the x, y and z components of the analytical reaction forces at the fixed support (dotted black) with the simulated root reaction forces and moments from HAWC2 (red) and BeamDyn (blue dashed).

4.3.4. Application of the flywheel when the wind turbine performs emergency braking
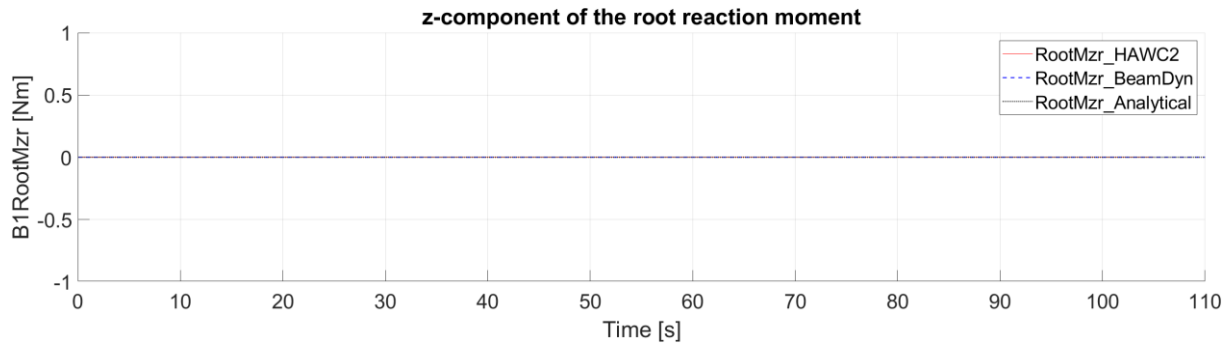
Numerous functionalities of the flywheel can be applied to deal with various grid events, and to reduce the mechanical loads on the structure of wind turbines [13]. These functionalities were developed via the First Eigenmodes simulation model [9]. However, as discussed in the beginning of this section, this model is not suitable for evaluating the impact of the flywheel on the mechanical loads of wind turbines. Since the validation presented in the previous section proved that the modified HAWC2 and BeamDyn models are able to simulate the dynamic behaviour of the flywheel, these modified models can be used to analyse the stress reduction functionalities of the flywheel on wind turbine components.

Emergency braking is one of the most drastic events that can occur to a wind turbine. It causes significant stress on the support structures of the wind turbine, especially on the tower bottom and the foundation. A worst-case scenario, in which the wind turbine has to be brought to standstill, is presented in the design load case (DLC) 2.3 in the IEC-61400-1 standard [20]. DLCs are simulation scenarios that are defined in wind turbine guidelines, and used to verify wind turbine designs. DLC 2.3 is defined as a combination of a significant wind event, i.e. extreme operation gust (EOG), with an internal or external electrical system fault, i.e. loss of electrical grid. According to the IEC-61400-1 standard, a study of several combinations of different wind speeds and times of grid loss events with respect to the EOG need to be simulated in order to determine which combination has the most critical effect on the simulated wind turbine. Hence, a study was performed for different combination scenarios on the NREL 5 MW reference wind turbine [10]. The study showed that the combination of a rated wind speed of 11.6 m/s with a time of grid loss at the lowest wind speed in the EOG (see the event start in Figure 18 (a)) had the greatest load effect on the wind turbine support structure. Based on this finding, DLC 2.3 was simulated initially in the original codes of HAWC2 and OpenFAST. Figure 18 (a) and (b) show that even when the wind speed, generator torque, and pitch control outputs from OpenFAST and HAWC2 are identical, the rotor speeds deviate slightly. This deviation is due to the differences in the implementation of the blade element momentum (BEM) theory in the aerodynamics models in HAWC2 [21] and OpenFAST [22]. Consequently, Figure 18 (c) illustrates the difference in the aerodynamic torque values generated by HAWC2 and OpenFAST.

Since the aerodynamics models of HAWC2 and OpenFAST are not in the scope of this dissertation, the difference in these aerodynamics models is not further investigated. However, in order to evaluate the effect of the flywheel on the 5 MW wind turbine without the effect of the difference in the aerodynamics models, two comparisons are presented in Figure 19: 5 MW wind turbine with and without flywheel in OpenFAST (Figure 19, right hand side), and 5 MW wind turbine with and without flywheel in HAWC2 (Figure 19, left hand side).
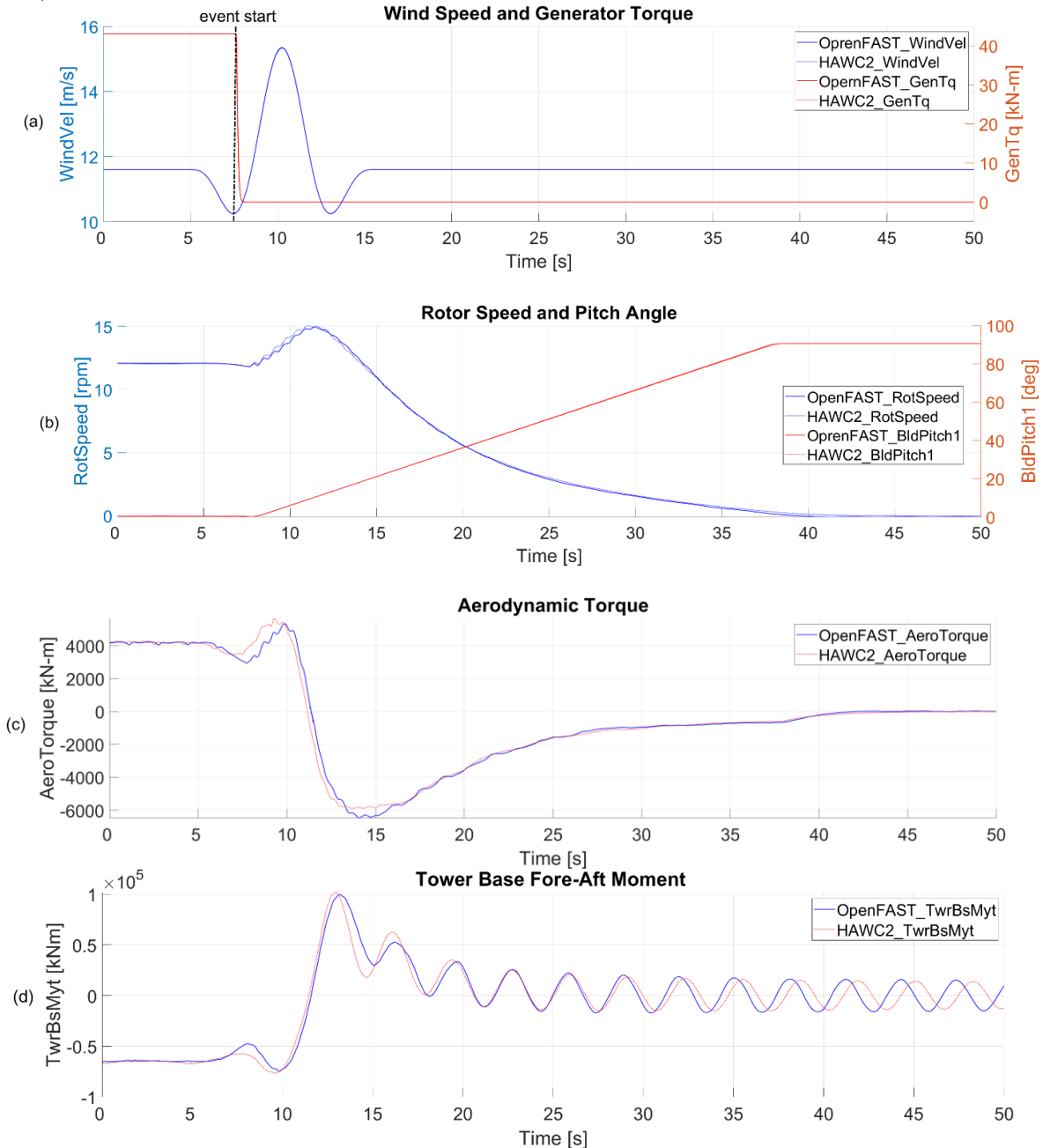
Figure 18: DLC 2.3 effect on a 5 MW refernce wind turbine simulated with OpenFAST and HAWC2. (a) EOG starting with rated wind speed of 11.6 m/s and grid loss at the lowest wind speed in the gust. (b) rotor speed and pitch angle. (c) aerodynamic torque. (d) the tower base fore-aft moment.

When there is a sudden grid loss, the generator torque disappears, see Figure 18 (a), and the wind turbine has to be quickly brought to standstill to avoid excessive overspeed. This is done by quickly pitching the blade to feather position from 0° to 90°, see Figure 18 (b), i.e. by applying aerodynamic emergency breaking. However, quick pitching at high rotor speeds

27

leads to an increase in the mechanical loads on the wind turbine support structures. This can be seen in Figure 18 (d) as an increase in the tower base fore-aft moment.Flywheels can support aerodynamic emergency breaking in the case of DLC 2.3 by being charged to their maximum charge state in all three blades, see Figure 19 (a) and (b). This produces two decelerating torques: a mechanical decelerating torque at the low-speed shaft resulting from Coriolis forces, see Equation 7, and an electrical decelerating torque at the high-speed shaft resulting from the electric pumps, see Figure 19 (c) and (d). The charging of the flywheel is supported by the electrical pumps, which draw their power from the wind turbine generator, even when the wind turbine is no longer connected to the grid. In this state of operation, the generator with its frequency converter and the motors of the pumps exist as an electric island. Figure 19 (c) and (d) illustrate the damping effect of the mechanical decelerating torque form the flywheel on the out-of-plane blade tip deflection. Figure 19 (a) and (b) show that the rotor speed accelerates less when the flywheel is applied. The flywheel can decrease the tower base fore-aft moment by up to 12.5 %, see Figure 19 (e) and (f).

Figure 19: Comparison of the effect of DLC 2.3 on the 5 MW wind turbine with flywheel (blue & red) and without flywheel (black) in OpenFAST and HAWC2. (a) and (b) rotational speed and charge state of the flywheel. (c) and (d) out-of-plane tip deflection and generator and flywheel pumps electrical torque. (e) and (f) tower base fore-aft bending moment.

5. Conclusions and future work

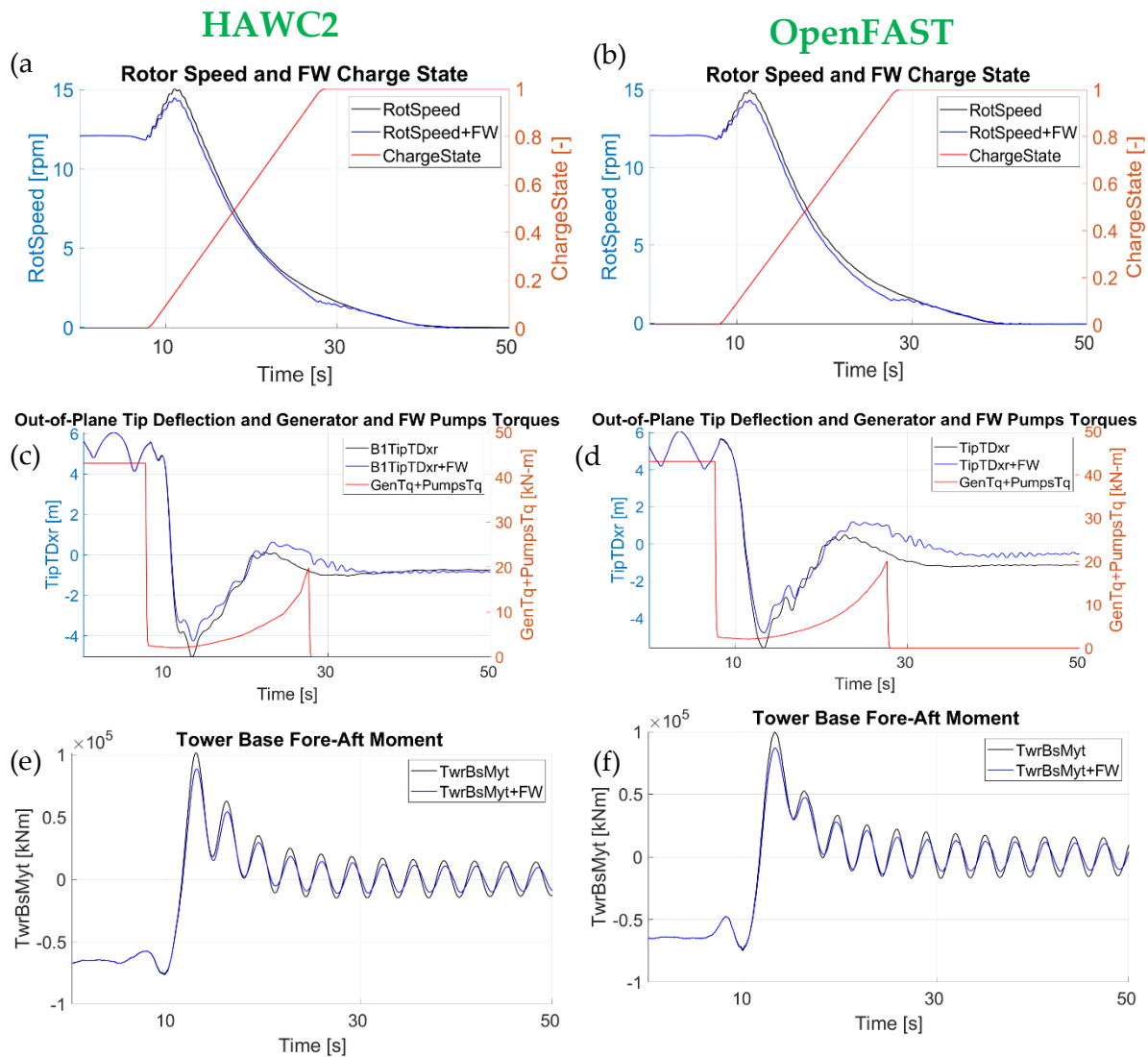This Ph.D. project investigated whether a flywheel could be installed into a wind turbine's rotor blades without making them significantly heavier. Furthermore, the dynamic behaviour of a flywheel was implemented in state-of-the-art load simulation tools in order to analyse the impact of a flywheel on the wind turbine components.

5.1. Conclusions

Previous studies of a hydraulic-pneumatic flywheel considered the piston accumulators to be separate components inside the rotor blades of wind turbines [6,7]. This is because the piston accumulators were made of steel, which made them heavy and unbendable. Such heavy steel components would increase the mass of the rotor blades significantly. Furthermore, it was not possible to analyse the impact of the dynamic behaviour of the flywheel on the wind turbine components as state-of-the-art load simulation tools could not be modified to implement variable blade inertia.

These problems have been solved within this Ph.D. project by:

1- Development of flexible piston accumulators made of CFRP (Publications 1 and 2): These are not only lighter than the steel piston accumulators, but are also able to bend whenever the rotor blade bends. A load comparison analysis showed that the increase in ultimate and fatigue loads of the blade, the tower, and the drive train using the CFRP flywheel design are much smaller than those for the conventional steel flywheel design. The bending capability of the CFRP flywheel allows piston accumulators to be integrated into the support structure of the rotor blade. An algorithm was created to enable the minimisation of the additional stationary masses in the rotor blades. This algorithm iteratively replaced parts of the blade spar caps with composite material of the piston accumulators. The result of this study showed that the flywheel can be installed in the rotor blades without making the wind turbine significantly heavier.

2- Implementation of variable blade inertia in state-of-the-art load simulation tools (Publications 3 and 4): Initially, the source code of the structural dynamic model of ElastoDyn was modified. This modification enabled ElastoDyn to simulate the dynamic behaviour of the flywheel in the load simulation tool of OpenFAST. As one of the several applications of the flywheel, the modified ElastoDyn was applied to correct rotor mass imbalance. The method used in ElastoDyn to implement variable blade inertia was further improved and implemented in the two advanced structural dynamic models HAWC2 and BeamDyn. The modified models were validated on the basis of three benchmarking cases of increasing complexity. For all three cases, the validation showed very good agreement between BeamDyn, HAWC2, and analytical calculations. Simulating the application of the flywheel in the rotor blades of the NREL 5 MW reference wind turbine when it is subject to DLC 2.3 showed that the flywheel reduced the tower base fore-aft bending moment by 12 %. This result was achieved with both HAWC2 and OpenFAST. With variable blade inertia, the simulated effect of the flywheel showed good agreement between HAWC2 and OpenFAST in the results of the rotor blade motions, e.g. the rotor speed and the out-of-plane motion, as well as in the tower base torque.

From 1 it can be concluded that the flexible piston accumulators made of CFRP that are presented in this thesis reduce the additional stationary mass of the flywheel significantly in comparison to conventional steel design of the flywheel. Moreover, the CFRP piston accumulators can be integrated into the support structure of the rotor blades. From 2, it can further be concluded that numerous applications of the flywheel can be simulated with modified source codes of OpenFAST/BeamDyn and HAWC2. Furthermore, the impact of the flywheel on the wind turbine components can be simulated by implementing the dynamic behaviour of the flywheel in the state-of-the-art load simulation tools.

5.2. Future Work

This Ph.D. project has shown that the effect of the flywheel on the wind turbine components, and in particular on the blade eigenfrequencies, increased when the tip piston accumulators are installed deeper within the blade tip. However, as the cross-sectional area of the blade decreases towards the blade tip, the tip accumulators must be lengthened. Therefore, further work in cooperation with HYDAC GmbH will focus on the manufacturing and testing of flexible piston accumulators made of CFRP which are longer than 10 m.

Increasing the effect of the flywheel is not only possible with installing the tip accumulators deeper in the blade tip, but also with using fluids that have high densities [23]. These fluids are able to store greater amounts of energy when they are moved between the root and the tip accumulators. Hence, further research should investigate the usability of such heavy fluids for applications in the flywheel in more detail.

As the piston accumulators are considered as part of the support structure, it must be further investigated how the piston accumulators can be connected to the material of the support structure of the blade.

The method used in this project to implement variable blade inertia in HAWC2 and BeamDyn should be refined to consider all moving parts in the hydraulic–pneumatic flywheel, i.e. also the pistons and the compressed gas. These two components have not been considered in the modified codes of HAWC2 and BeamDyn.

Based on the results of this Ph.D. project, a new project will start towards the end of 2023, which will focus on the application of the modified HAWC2 and OpenFAST/BeamDyn to simulate different wind turbine types with the new flywheel design.

References

1. Jauch, C. A Flywheel in a Wind Turbine Rotor for Inertia Control. *Wind Energy* **2015**, *18*, 1645–1656, doi:10.1002/we.1784.
2. Jauch, C.; Hippel, S. Hydraulic–Pneumatic Flywheel System in a Wind Turbine Rotor for Inertia Control. *IET Renewable Power Generation* **2016**, *10*, 33–41, doi:10.1049/iet-rpg.2015.0223.
3. Jauch, C. Grid Services and Stress Reduction with a Flywheel in the Rotor of a Wind Turbine. *Energies* **2021**, *14*, 2556, doi:10.3390/en14092556.
4. Jauch, C. Controls of a Flywheel in a Wind Turbine Rotor. *Wind Engineering* **2016**, *40*, 173–185, doi:10.1177/0309524X16641577.
5. Hochschule Flensburg, Pirouetten Für Die Energiewende, Ideenwettbewerb Schleswig-Holstein Available online: https://hs-flensburg.de/hochschule/aktuelles/2016/12/3/pirouetten-fuer-die-energiewende (accessed on 15 August 2023).
6. Hippel, S.; Jauch, C.; Ritschel, U. Hydraulic-Pneumatic Flywheel Configurations for Controlling the Inertia of a Wind Turbine Rotor. *Wind Engineering* **2019**, *43*, 114–132, doi:10.1177/0309524X18780386.
7. Hippel, S.; Jauch, C. Load Analysis of Hydraulic-Pneumatic Flywheel Configurations Integrated in a Wind Turbine Rotor. *Wind Energy* **2019**, *22*, 1190–1202, doi:10.1002/we.2349.
8. Jauch, C. First Eigenmode Simulation Model of a Wind Turbine – for Control Algorithm Design. **2016**, doi:10.13140/RG.2.2.15839.46244.
9. Jauch, C. First Eigenmodes Simulation Model of a Wind Turbine - for Control Algorithm Design. **2020**, doi:10.13140/RG.2.2.17192.19204.
10. Jonkman, J.; Butterfield, S.; Musial, W.; Scott, G. Definition of a 5-MW Reference Wind Turbine for Offshore System Development. *System Development* **2009**, 75.
11. Jonkman, J.M.; Buhl, M.L.Jr. *FAST User's Guide - Updated August 2005*; 2005; p. NREL/TP-500-38230, 15020796;
12. Resor, B. *Definition of a 5MW/61.5m Wind Turbine Blade Reference Model.*; 2013; pp. SAND2013-2569, 1095962;.
13. Jauch, C. Grid Services and Stress Reduction with a Flywheel in the Rotor of a Wind Turbine. *Energies* **2021**, *14*, 2556, doi:10.3390/en14092556.
14. ElastoDyn Users Guide and Theory Manual — OpenFAST v3.4.1 Documentation Available online: https://openfast.readthedocs.io/en/main/source/user/elastodyn/index.html#elastodyn-users-guide-and-theory-manual (accessed on 28 March 2023).
15. Kane, T.R.; Levinson, D.A. *Dynamics, Theory and Applications*; McGraw Hill, 1985; ISBN 978-0-07-037846-9.
16. Cacciola, S.; Agud, I.M.; Bottasso, C.L. Detection of Rotor Imbalance, Including Root Cause, Severity and Location. *J. Phys.: Conf. Ser.* **2016**, *753*, 072003, doi:10.1088/1742-6596/753/7/072003.
17. Larsen, T.J.; Hansen, A.M. How 2 HAWC2, the User's Manual Available online: https://tools.windenergy.dtu.dk/HAWC2/manual/How2HAWC2_12_9.pdf.
18. Wang, Q.; Sprague, M.A.; Jonkman, J.; Johnson, N.; Jonkman, B. BeamDyn: A High-Fidelity Wind Turbine Blade Solver in the FAST Modular Framework. *Wind Energy* **2017**, *20*, 1439–1462, doi:10.1002/we.2101.
19. Pavese, C.; Kim, T.; Energy, D.W. HAWC2 and BeamDyn: Comparison Between Beam Structural Models for Aero-Servo-Elastic Frameworks. 11.
20. IEC 61400-1:2019 RLV | IEC Webstore | Rural Electrification, Wind Power Available online: https://webstore.iec.ch/publication/64648 (accessed on 12 June 2023).
21. Madsen, H.A.; Larsen, T.J.; Pirrung, G.R.; Li, A.; Zahle, F. Implementation of the Blade Element Momentum Model on a Polar Grid and Its Aeroelastic Load Impact. *Wind Energy Science* **2020**, *5*, 1–27, doi:10.5194/wes-5-1-2020.
22. Jonkman, J.M.; Hayman, G.J.; Jonkman, B.J.; Damiani, R.R.; Murray, R.E. AeroDyn V15 User's Guide and Theory Manual. *Renewable Energy*.
23. K. Onyema High-Density Fluids for the Use in Flywheel Systems Inside Wind Turbine Rotor Blades. Master Thesis, Flensburg University of Applied Sciences: Flensburg, 2022.

fluids

Article

Development of a Flexible Lightweight Hydraulic-Pneumatic Flywheel System for Wind Turbine Rotors

Laurence Alhrshy, Clemens Jauch and Peter Kloft

Special Issue

Wind and Wave Renewable Energy Systems

Development of a Flexible Lightweight Hydraulic-Pneumatic Flywheel System for Wind Turbine Rotors

Laurence Alhrshy [1],*, Clemens Jauch [1] and Peter Kloft [2]

1   Wind Energy Technology Institute, Flensburg University of Applied Sciences, Kanzleistraße 91-93, 24943 Flensburg, Germany; clemens.jauch@hs-flensburg.de
2   HYDAC Technology GMBH, Justus-von-Liebig Strasse, Werk 2, D-66280 Sulzbach/Saar, Germany; peter.kloft@hydac.com
*   Correspondence: laurence.alhrshy@hs-flensburg.de; Tel.: +49-461-48161-407

Abstract: In this paper, the design of a flexible piston accumulator for application in a hydraulic-pneumatic flywheel system in a wind turbine rotor is presented. The flywheel system enables a wind turbine to vary the inertia of its rotor blades to control the power output and, most importantly, to influence the vibratory behaviour of wind turbine components. The method used for designing the flexible accumulator is based on the one hand on test results of a flexible piston accumulator prototype, and on the other hand, on simulation results of a model of a flexible piston accumulator. As a result, a design of flexible piston accumulators for application in the flywheel system is implemented and compared with the design of conventional steel accumulators. Due to the proposed design of the flywheel system, the impact on the mechanical loads of a wind turbine is analysed. The simulation results show that the new design of the piston accumulators causes a lower impact on the mechanical loads of the wind turbine than a previously published design of piston accumulators. It is further shown that the considered wind turbine can take on the flywheel system without the need for reinforcements in the rotor blades.

Keywords: flexible accumulator; flywheel; hydraulic-pneumatic; load simulation; mechanical loads; piston accumulator; wind turbine

1. Introduction

For many years, a hydraulic-pneumatic flywheel (FW) system in the rotor of a wind turbine (WT) has been developing at the Wind Energy Technology Institute (WETI) of Flensburg University of Applied Sciences. The general idea of the FW system is based on the variation of the inertia of the rotor blades in a WT. This is done by moving a fluid mass between two piston accumulators in the rotor blade (see Figure 1). Kinetic energy is stored or released by varying the inertia of the rotor blades, which allows a certain variation of the electrical power of the WT, independent of the prevailing wind conditions. Additionally, and most importantly, the vibratory behaviour of the WT can be influenced. The physical description of such an energy storage system is introduced in previous work of the authors, and this covers the kinetics [1] and the hydraulics [2].

As most of the conventional hydraulic piston accumulators are made of steel, the initial design of the piston accumulator for the FW system was made of steel, too. This increases the additional stationary masses of the FW system enormously, and thus the total mass of the rotor blade. Moreover, conventional steel accumulators are not designed to bend with the rotor blade bending. Hence, in the initial design of the FW system, the dimensions of the accumulators, and the location where the accumulators are located in the rotor blades, are chosen such that the accumulators are never bent,

even when the rotor blades are bent most [3]. Because of these two disadvantages, conventional steel accumulators are less suitable for installation in the rotor blades of a WT. Consequently, the intention of the research published in this paper is to design a new piston accumulator for the FW system, that is lighter than steel accumulators on the one hand, and which, on the other hand, allows the piston accumulator to be bent whenever the rotor blade is bent. The challenge of bending a piston accumulator is to prevent the piston from getting stuck and to prevent gas leakages across the piston rings. Carbon fibre-reinforced plastic (CFRP) is a material which is lighter and at the same time more bending-flexible than steel. Also, rotor blades of WTs are made of composite material. This offers better options for attaching the CFRP accumulators to the structure of a rotor blade, compared to steel accumulators. One of the biggest unsolved problems related to conventional steel accumulators is that their attachment to the rotor blade structure should allow the rotor blade to bend around the accumulator without inflicting a bending moment on the accumulator. Since this problem could so far not be solved in an economically feasible manner, steel accumulators were abandoned. Consequently, the focus shifted to the design of flexible CFRP accumulators that are allowed to be bent and that can be attached to the rotor blade structure along their entire length.
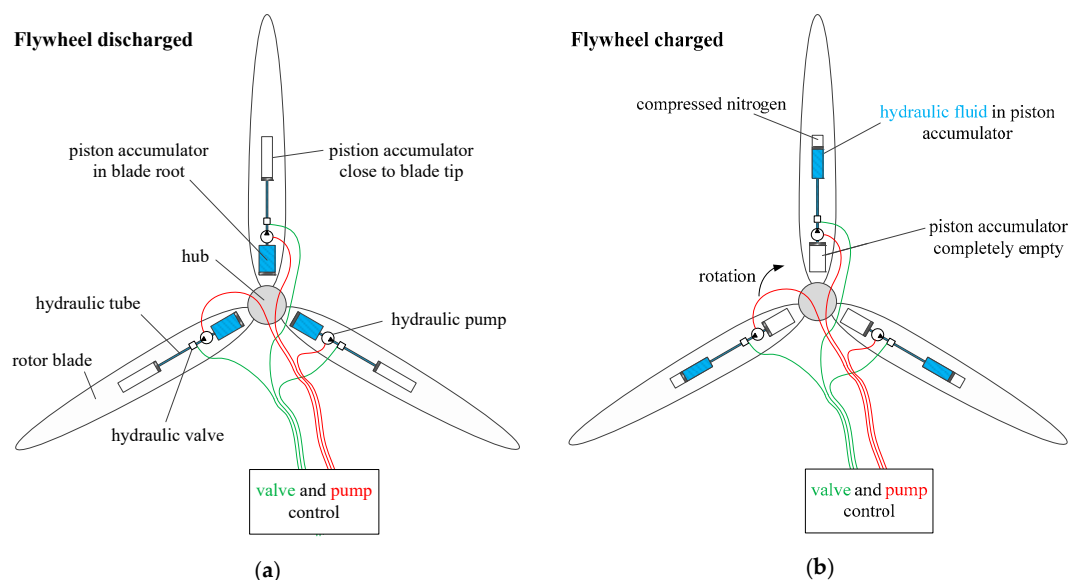
Figure 1. Simplified sketch of the flywheel (FW) system: (**a**) flywheel in discharged state and (**b**) flywheel in charged state.

Information about lengths and diameters of the accumulators are obtained from a previous work of the author [3], where a methodology was used to determine the dimensions and positions of the steel accumulators. As a result, several FW configurations were derived. Using the same methodology to derive the FW configurations of CFRP accumulators brings about the advantage that the calculated loads and masses of the CFRP accumulator can be compared with the loads and masses that resulted from the previously investigated steel accumulators.

However, since the goal of this paper is not to compare all the FW configurations published in Hippel et al. [3] for the conventional and for the flexible CFRP design of piston accumulators, the comparison is limited to three relevant FW configurations. The three selected FW configurations are those which represent the largest, a medium and the lowest impact on the mechanical loads. In the following, the considered FW configurations are called "types" and are identified with Roman numerals, as introduced in Hippel et al. [3]. FW type I causes the lowest impact on the mechanical loads of the rotor blades, although this type is the heaviest, and the FW type IV causes the largest impact on the mechanical loads of the rotor blades, although this type is the lightest. FW type VI causes a medium impact on the mechanical loads of the rotor blade compared to the FW types I and IV.

In addition, type VI has an average weight between FW type I and FW type IV. Additionally, these three FW types cover the most relevant locations for installation of piston accumulators inside the rotor blades.

Due to the frequent use of the 5 megawatt (MW) WT of the National Renewable Energy Laboratory (NREL) (Denver, CO, USA) and the public availability of its data [4], the FW system was adapted to this WT. The impact of the FW system on the mechanical loads of the 5 MW WT is analysed by performing load simulations using FAST v7 (Denver, CO, USA). FAST is a computer-aided-engineering tool, which is developed by NREL for simulating the coupled dynamic response of WTs [5]. This load simulation tool, as well as all other state-of-the-art load simulation tools for WTs, is incapable of representing variable rotor blade inertias as they occur in the FW system. Hence, in this work, the load simulation can only be done for two conditions: FW statically charged and FW statically discharged (see Figure 1).

In order to have reference values for the load comparison, load simulation results for the original NREL 5 MW WT rotor blade (without FW system) and for the NREL 5 MW WT rotor blade with steel accumulators are taken from Hippel et al. [6]. These reference values are compared with load simulation results of the NREL 5 MW WT rotor blade with CFRP accumulators. This comparison illustrates the impact of different FW designs on different components of the WT. Based on the results of the load analysis, ultimate and fatigue damages on the rotor blade of the WT can be evaluated, and countermeasures such as reinforcement of the blade can be derived. With this methodology, the solution for the aforementioned problem that steel accumulators had to be abandoned, can be validated.

2. Bending Inflicted on Piston Accumulators Due to Rotor Blade Bending

As mentioned above, piston accumulators for FW systems in WT rotor blades should be flexible, i.e., piston accumulators should be connected to the rotor blade along their entire length, which means that they will be bent whenever the rotor blade is bent. For the piston accumulators, this implies that the piston rings have to seal the gap between the piston and the cylinder, even if the cylinder is bent. Also, the piston must not clamp, i.e., it must be free to move under any realistically conceivable bending.

In order to design such a flexible piston accumulator for FW systems in rotor blades of WTs, it is important to know how the considered rotor blade deforms during operation. Hence, simulations of WT operation need to be performed to illustrate the displacement between blade nodes, where a piston accumulator could be installed. Based on the information that is obtained from such simulations, a flexible piston accumulator prototype was built, and tests are performed on this prototype, inter alia, to ensure gas-tightness during bending.

The structural design of the blade applied in the study that is presented in this paper is identical to the Sandia 61.5 m rotor blade [7]. This rotor blade is also applied in the original design of the 5 MW WT developed by NREL [4]. This conception takes advantage of the extensively used 5 MW reference WT in studies by the wind energy research community, as a system that represents the current and future state-of-the-art in offshore systems.

A rotor blade can be bent in edgewise direction and in flapwise direction. In flapwise direction, it is much more flexible than in edgewise direction; hence, it can bend a lot more in flapwise direction. Since a rotor blade can be considered a beam, it can vibrate with different eigenfrequencies, i.e., it has different eigenmodes. Vibration with a particular eigenfrequency leads to deformations of the blade with the respective mode shape. Due to the fact that the first and the second eigenmodes lead to the largest deflections of rotor blades, this study focusses on the first and the second eigenmodes in flapwise direction only. In order to compute the eigenmodes of a beam, like the Sandia 61.5 m rotor blade [7], a finite-element method (FEM) program is needed that provides the coupled modes of the WT blade. Such a program is also provided by NREL and is called BModes [8]. BModes applies the Euler Bernoulli beam theory combined with Hamilton's principle and is capable of computing the coupled modes of beams in general; hence, it can be used for both the blades and the tower of a WT. All the specifications that BModes needs, like rotor speed, blade geometry, and pitch control, can be

derived from the specification of the NREL 5 MW WT [4]. BModes also requires structural property distributions along the rotor blade. These properties are derived from the Sandia 61.5 m rotor blade design [7]. With the aforementioned information, an input file for BModes is prepared, in order to compute mode shapes and frequencies. BModes uses FEM followed by an eigen analysis to compute the eigenmodes [8]. As a result, BModes generates an output file, where the computed coupled mode shapes are shown as spanwise distribution of flap, edgewise, twist, and axial displacement components in a particular mode. Flap displacement is the displacement that the blade exhibits out of the rotor plane, relative to its rest position, when a pitch angle of zero degrees is considered [8]. This component is used to illustrate the nodal displacement for the first and the second eigenmodes in Figures 2 and 3, respectively. Based on this component, slope and curvature of modal displacement curve can be derived as follows, and shown in Figures 2 and 3.

$$slope = \frac{\text{d } flap\_disp}{\text{d } blade\_span} \tag{1}$$

$$curvature = \frac{\text{d}^2 flap\_disp}{\text{d } blade\_span^2} \tag{2}$$

where *blade span* is the span location of a point on the blade reference axis measured with respect to blade root, *flap disp* is the blade displacement out of the rotor plane obtained from BModes, *slope* is the first derivative of the flap displacement with respect to the *blade span*, and *curvature* is the second derivative of the flap displacement with respect to the *blade span*.

(**a**)

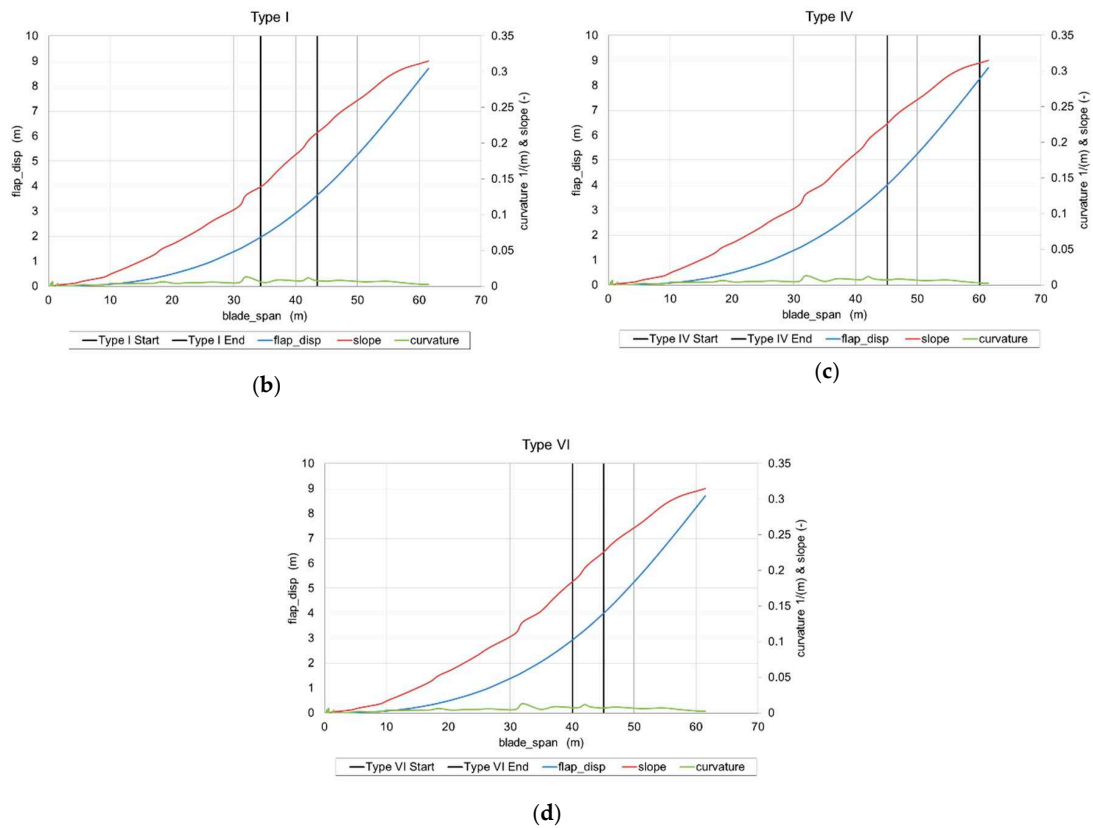**Figure 2.** *Cont.*

(**b**)

(**c**)

(**d**)
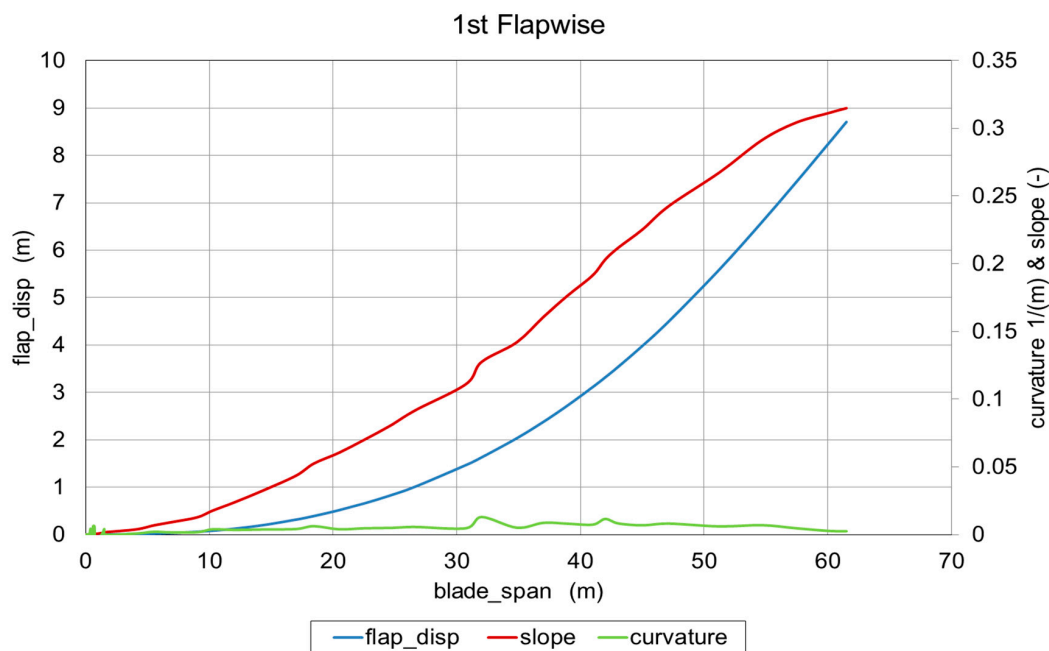
Figure 2. (**a**) Flap deflection, slope, and curvature of the first eigenmode of the considered wind turbine (WT) blade, (**b**) location of tip accumulator of type I, (**c**) location of tip accumulators of type IV, and (**d**) location of tip accumulators of type VI.

(**a**)

Figure 3. *Cont.*

(**b**)

(**c**)

(**d**)
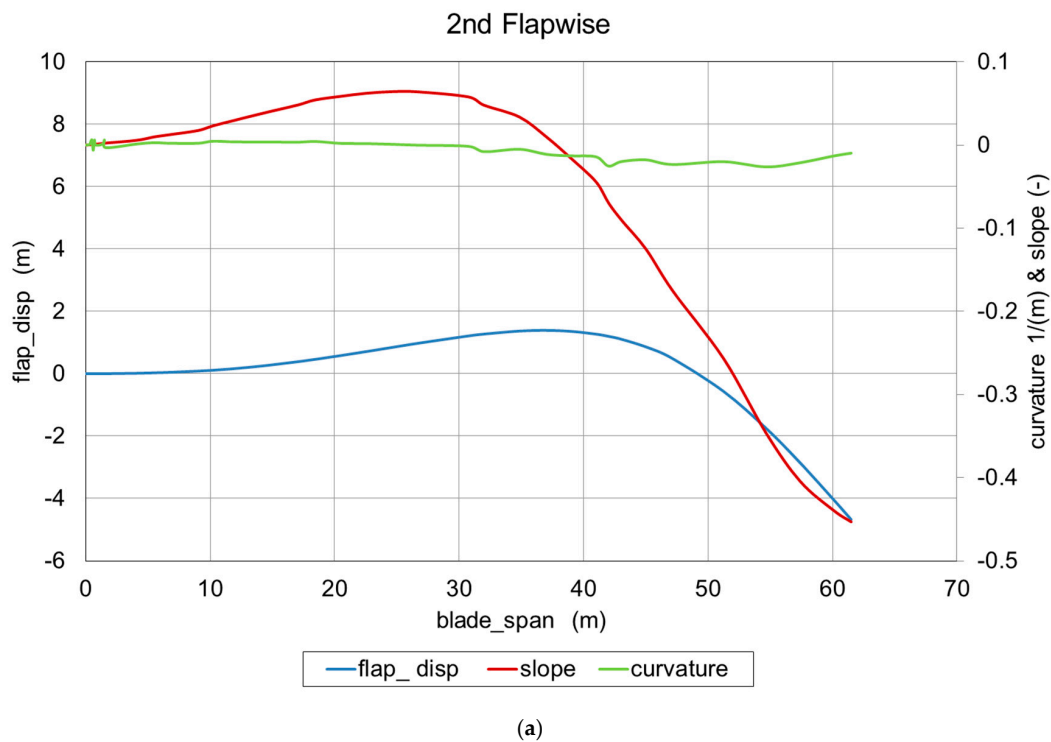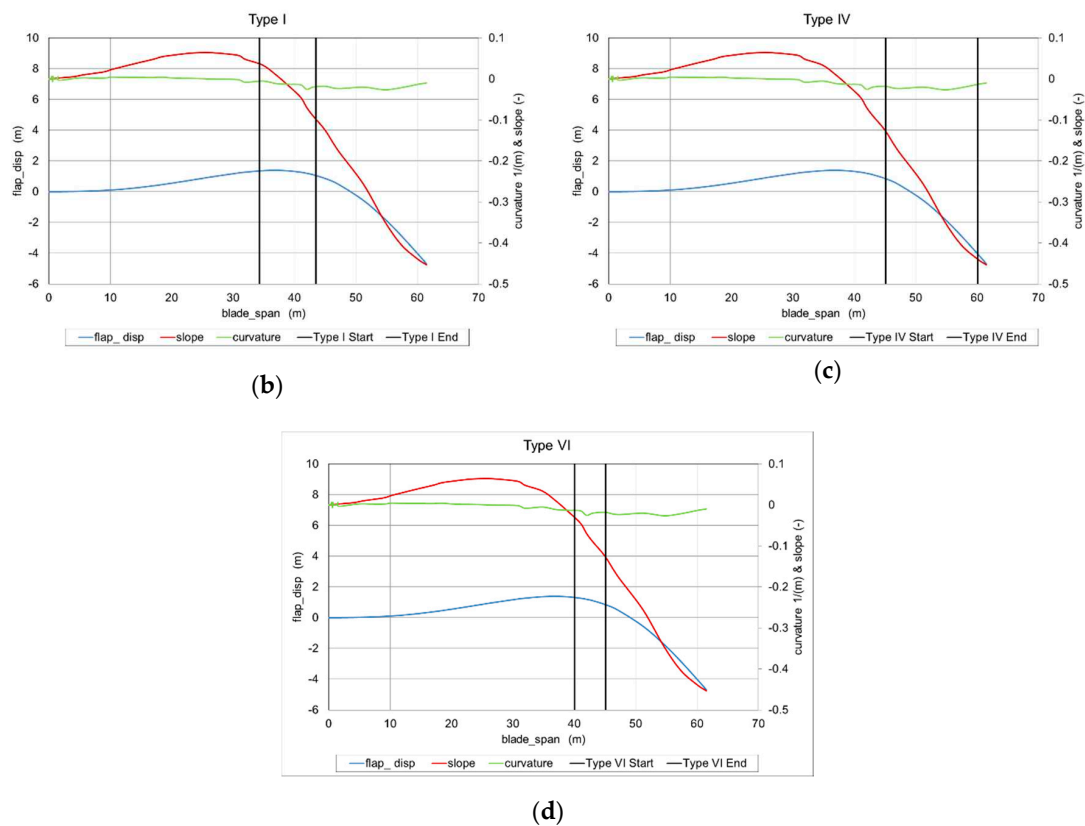
Figure 3. (**a**) Flap deflection, slope, and curvature of the second eigenmode of the considered WT blade, (**b**) location of tip accumulator of type I, (**c**) location of tip accumulators of type IV, and (**d**) location of tip accumulators of type VI.

Regarding the three FW types mentioned in the introduction, Figures 2 and 3 show the start and the end location of the tip accumulators, i.e., the tip accumulators are located between the span locations indicated by the vertical black lines in the diagrams (b), (c), and (d) of Figures 2 and 3. For better comprehensibility, the locations of the accumulators are visualized in the different blade sections in Figure 4. Information about flap displacement, slope, and curvature for the installation space of tip accumulators can be derived from Figures 2 and 3. This information can be used for defining the bending test for the flexible accumulator prototype. As a result, the design specifications of the prototype are applied to the FW types. In other words, the design of the CFRP piston accumulators of different lengths, diameters, and pressures, as needed for the three different FW types, are extrapolations of the design specifications of the prototype. This is outlined further in the next section.

Figure 4 presents the available spaces at each rotor blade section (in blue). Where a shows the root accumulator, the fluid pipe, and the tip accumulator (in red) of FW type I inside the rotor blade, Figure 4b, c show those components for FW type IV and FW type VI, respectively.

(a)

(b)

(c)
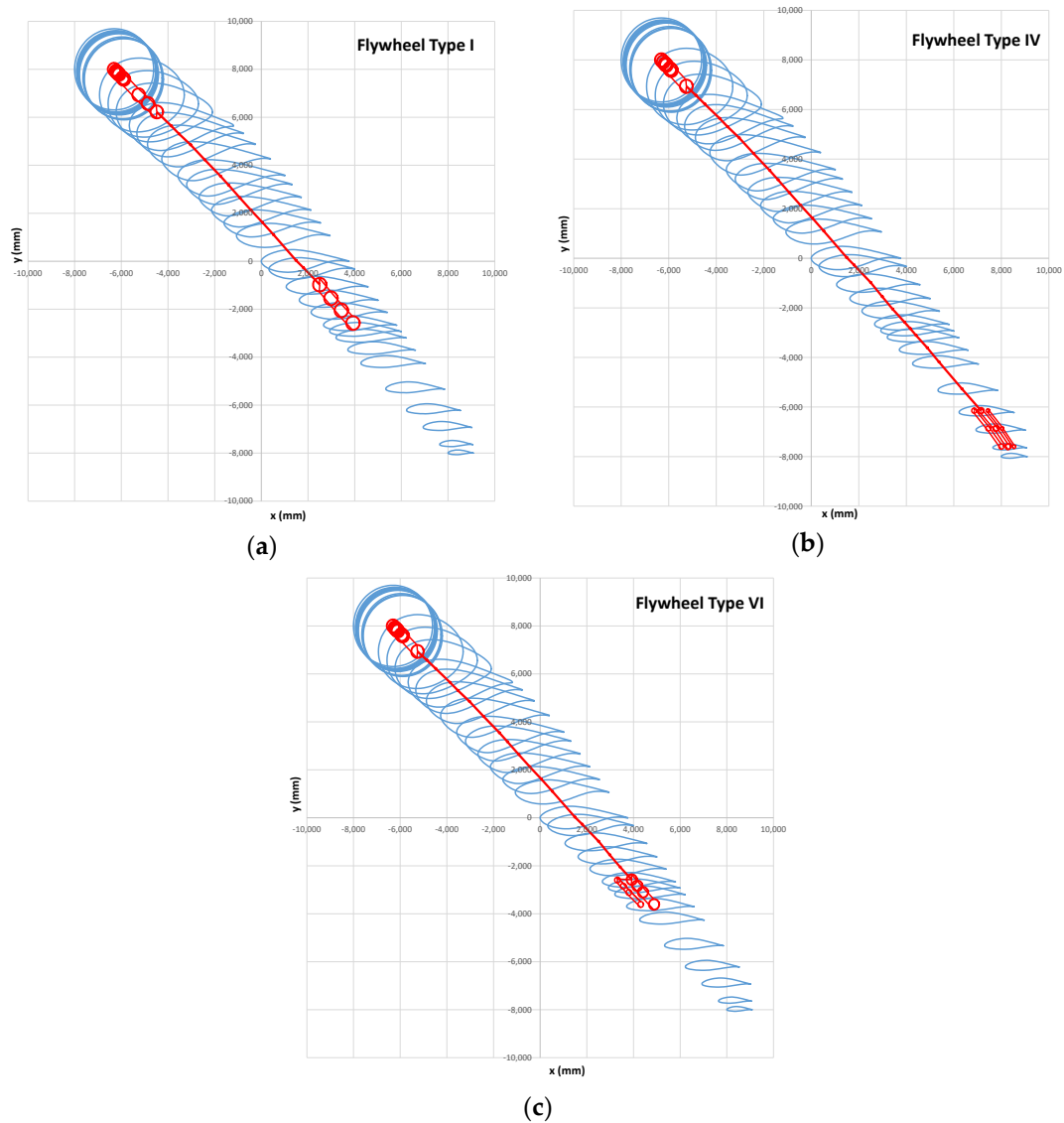
Figure 4. Cross-sections of the Sandia 61.5 m blade at the 38 blade nodes and the piston accumulators with fluid pipe of (**a**) FW type I, (**b**) FW type IV, and (**c**) FW type VI.

3. Specification of Flexible Carbon Fibre-Reinforced Plastics Piston Accumulator

The work documented in Section 2 leads to the conclusion that the piston accumulators should be used flexibly. They should be connected to the rotor blade along their entire length, which means that they will be bent whenever the rotor blade is bent.

3.1. Bending of Conventional Piston Accumulators

It is state-of-the-art that hydraulic-pneumatic piston accumulators must not be bent. Otherwise, it is to be expected that the piston gets stuck and that there are gas leakages from the gas chamber into the fluid chamber or fluid leakages from the fluid chamber into the gas chamber.

Figure 5 shows a bent piston accumulator with conventional piston in the side view. It can be seen that the gap between the piston and the cylinder is the only tolerance that is available for accommodating bending of the cylinder. The drawing in Figure 5 is not to scale; instead, the available gap is strongly exaggerated for illustration. Typically, the gap between piston and cylinder amounts to about 0.15 mm.

Figure 5. Illustration of a bent piston accumulator in the side view (not to scale).

The length of a conventional piston is typically about 60% of the diameter of the piston, as it has to be chosen such that the piston does not tilt under any circumstance. Figure 5 illustrates that the cylinder can only be bent until the gap is fully used up along the length of the piston. If the cylinder is bent further, the piston gets stuck.

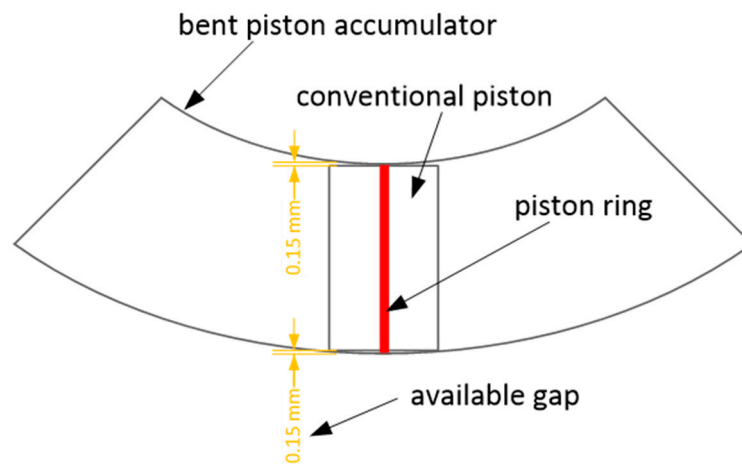Figure 5 shows that the piston ring is fully flattened on the inner radius of the bent cylinder. If the piston ring is not specifically designed for such deformation, it gets damaged. Subsequently, the piston ring would no longer be able to reliably separate gas from fluid, even if the cylinder were no longer bent.

Another problem that leads to leakages from bending the cylinder is the cross-sectional shape of the cylinder, which has to be circular, because the cross-sectional shape of the piston is also circular. However, if a cylinder, which is made of an isotropic material, is bent in the longitudinal direction, its cross-sectional shape becomes an ellipse, see Figure 6.
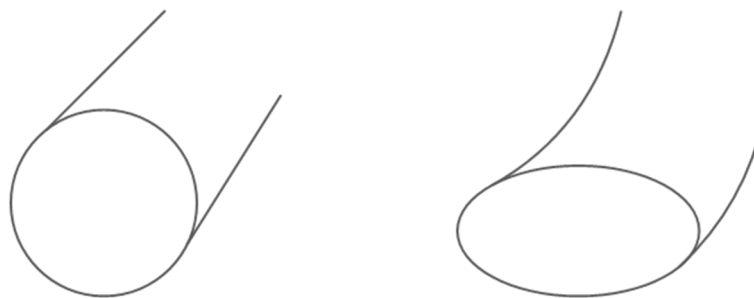
Figure 6. Cylinder made of an isotropic material. Left: in resting position with circular cross-section. Right: bent in the longitudinal direction, which turns the cross-section into an ellipse.

In a piston accumulator, the piston is usually a lot more rigid than the cylinder. Therefore, it can neither bend, nor can it match its cross-sectional shape to the cross-sectional shape of the cylinder. Consequently, there will be leakages between the circular piston and the elliptic cylinder.

3.2. Preliminary Design of Flexible Piston Accumulators

The problems mentioned above are solved by HYDAC Technology GmbH (HYDAC.com, Sulzbach, Saarland, Germany), who design flexible piston accumulators made of CFRP. This means that the piston rings have to seal the gap between the piston and the cylinder, even if the cylinder is bent. Also, the piston must be free to move under any bending. The material CFRP is advantageous because it is anisotropic, and hence, allows designing different properties in different directions. Furthermore, use of CFRP should lead to a weight reduction compared to conventional steel piston accumulators.

This motivated HYDAC, in cooperation with PRONEXOS (pronexos.com, Almelo, The Netherlands), to perform a test to specify a flexible CFRP piston accumulator with a metal liner on the inside of the CFRP cylinder.

In the process of manufacturing the cylinder, the anisotropic properties can be achieved by winding the carbon fibres in certain directions around the cylinder. Figure 7 qualitatively shows the different winding directions.

Figure 7. Qualitative illustration of the different winding directions that can be applied in the manufacturing process of a carbon fibre-reinforced plastic (CFRP) cylinder (the angles are only examples for illustrating the concept).

These winding directions lead to the following properties of the laminate:

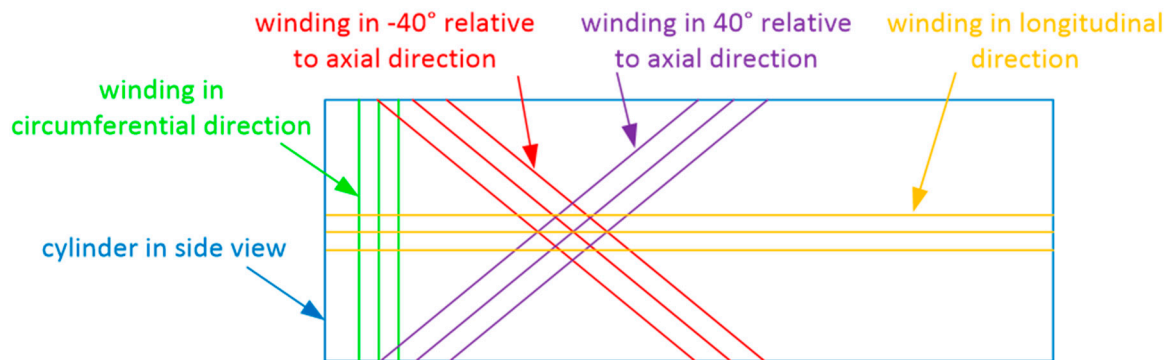- Windings in the circumferential direction increase the stiffness in the radial direction. The more carbon fibre layers are added in this direction, the less of a diameter increase the cylinder exhibits in case of internal pressure. Also, the cross-sectional shape is less prone to become an ellipse in case of longitudinal bending.
- Windings in the longitudinal direction increase the stiffness in the axial direction. By adding a specific number of windings in the longitudinal direction, the cylinder deflects by a certain extent from a specific external force in the lateral direction. The number of windings in the longitudinal direction has to be chosen such that these fibres rupture when the bursting pressure inside the cylinder is exceeded.
- Windings in a certain angle (positive and negative), with respect to the longitudinal axis, add to stiffness in the radial direction and in the axial direction, to an extent that depends on the angle. Most importantly, these windings add to the torsional stiffness of the cylinder (the angles shown in Figure 7 are only arbitrary examples for illustration).

When a piston accumulator is to be bent, the jamming of the piston, as shown in Figure 5, has to be prevented. At the same time, the piston has to reliably separate gas from fluid, i.e., the piston rings must not get damaged from bending the cylinder. These properties are achieved by making the piston from three flexibly connected discs, see Figure 8.

The outer discs (called stabilising discs in Figure 8) prevent the piston from tilting. The centre disc carries the piston ring, and therefore, separates the gas chamber from the fluid chamber. The three discs are connected to each other via a flexible rod, which can be bent easily when the cylinder around the piston gets bent.
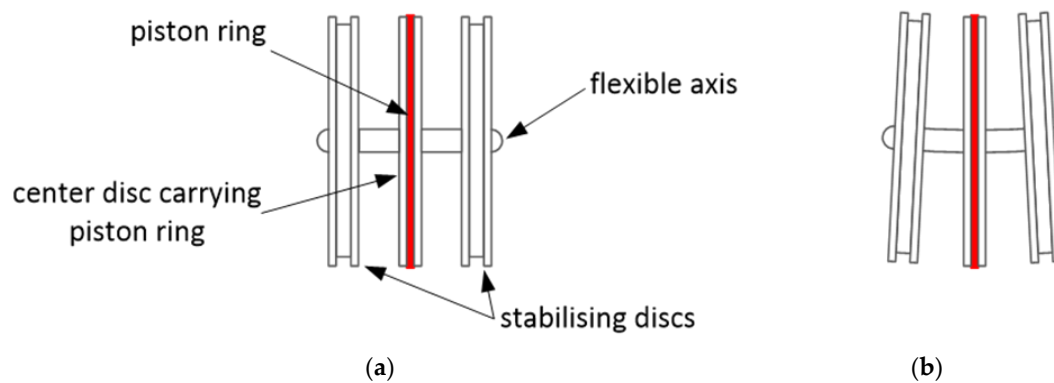
Figure 8. Flexible piston (**a**) with naming of components and (**b**) in bent state.

3.3. Test Specifications

Based on the information about the bending behaviour of the Sandia 61.5 m rotor blade presented in Section 2, HYDAC, in cooperation with PRONEXOS, built a prototype of a CFRP piston accumulator with a steel liner on the inner surface of the CFRP tube, see Figure 9. Figure 9 shows the steel liner covered with the CFRP laminate. In the background, the piston can also be seen. This prototype is tested in the test area of HYDAC Technology. Further design specifications for the prototype are:

- The structural strength of the laminate with the steel liner shall withstand the working pressure of 60 bar.
- A maximum diameter increase of the accumulator tube of 0.1 mm at 40 bar working pressure.
- The laminate should rupture in the longitudinal direction at burst pressure (>120 bar).
- The CFRP design shall be no more than 1.5 times as expensive as a comparable steel design.
- The steel liner at the inner surface shall have a wall thickness of 1 mm and its main purpose is to guarantee gas leak tightness, even in case of inter-fibre cracks in the CFRP laminate.

Figure 9. A prototype of a CFRP piston accumulator with a steel liner on the inner surface of the CFRP tube.

The materials used for the construction of the prototype are already qualified for series manufacturing at PRONEXOS. The steel liner of the prototype is produced via a cold-forming technology. Table 1 illustrates the material properties and the lay-up plan of the CFRP prototype.

Table 1. Laminate lay-up and the material properties of the CFRP with steel liner prototype.

Lay-Up No.	Thickness mm	Direction °	Density g/cm^3	$E_{\parallel}$ MPa	$E_{\perp}$ MPa	$G_{\perp\parallel}$ MPa	$v_{\perp\parallel}$ -
1	0.83	88	1.57	146,342	10,725	5376	0.2555
2	1.06	15	1.57	146,342	10,725	5376	0.2555
3	0.83	88	1.57	146,342	10,725	5376	0.2555
4	0.83	88	1.57	146,342	10,725	5376	0.2555
5	1.06	15	1.57	146,342	10,725	5376	0.2555
6	0.83	88	1.57	146,342	10,725	5376	0.2555
7	0.83	88	1.57	146,342	10,725	5376	0.2555
8	1.06	15	1.57	146,342	10,725	5376	0.2555
9	0.83	88	1.57	146,342	10,725	5376	0.2555
10	1	-	7.80	210,000	210,000	79,300	0.3200
Total thickness	9.16	-					

Where $E_{\parallel}$, $E_{\perp}$, $G_{\perp\parallel}$, and $v_{\perp\parallel}$ are the Young's modules parallel to fibre direction, the Young's modules perpendicular to fibre direction, the in-plane share modules, and the major Poisson's ratio of a CFRP laminate layer, respectively.

In order to verify the validity of the prototype specification, the prototype is modelled with the design tool COMPOSITOR v4.1 [9]. COMPOSITOR is a structural computer-aided-engineering tool, which was developed by the Institute for Plastics Processing at RWTH Aachen University (ikv-aachen.de, Aachen, Nordrhein-Westfalen, Germany).

For the working pressure of 40 bar, a load case of two global stresses can be translated on the basis of Barlow's formula [10]:

$$\sigma_t = \frac{p \cdot d_m}{2 \cdot s} \tag{3}$$

$$\sigma_a = \frac{p \cdot d_m}{4 \cdot s} \tag{4}$$

where σ_t and σ_a are the circumference and the longitudinal stresses, respectively. p is the internal pressure, d_m is the mean diameter, and s is the wall thickness of the pressure vessel, here, the tube of the piston accumulator. The material specifications and the laminate lay-up of the flexible accumulator prototype are considered in the simulation model of COMPOSITOR. As a result, two components of the strain, in circumference and longitudinal directions, are computed, based on the classical laminate theory. The resulting circumference strain can be transformed into a diameter increase, i.e., the diameter increase of the test model is about 0.08 mm at the working pressure of 40 bar, which is lower than the required maximum diameter increase of 0.1 mm.

The dimensions of the flexible piston accumulator prototype are listed in Table 2. These dimensions are limited by the dimensions of the test facility at HYDAC's test area. Hence, the prototype size is obviously not comparable with the dimensions of a piston accumulator for a FW system in a multi MW WT rotor blade.

Table 2. Flexible piston accumulator prototype dimensions.

Inner Diameter, mm	Outer Diameter, mm	Total Length, mm	Stationary Weight, kg
250	269.2	1995	89.78

The test requirement of maximum diameter increase of 0.1 mm is so conservative that it can only be achieved by relatively small piston accumulators. Applying this requirement to the FW types for a multi MW WT leads to oversizing of the wall thickness of the piston accumulators. Therefore, the maximum diameter increase is slackened to 0.3 mm, which is a commonly used value for steel accumulators. A larger diameter increase poses a challenge for the piston rings, as they must not extrude into the gap between liner and piston. However, a 0.3 mm diameter increase is a feasible value that is confirmed by piston accumulators that have been operating for a long time.

4. Carbon Fibre-Reinforced Plastic Flywheel Types

4.1. Geometry

The possible installation spaces for the tip accumulators are limited by the dimensions of the airfoils of the Sandia 61.5 m blade design. In this blade, like in all state-of-the-art rotor blades, the space inside the blade decreases towards the blade tip. As a result, a single, double, or triple tip accumulator can be installed inside the blade, in order to achieve the desired increase of the inertia of the NREL 5 MW WT.

The properties of the CFRP tip accumulators of the three selected FW types are summarised in Table 3, where rotor radius is the maximum rotor radius that can be achieved by the tip accumulators. This data is further needed in the mass and load comparison in Sections 4.2 and 5.

Table 3. Properties of the CFRP piston accumulators of the three FW types.

Flywheel Types	No. of Tip Accumulators	Rotor Radius, m	Inner Diameter, mm	Total Length, mm
Type I	1	40.01	577	5477
Type IV	3	Each at 61.6	224, 209, and 149	5966, 5957, and 5920
Type VI	2	Each at 46.6	443 and 241	5047 and 4923

Based on the information about the CFRP tip accumulators' properties mentioned in Table 3, the proposed installation spaces inside the Sadia 61.5 m rotor blade are illustrated in Figure 4.

4.2. Masses Comparison

In order to design the CFRP piston accumulators for the different FW types, according to the prototype specifications (see Table 1), again, COMPOSITOR is applied. For this purpose, the model specifications of the prototype, as introduced in Section 3.3, are used to model the CFRP accumulator as needed for the three FW types. The three FW types that are mentioned in the Introduction Section are analysed, and the wall thicknesses of the CFRP accumulators are computed according to the working pressure of each FW type and to the maximum permissible diameter increase of the steel accumulator, as discussed above.

As a result, simulations of the CFRP piston accumulators for the FW systems in COMPOSITOR have shown that in addition to the flexibility of the CFRP piston accumulator, also, the total stationary mass is decreased compared to conventional steel piston accumulators. This is due to the special technology used by winding the carbon fibre in circumferential, longitudinal, and hoop and helical (e.g., ±40° relative to axial direction) directions around the steel liner of the piston accumulator, see Figure 7.

Consequently, the design of the flexible piston accumulator is noticeably lighter than the conventional steel design. Table 4 and Figure 10 compare the properties and the masses of both CFRP and conventional steel piston accumulators for the three FW types mentioned in the Introduction Section. In Figure 10, the CFRP accumulators and the conventional steel accumulators are represented as CFRP + Liner and as Steel in blue and red, respectively. The masses represented in Figure 10 are the total stationary masses of root and tip accumulators of each FW type, where type I has only one tip

accumulator. Type IV and type VI have three and two tip accumulators, respectively. Figure 10 shows the obvious weight reduction of the total stationary masses of the root and the tip accumulators for the CFRP design compared to the conventional steel design for all represented FW types. The effect of this weight reduction on the impact of the mechanical loads of the WT is discussed in the next section.

Table 4. Properties of the CFRP and the conventional piston accumulators of the three FW types.

Flywheel Types	CFRP + Liner Accumulators						Steel Accumulators					
	Type I	Type IV			Type VI		Type I	Type IV			Type VI	
No. of tip accumulators	1	1	2	3	1	2	1	1	2	3	1	2
Wall thickness mm	4.24	Each 3.72			Each 3.72		3	Each 3			Each 3	
Working pressure bar	13.9	Each 31.6			Each 18.7		13.9	Each 31.6			Each 18.7	
Material	carbon fibre Toho tenax STS40 and→S335 steel liner						34CrMo4 steel					

(a)

(b)

Figure 10. *Cont.*

(**c**)
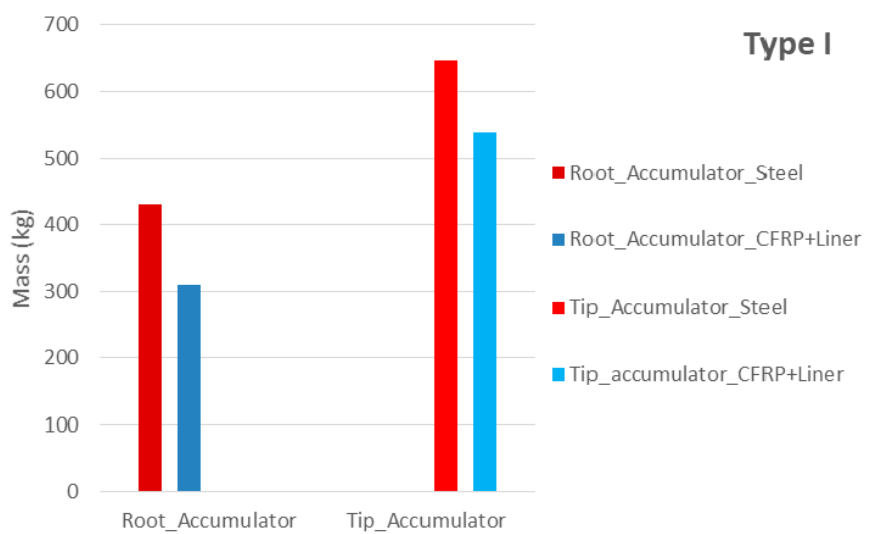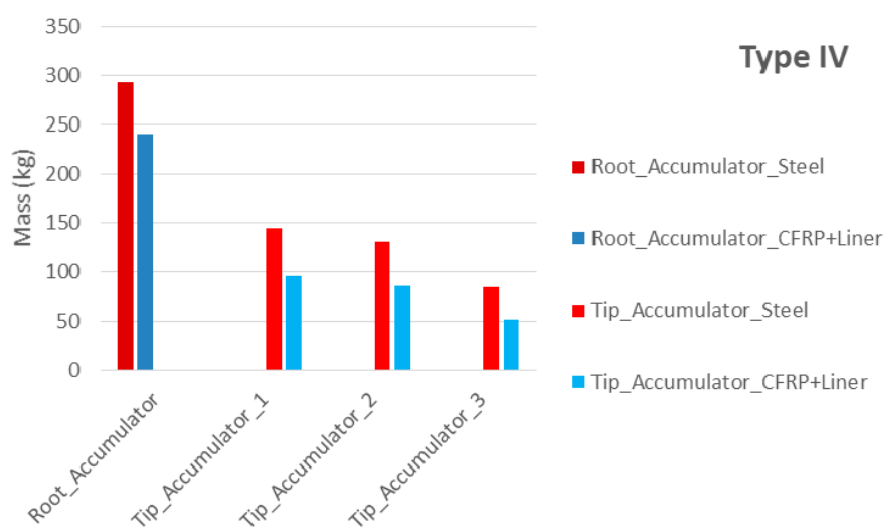
Figure 10. Mass comparison of blade tip and blade root accumulators from steel and from CFRP with steel liner for (**a**) type I, (**b**) type IV, and (**c**) type VI.

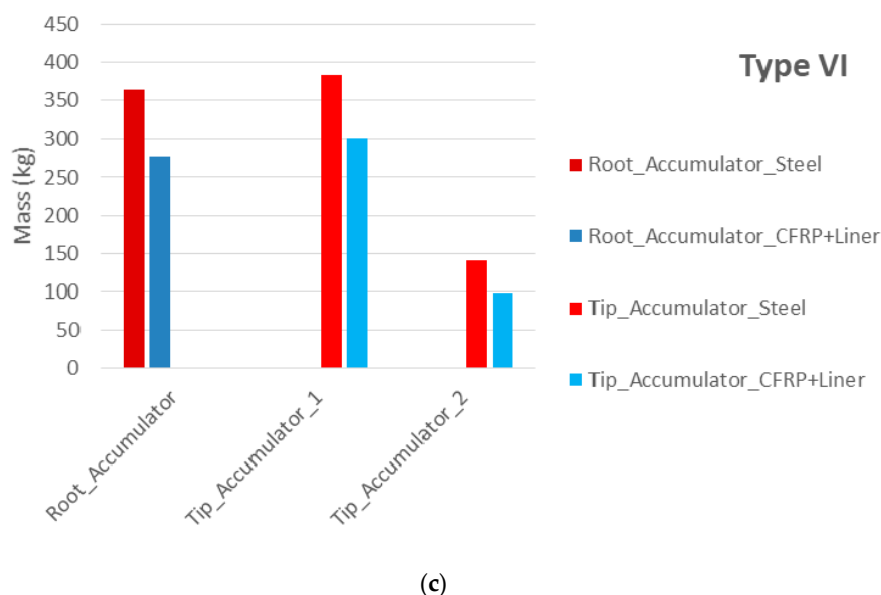## 5. Load Analysis

The load analysis aims to quantify the effect of the weight reduction of the CFRP piston accumulators on the impact of the mechanical loads of the NREL 5 MW WT. The quantifying of loads is done firstly by computing the mechanical loads of the original WT without a FW system in order to get reference load values. Afterwards, load simulations are done for the WT with a FW system comprising CFRP accumulators as well as with a FW system comprising conventional steel accumulators in the rotor blades. Eventually, the deviations of the mechanical loads from the reference values illustrate the impact of the different FW system designs on the mechanical loads of the WT.

For this analysis, the program FAST is used. FAST is an aeroelastic computer-aided-engineering tool developed by NREL [4], that allows for computing mechanical loads in a wind turbine.

As described in previous work of the author [6], the methodology used to implement the variable behaviour of the FW system in FAST considers the FW system statically, i.e., either the system is fully charged or fully discharged. In state-of-the-art WTs, the rotor blade inertia does not vary during operation. Therefore, all common load simulation tools, like Felx5 (http://www.dtu.dk, v5, Technical University of Denmark, Kgs. Lyngby, Denmark), FAST (https://nwtc.nrel.gov/FAST8/), or Bladed [11], are unsuitable for simulating the dynamic operation of the FW system. This would require drastic adaptations of the source code of such load simulation tools. Future work will focus on implementing variable blade inertias in a load simulation tool to allow for the simulation of the dynamic operation of a FW system in a WT rotor.

The structural blade properties of the Sandia 61.5 m rotor blade design are described in FAST as sectional distributed mass densities and stiffnesses. Each section with its mass and stiffness is at a particular location in the spanwise direction of the blade. These locations are also the locations where cross-sections of the airfoil are illustrated in Figure 4. As the eigenmodes characterise the structural properties of the rotor blade, FAST requires also the mode shape coefficients of the first three eigenmodes. The impact of the FW system on the structural properties of the rotor blade is implemented in terms of increasing the mass density at those nodes of the blade, where the root and the tip accumulators are installed. Regarding the state of the charge of the FW system, the fluid mass is shifted between the tip accumulator and the root accumulator, i.e., if the FW system is charged, the complete fluid mass is added to the mass density of the nodes of the blade tip, where the tip accumulator is located. If the FW system is discharged, the complete fluid mass is added to the mass

density of the nodes of the blade root where the root accumulator is located. These two scenarios are done for the three previously mentioned FW types. Additionally, the mode shape coefficients of the first three eigenmodes are computed with BMode for both states of charge, due to the change of the blade section masses. Other structural properties of the blade input data remain unchanged.

In this paper, load simulation results of the cases "original WT without FW system" and "WT with conventional steel accumulator FW system" are obtained from previous work of the author [6]. Hence, it is mandatory for the load simulations of the WT with a FW system comprising CFRP accumulators to take the same design load cases (DLCs) and the same wind fields. Only in this way is it possible to compare load simulation results of both FW system designs with the original WT without FW system. The selected DLCs are based on the "IEC International Standard for the Design of Wind Turbines" and they cover the most important operation modes of a WT [12]. Thus, the computed ultimate and fatigue loads of the unchanged rotor blade and of the rotor blade with the conventional steel piston accumulators can be obtained from Hippel et al. [6]. The results of these simulations are used as reference values. Subsequently, load simulations are performed for the WT with FW system comprising the CFRP piston accumulators. Loads are computed for the WT with the FW types I, IV, and VI in charge and discharged state. The resulting ultimate and fatigue loads are compared to the reference values. Afterwards, the changes in ultimate and fatigue loads of rotor blade, tower, and drive train are evaluated, and potentially occurring structural blade failures are discussed.

At first, the change in ultimate loads of the blades, the drive train, and the tower of the 5 MW WT due to both designs of the FW system are discussed. Figure 11 depicts the change in ultimate loads as a percent increase in bending moments. The charged and the discharged states of the FW system with CFRP accumulators are represented in Figure 11 in dark red and dark blue, whereas the charged and discharged states of the FW system with conventional steel accumulators are shown in light red and light blue, respectively. The increase in bending moments when both FW designs are in a charged state are obviously greater than the bending moments when the FWs are in a discharged state. The reason for this is that the fluid mass in the charged state is added to the stationary mass of the tip accumulator, where the lever arm of the gravitation force has a larger distance to the centre of rotation. Also, the larger distance to the centre of rotation leads to larger centrifugal forces created by the fluid mass. Due to the stationary weight reduction of the CFRP accumulator, the increase in bending moments of almost all FW types is lower for the CFRP design compared to the conventional steel design. Excepted from this is the change in bending moment at blade cuts for FW Type IV in the charged state. Only in this scenario is the increase in bending moment of the CFRP design about 2% greater than the conventional steel design. The reason for this minor increase is the difference in WT operating points of both FW designs when the maximum turbulent wind speed hits the rotor blade.

The first and the second graphs in Figure 11 show the bending moments at the blade cuts, *SpnMLxB*, and the tower cuts, *TwHtML*, where the maximum increase of these moments are indicated. The variable names are based on the conventions used in FAST [5].

Finally, the change in fatigue loads are analysed in a similar procedure as for ultimate loads. Fatigue analysis is done twice for each FW design over the lifetime of 20 years of the WT. Once, the FW system is charged for 20 years, and once, again, the FW system is discharged for 20 years. This is, again, due to the fact that the dynamic behaviour of the FW system cannot be implemented in FAST.

Figure 12 compares the change in fatigue loads for both FW designs at the rotor blade, the tower, and the drive train of the 5 MW WT. The light red and the light blue bars in Figure 12 represent the charged and the discharged states of the conventional design of the FW system, respectively. The columns in dark red and in dark blue represent the charged and the discharged states of the CFRP design of the FW system, respectively.
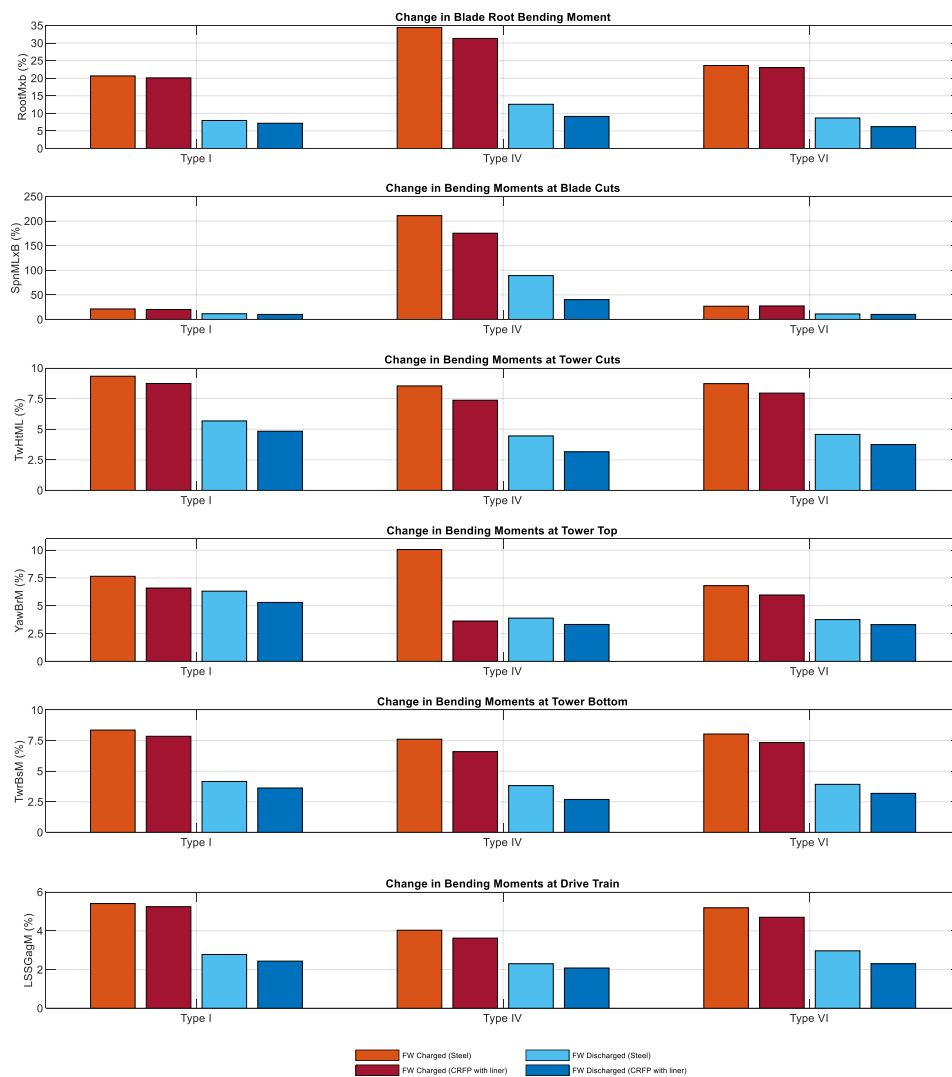
Figure 11. Comparison of changes in ultimate loads in (from top to bottom) blade root bending moment, bending moments at blade cuts, bending moments at tower top, bending moments at tower bottom, and bending moments at drive train, between steel accumulator and CFRP with metal liner accumulator for FW types I, IV, and VI in charged (red) and discharged (blue) status, both with respect to the ultimate loads of the original WT without FW system.

The change in fatigue-damage equivalent bending moment at the blade, the tower, and the drive train caused by the CFRP design of the FW system are obviously lower than the change in fatigue-damage equivalent bending moment caused by the conventional steel design. This is due to the difference of the stationary weight between the CFRP design and the conventional steel design of the piston accumulators. For the FW type IV, the fatigue equivalent bending moment at tower top in discharged state and at tower bottom in charged and discharged states are slightly decreased for both FW designs. This slight decrease of the fatigue bending moment can be traced to the low impact of type IV on the tower top and tower bottom during the simulation time of 20 years of operation.

Consequently, ultimate and fatigue failures are evaluated to ensure that there is no need for reinforcement in the original rotor blade design of the NREL 5 MW WT. The failure evaluation in this paper is based on the same methodology used by Hippel et al. [6], where the load simulation results were used to indicate ultimate and fatigue failures. The failure evaluation in a previous work of the author [6] showed that neither ultimate nor fatigue failure of the rotor blade was caused by the presence of the conventional steel accumulator FW system. Figures 11 and 12 show that the loads of

the CFRP FW design are in general lower than those of the conventional steel FW design. This leads to the conclusion that the increase in ultimate and fatigue loads due to the installation of the CFRP FW design cause neither ultimate nor fatigue failure of the rotor blade, since the WT model and the rotor blade design are the same for both load simulations. Hence, with the flexible CFRP accumulators as designed here, and with the methodology for designing a FW system with these accumulators, a FW system can be implemented in a WT rotor. Although the previous work already indicated that a FW system could be installed in a rotor without causing failure in the blades, there was always the shortfall that the conventional steel accumulators must not be bent. Therefore, a mounting technology would have been required that attaches the accumulators to the rotor blades, but that, at the same time, allows the rotor blade to bend around the accumulator without inflicting a bending moment on the accumulator. With the flexible CFRP accumulators, this problem is solved. These accumulators can be laminated to the structure of the rotor blade. Hence, the accumulators bend with the rotor blade, which is no problem for these flexible CFRP accumulators.
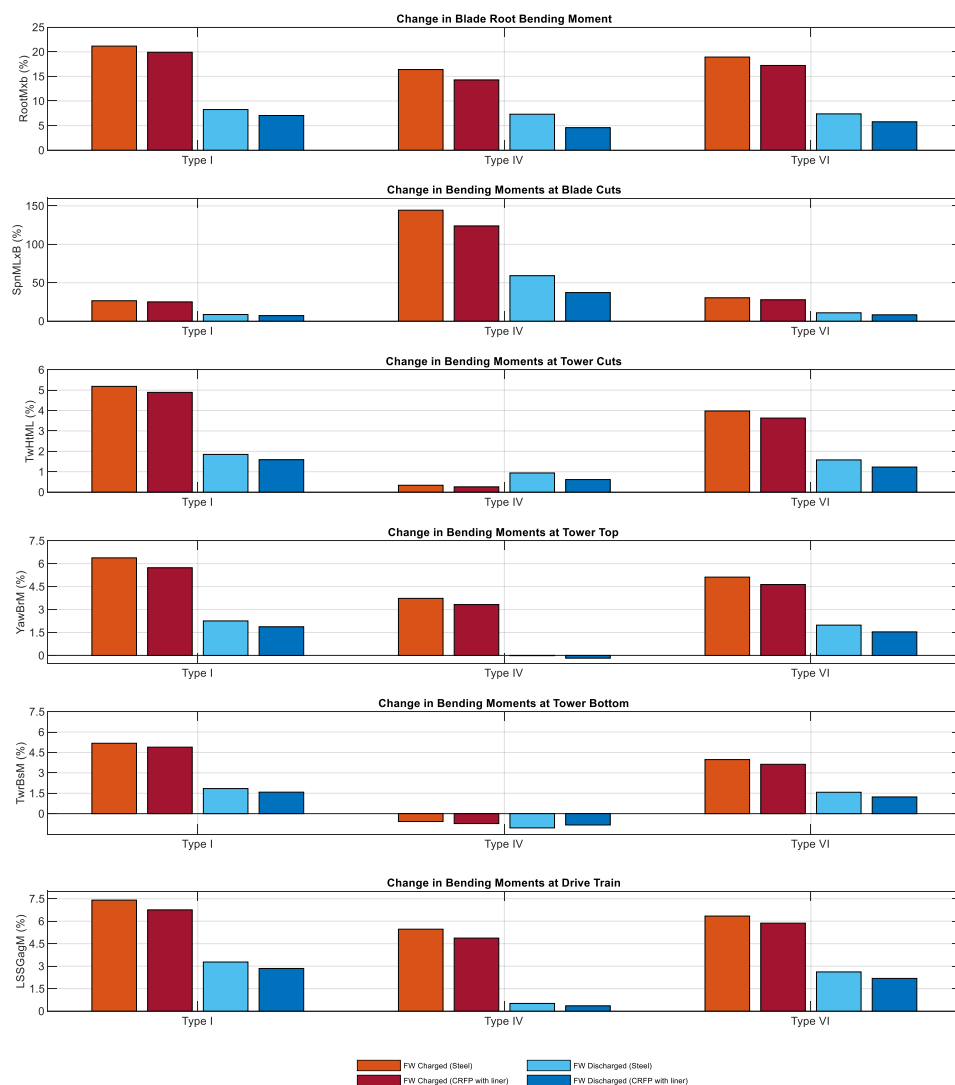
Figure 12. Comparison of changes in fatigue loads in (from top to bottom) blade root bending moment, bending moments at blade cuts, bending moments at tower top, bending moments at tower bottom, and bending moments at drive train, between steel accumulator and CFRP with metal liner accumulator for FW types I, IV, and VI in charged (red) and discharged (blue) status, both with respect to the ultimate loads of the original WT without FW system.

6. Conclusions

In the present paper, a CFRP piston accumulator design was presented for a FW system to be installed in a rotor blade of a WT. The development of such CFRP accumulators goes through different stages. Firstly, the bending behaviour of the considered rotor blade, here the Sandia 61.5 m rotor blade for the NREL 5 MW WT, was analysed, and the bending gradients were derived for the first and second eigenmodes. Subsequently, based on the derived bending gradient, a flexible CFRP piston accumulator prototype was specified, built, and tested. The design specifications of the prototype were used to derive the different piston accumulators needed for the FW system. Finally, ultimate and fatigue load comparisons were done between a WT with a conventional steel design of FW system, a WT with a flexible CFRP design FW system, and a WT without any FW system. The load comparison revealed that the increase in ultimate and fatigue loads of the blade, the tower, and the drive train due to the CFRP FW design are much smaller than the increase in these loads in case of the conventional steel FW design. Furthermore, the load analyses of the 61.5 m rotor blade revealed that neither ultimate nor fatigue failure occurred due to the installation of the CFRP FW design. Consequently, the initial design of the NREL 5 MW WT can take on the FW system without the need for reinforcement in the rotor blades.

It can be concluded that the main goal of designing a FW system made of piston accumulators that can be realistically implemented in rotor blades has be fully achieved. The mounting technology could not be simpler: the designed CFRP accumulators are allowed to bend with the rotor blade. Also, they are made of epoxy, which allows to laminate them to the glass fibre-reinforced plastic, of which the rotor blade is made.

With the methodology presented in the paper, a FW system can be designed for any arbitrary WT. Although the methodology is presented for the case of the NREL 5 MW reference WT, it can be applied to any other WT, too.

Future work will focus on designing FW types that take full advantage of the fact that the newly developed accumulators may be bent, i.e., the development of very long accumulators will focus on designing FW types where the fluid mass can move through most of the length of the rotor blade. In order to assess the effect of such FW types on the mechanical loads, it becomes even more important to adapt load simulation tools to this purpose. Hence, a load simulation tool that allows simulating variable blade inertias will need to be developed in the future.

References and Note

1. Jauch, C. A flywheel in a wind turbine rotor for inertia control. *Wind Energy* **2015**, *18*, 1645–1656. [CrossRef]
2. Jauch, C.; Hippel, S. Hydraulic-pneumatic flywheel system in a wind turbine rotor for inertia control. *Iet Renew. Power Gener.* **2016**, *10*, 33–41. [CrossRef]
3. Hippel, S.; Jauch, C.; Ritschel, U. Hydraulic-pneumatic flywheel configurations for controlling the inertia of a wind turbine rotor. *Wind Eng.* **2019**, *43*, 114–132. [CrossRef]
4. Jonkman, J.; Butterfield, S.; Musial, W.; Scott, G. *Definition of a 5-MW Reference Wind Turbine for Offshore System Development*; NREL/TP-500-38060; NREL: Denver, CO, USA, 2009; p. 947422.
5. Jonkman, J.M.; Buhl, M.L., Jr. *FAST User's Guide—Updated August 2005*; NREL/TP-500-38230; National Renewable Energy Lab. (NREL): Golden, CO, USA, 2005; p. 15020796.

6. Hippel, S.; Jauch, C. Load analysis of hydraulic-pneumatic flywheel configurations integrated in a wind turbine rotor. *Wind Energy* **2019**, *22*, 1190–1202. [CrossRef]

7. Resor, B. *Definition of a 5MW/61.5m Wind Turbine Blade Reference Model*; SAND2013-2569; National Renewable Energy Lab. (NREL): Livermore, CA, USA, 2013; p. 1095962.

8. Bir, G. *User's Guide to BModes (Software for Computing Rotating Beam-Coupled Modes)*; NREL/TP-500-39133; National Renewable Energy Lab. (NREL): Golden, CO, USA, 2005; p. 861489.

9. Fischer, O.; Mannigel, M.; Preller, F. COMPOSITOR Hilfsmittel zur Analyse von Laminaten aus Faserverbundkunststoffen Bedienungsanleitung Version 4.1. 2009.

10. Barlow's Formula. Available online: https://www.amerpipe.com/reference/charts-calculators/barlows-formula/ (accessed on 16 August 2020).

11. NWTC Programmer's Handbook: A Guide for Software Development within the FAST Computer-Aided Engineering Tool—PDF Free Download. Available online: https://docplayer.net/19117568-Nwtc-programmer-s-handbook-a-guide-for-software-development-within-the-fast-computer-aided-engineering-tool.html (accessed on 7 July 2020).

12. IEC 61400-1:2019—IEC-Normen—VDE VERLAG. Available online: https://www.vde-verlag.de/iec-normen/247153/iec-61400-1-2019.html (accessed on 8 July 2020).

PAPER • OPEN ACCESS

A Resource-Efficient Design for a Flexible Hydraulic-Pneumatic Flywheel in Wind Turbine Blades

To cite this article: L Alhrshy and C Jauch 2022 *J. Phys.: Conf. Ser.* **2265** 032018

View the article online for updates and enhancements.

You may also like

- Radial stiffness improvement of a flywheel system using multi-surface superconducting levitation
  Sinan Basaran and Selim Sivrioglu

- Modelling, simulation, and experimental verification of a pendulum-flywheel vibrational energy harvester
  Yifeng Wang, Mingyuan Gao, Huajiang Ouyang et al.

- Influence of the flywheel profile on the energy storage capacity of the kers system
  L Milica and G Andrei

A Resource-Efficient Design for a Flexible Hydraulic-Pneumatic Flywheel in Wind Turbine Blades

L Alhrshy and C Jauch

Wind Energy Technology Institute (WETI), Flensburg University of Applied Sciences, Kanzleistraße 91-93, 24943 Flensburg, Germany;

laurence.alhrshy@hs-flensburg.de

Abstract. The utilization of renewable energy resources significantly increases in order to reduce the impact of climate change. Wind turbines are one of the most important renewable energy sources and have an important role to play in power generation. They do, however, have to serve the increasingly variable demands of the grid. Some of these demands cannot be satisfied with the standard control mechanisms of state-of-the-art wind turbines. A hydraulic-pneumatic flywheel in a wind turbine rotor is one mechanism which, in addition to its various grid services, can also reduce the mechanical loads on the structure of a wind turbine. However, the installation of such a flywheel into rotor blades increases the weight of the blades. This paper focusses on the development of a design method for reducing the additional mass of the flywheel. This method incorporates the piston accumulators of the flywheel in the blade support structure, which allows for the replacement of parts of the blade spar caps with composite material from the piston accumulators. This enables the flywheel to be installed into the rotor blades without making the wind turbine significantly heavier.

1. Introduction

When replacing conventional power plants with wind turbines (WTs), the demanding requirements of the grid need to be considered. Some of these requirements can only be satisfied with additional control mechanisms in the WTs. The mechanism presented in this paper involves the incorporation of a hydraulic-pneumatic flywheel (FW) in a WT's rotor.

The hydraulic-pneumatic FW functions by moving a fluid mass between a tank in the blade root and one or more piston accumulators near the blade tip. Figure 1 shows the components of such a FW with only one tip accumulator. To charge the hydraulic-pneumatic FW at any arbitrary rotor speed, electrically-driven pumps move the fluid to the blade tip. The hydraulic-pneumatic FW is discharged by means of compressed nitrogen, which is stored in containers in the blade body.

The feasibility of the concept of incorporating a FW in a WT's rotor has been shown and improved since 2014 [1]. The initial proposal for a FW had solid weights at either end of the blade connected by a spiral spring [1]. In order to improve the response of this FW to the dynamic behavior of rotor blades, a further proposal was made to replace the solid weights and spiral spring with a hydraulic-pneumatic FW containing steel piston accumulators [2]. The initial steel piston accumulators would have been heavy, rigid and unbendable [3]. Furthermore, the addition of weight at the blade tip would cause significant increases in ultimate loads as well as in fatigue loads of all WT components, even when the FW is fully discharged and not in operation [4]. The configuration of the unbendable steel piston accumulators of the hydraulic-pneumatic FW in terms of their geometry, position and number was previously proposed so as to allow the blades to bend without bending the piston accumulators [3]. Due
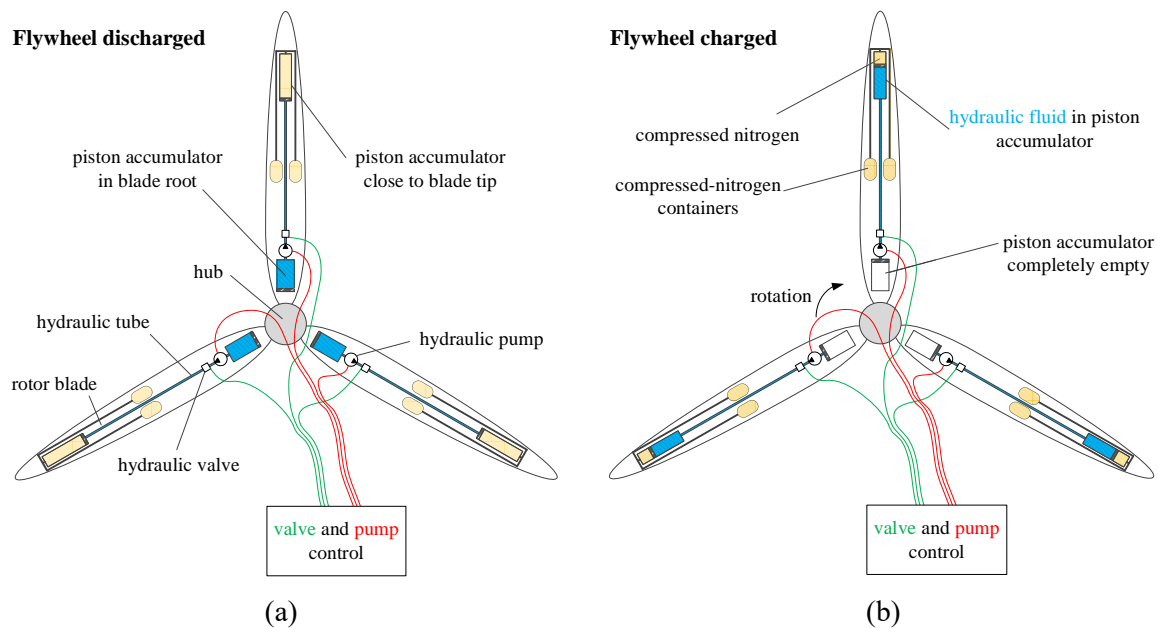
Figure 1. Simplified sketch of a hydraulic-pneumatic FW: (a) FW in discharged state and (b) FW in charged state.

to this restriction, several desirable positions of the steel piston accumulators in the blade are not feasible. In order to overcome the disadvantages of the steel piston accumulators, further research in cooperation with HYDAC Technology GmbH resulted in the development of a hybrid design of piston accumulator using carbon fibre-reinforced plastic (CFRP) with a steel liner [5]. This is lighter than the initial steel design and can bend when the rotor blade bends. The bending capability of composite materials allows piston accumulators to be integrated into the support structure of the rotor blade. Consequently, the piston accumulators can substitute part of the material used in the spar caps of the blade, i.e. they can take over some of the loads, which otherwise have to be borne by the original support structure of the blade.

The present article provides as algorithm for the configuration of the hydraulic-pneumatic FW as a part of the blade structure. The algorithm iteratively replaces parts from the blade spar caps with the material from the piston accumulator, in order to minimize the additional stationary masses in the rotor blades. As a result, several configurations based on the various functionalities of the FW have been derived. The underlying basic requirement is always that the FW increases the rotor inertia dynamically by 15%.

In section 2, the various functionalities of the hydraulic-pneumatic FW are briefly introduced. Based on these functionalities, the installation radius of the tip accumulators is derived. Section 3 presents the changes in the blade masses and stiffnesses due to the introduction of the tip accumulators as part of the blade support structure. In section 4, the methodology used to derive the FW configurations is illustrated in a flow diagram. The resulting configurations from section 4 and their effect on the blade eigenfrequencies are discussed in section 5. Finally, section 6 summarizes the findings and provides an outlook on future work on this topic.

2. Applications for a hydraulic-pneumatic flywheel

Numerous applications for FWs in WT rotor blades were previously described [6], both for the requirements of the grid as well as for the reduction in mechanical loads on the WT. These applications are associated with the amount and the speed of release or storage of kinetic energy by the FW [6]. In this section, the focus is on the effect of the kinetic energy on these applications.

The FW applications described in [6] are briefly described below in order to illustrate their relationship to kinetic energy.

2.1. Steadying power infeed

Variations in the power production of a WT are mainly caused by high-frequency wind turbulences. These variations can be mitigated within seconds by changing the direction of energy flow in a FW contained within the blade of the WT. Steadying the power infeed also steadies the rotational speed of the WT rotor and reduces pitching actions. Both reduce the mechanical loads on the WT.

2.2. Grid frequency support and power system stabilization

In normal operation, the grid frequency permanently varies around its rated value, provided that the balance between generation and demand can be maintained at all times. Methods for supporting or stabilizing the grid frequency are based on the adjustment of the active power of generators. WTs with a FW in their rotor can respond to grid frequency variations by injecting or consuming power for a short duration with hardly any impact on their rotational speeds.

2.3. Mitigating excitations from gravitation and wind share

The impact of gravitation on the blade root bending torque can be controlled via the Coriolis forces of the hydraulic-pneumatic FW. Similarly, aerodynamic rotor imbalance, resulting from wind shear, can be mitigated with centrifugal forces of the FW. These examples of mechanical load reduction enable the FW to asynchronously vary its state of charge with every rotation of the rotor.

Static balancing of the rotor, damping in-plane vibrations of the rotor and the tower, emergency braking, and low-voltage ride-through are also applications of the hydraulic-pneumatic FW [6].

A hydraulic-pneumatic FW in a WT rotor varies the moment of inertia of the WT rotor in order to release or store kinetic energy. Regarding the law of conservation of angular momentum, the kinetic energy, E_{kin}, in a rotational system is a function of the moment of inertia, J, and the angular velocity ω.

$$E_{kin} = \frac{1}{2} \cdot J \cdot \omega^2 \tag{1}$$

The moment of inertia of a FW, J_{FW}, can be varied by changing the variable distance, R_{var}, between the centre of gravity of the shifted fluid mass, m_{fluid}, and the centre of rotation. Equations (2) and (3) describe the FW inertia of a three-blade WT.

$$J = J_{rotor} + J_{FW} \tag{2}$$

where, J_{rotor}, is the rotor inertia.

$$J_{FW} = 3 \cdot R_{var}^2 \cdot m_{fluid} \tag{3}$$

Equations (1), (2) and (3) show that the controlled kinetic energy of the hydraulic-pneumatic FW, E_{kin}, is proportional to the square variable radius, R_{var}^2. This means that the closer the piston accumulators are installed to the blade tip, the smaller the fluid mass, m_{fluid}, needs to be to achieve the desired kinetic energy of the hydraulic-pneumatic FW. The input parameters for the configuration algorithm in section 5 are selected on the basis of this fact. However, previous research [4] showed that the blade root bending moment increases with increasing installation radius of the piston accumulators. The prime cause for this is the additional stationary masses of the tip piston accumulators. Therefore, the following section presents a method which has been developed to minimize this additional mass.

3. Incorporating the flywheel as a part of the blade support structure

Previous load analyses of a WT containing a hydraulic-pneumatic FW with steel piston accumulators in its rotor showed that the mechanical loads increased on all WT components even when the FW is fully discharged [6-7]. This is due to the additional stationary masses of the piston accumulator in the blade tips. As these accumulators are designed to be made of composite material in the current proposal and, more importantly, to be bendable, it is possible to incorporate them into the support structure of the rotor blade. The objective of the present study is to minimize the additional masses by replacing parts of the

blade spar caps (SCs) with the tip accumulators of the FW. This allows the FW to be installed in the rotor blades without significantly increasing the mass of the blades.

To illustrate the effect on the blade structure of replacing SC material, Figure 2 provides a blade cross section before and after the modification. Due to the nature of the compact and heavy unidirectional (UD) composite material used for the SCs to support the bending stiffness of the blade, the majority of the total mass of the blade is concentrated in the SCs [7]. The piston accumulators and the blade SCs are both made of composite materials, which makes material replacement homogenous. Therefore, it seems an obvious choice to replace UD material of the SCs rather than the foam or the balsa of the blade with material from the piston accumulator.

In order to limit the inevitable increase in blade weight to a minimum, the SC thicknesses are decreased from t_SC to t_SC*. Figure 2 (b) shows the changes in the cross-sectional structure of the blade due to the installation of a piston accumulator with radius R_Acc and wall thickness t_Acc.
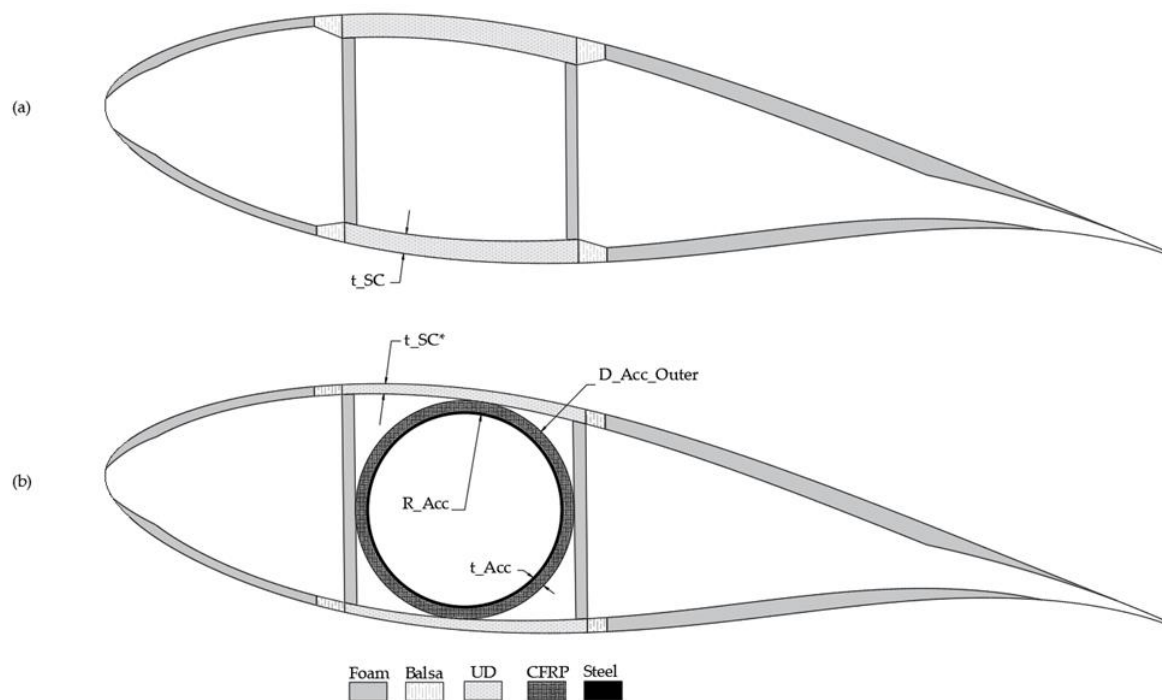
Figure 2. Schematic drawings of (a) initial blade cross-section without tip accumulator, (b) modified blade cross-section with tip accumulator.

However, since the SCs are structural components that support the blade bending stiffness, any modification to their thickness leads to changes in blade bending stiffness. To quantify the impact of a modification, two analyses were performed: (i) the static eigenfrequency of the blade; and (ii) the change in the tip deflection at the rated power. The analyses are described in section 5. The results of these analyses are significantly influenced by the considered FW configuration.

4. Configuration of the hydraulic-pneumatic flywheel
The methodology presented in this section is based on an algorithm, which applies an iteration loop to acquire optimal FW configurations, see Figure 3. The installation radius of the FW accumulator, R, i.e.

the outer radius where the FW accumulator is closest to the blade tip, is determined at the beginning of the algorithm.

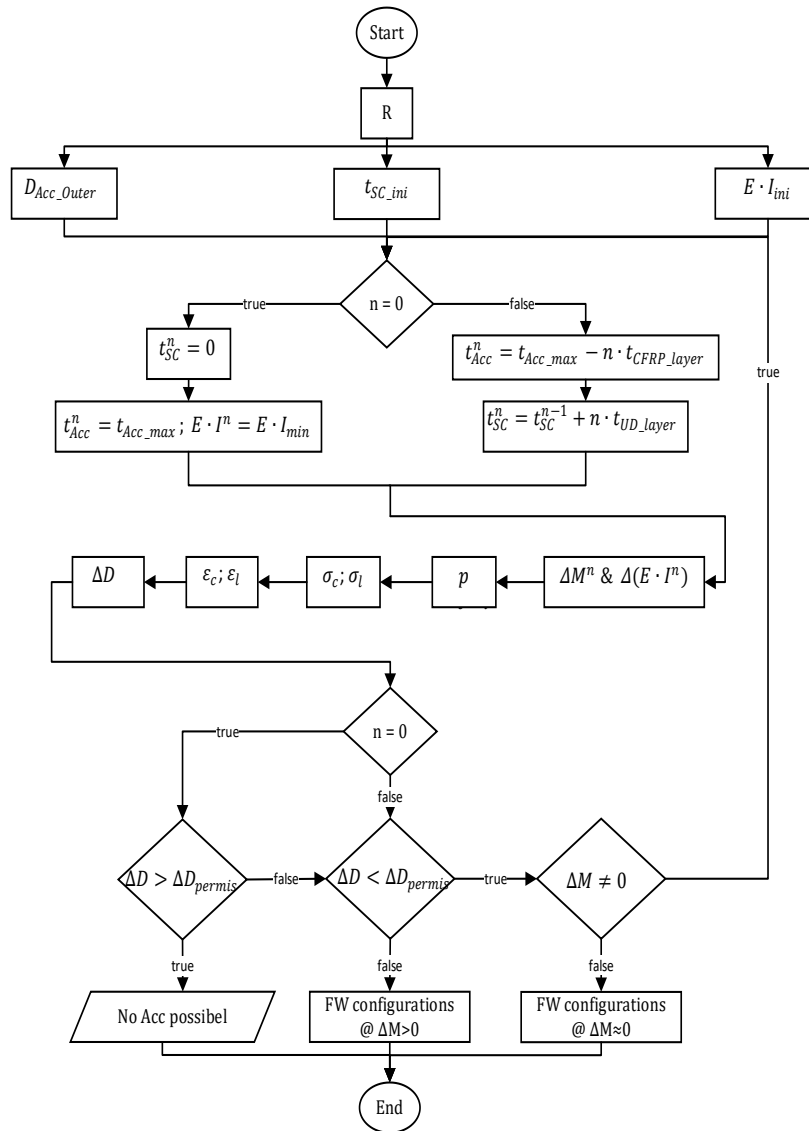**Figure 3.** The iterative process for computing the minimum tip accumulator thickness and the resulting FW configurations.

Based on this radius, the accumulator outer diameter, D_{Acc_Outer}, the initial SC thickness, t_{SC_ini}, and the initial cross-sectional bending stiffness, $E \cdot I_{ini}$, in terms of Young's modulus, E, of the material and the initial moment of inertia I_{ini} are defined. Initially, the tip accumulator was designed to completely replace the SCs in order to verify whether a piston accumulator can be installed at this radius. For this initial condition, the maximum tip accumulator wall thicknesses. t_{Acc_max}, and the minimum cross-sectional binding stiffness, $E \cdot I_{min}$ were computed. The changes in the mass, M, and the bending stiffness, $E \cdot I$, of the modified cross-section of this initial accumulator were quantified in terms of ΔM^n & $\Delta(E \cdot I^n)$, where, n, is the iteration step. Subsequently, the calculated working pressure on the piston accumulator, p, was translated into a circumference stress, σ_c, and a longitudinal stress; σ_l, using Barlow's formula. These stresses were used to calculate the strains in circumferential direction, ε_c and in longitudinal direction, ε_l, based on classical laminate theory. The resulting circumference strain was

transformed into an increase in the diameter of the shell of the accumulator, ΔD. It should be noted that ΔD should not exceed the permissible diameter increase, ΔD_{permis}, of 0.3 mm; otherwise, the piston accumulator would no longer be able to separate the gas from the fluid in the accumulator, i.e. gas from the gas chamber could leak into the fluid chamber and vice versa. In the iteration process, when the increase in diameter, ΔD, was lower than the permissible limit, and the change in the cross-sectional mass, ΔM, was not equal to zero, the wall thickness of the tip accumulator, t_{Acc}, was decreased, while the SCs thickness, t_{SC}, was increased iteratively. This iteration was continued until one of the aforementioned conditions was met. The wall thickness of the piston accumulator and the thickness of the SCs were modified depending on the thickness of a single layer of the CFRP and the UD composite material. As a result, numerous FW configurations were derived, which differ in the length and the positioning of the tip accumulator and the fluid mass, as well as the impact on the cross-sectional bending stiffness of the blade. A basic constraint in this algorithm is always that each configuration has to be able to dynamically increase the rotor inertia by 15%. The major advantage of the method applied in the presented algorithm is that the mass of the tip accumulator only marginally increases the total blade mass.

5. Results

The aforementioned methodologies for configuration and incorporation of the hydraulic-pneumatic FW as a part of the blade support structure can be applied for different WT rotor blade designs. The results discussed in this section were obtained using the AE 4.0-68.7 blade design. This rotor blade has a total length of 68.7 m and was developed by AEROVIDE GmbH for a 3-blade, pitch-regulated, variable-speed WT with a rated power of 4.0 megawatt (MW). This WT is designed according to the Guideline for the Certification of Wind Turbines Edition 2010.
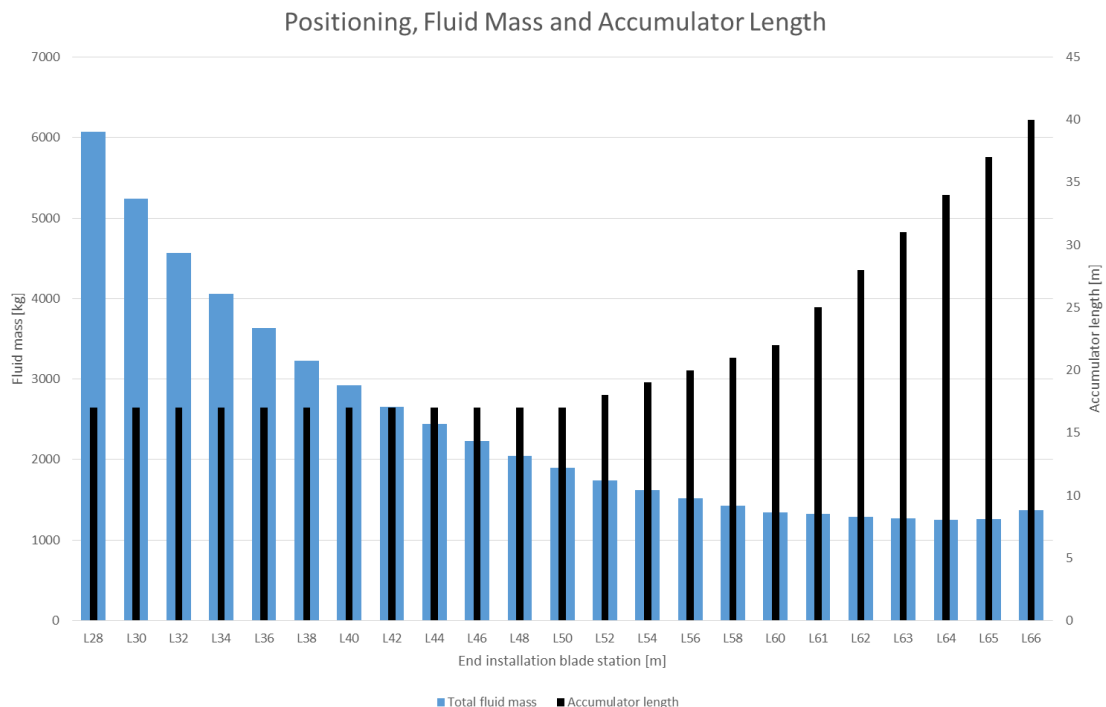

Figure 4. Possible FW configurations where one piston accumulator is located with its outer lid at the end installation blade station. Each configuration achieves a dynamic inertia increase of 15 %. The length of the accumulator as well as the fluid mass were determined by using the space inside the blade profile and the distance to the centre of rotation.

Figure 4 shows the weight of the fluid mass and the length of the piston accumulator at end installation blade stations between 66 m and 28 m for a FW with only one piston accumulator. The end installation blade station is the distance from the blade root to the point where the piston accumulator ends. The required length of the piston accumulator to achieve the 15% increase in the rotor blade inertia is dependent on the blade geometry, which in turn determines the maximum outer diameter of the piston accumulator. As the blade narrows towards its tip, the diameter decreases and the length of the tip accumulator significantly increases. The fluid mass, on the other hand, increases towards the blade root in order to keep the change in the blade inertia at 15% when the variable radius, R_var, decreases, see equation (2).

Figure 4 shows that in the FW configurations with only one piston accumulator, both the fluid masses and the piston accumulator lengths are extremely high. Therefore, the need to fully utilize the available space at every end installation blade station is very important. Figure 5 presents two FW configurations at different installation blade stations with four piston accumulators in each configuration. Configuration 1 in Figure 5 (a) represents an ultimate use of the available cross-sectional space at the 64 m end installation blade station. This configuration is more suitable for FW applications that require higher variable distance, R_{var}, see section 2. Configuration 2 in Figure 5 (b) is installed at the 36 m blade station. This configuration has two advantages: (i) the 4 piston accumulators have the same diameter, which insures that they behave identically when charging/discharging the FW; and (ii) this configuration leads to lower mechanical loads on the WT than configuration 1 when the FW is statically fully charged. Hence, configuration 2 may be suitable for the FW applications that are more frequent in a fully-charged state.

(a)

(b)
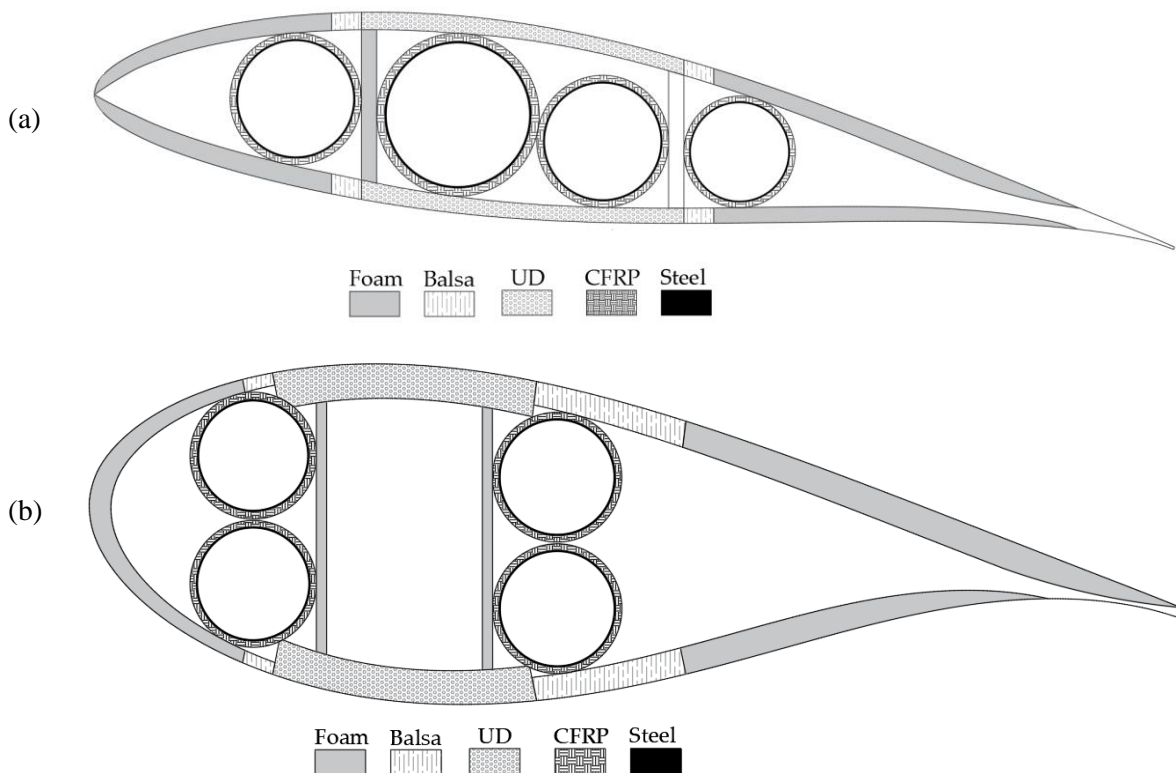
Figure 5. Schematic drawing of (a) FW configuration 1 with end installation at the 64 m blade station, (b) FW configuration 2 with end installation at the 36 m blade station.

Table 1 summarizes the FW configurations 1 and 2 for an increase in rotor inertia of the AE 4.0-68.7 blade design by 15%. The gas containers for discharging the FW are also listed in Table 1. The movable masses in the fluid side of the piston accumulators and in the gas containers are a water-glycol mix and nitrogen, respectively.

Table 1. FW configurations 1 and 2 for an increase in rotor inertia of the AE 4.0-68.6 WT by 15%

		No. of accumulators or gas containers per blade	Inner diameter of cylinders (mm)	End installation blade station (m)	Length of cylinders (m)	Movable mass (kg) per blade
Configuration 1	Accumulators	4	168.5, 188.9, 132.7, 115.5	Each at 64	8	581.3
	Gas containers	4	Each 193.3	Each at 20	10	53.2
Configuration 2	Accumulators	4	Each 300	Each at 36	11	3066.8
	Gas containers	4	Each 317.2	Each at 20	10	160.8

The impact of the FW in the discharged state on the mechanical properties of the blade is discussed below in terms of the change in bending stiffness for the FW configurations listed in Table 1. The percentage change in the cross-sectional mass, ΔM, and bending stiffness in the flapwise direction, ΔEI_x, for the FW configurations 1 and 2 is depicted in Figure 6 (a) and Figure 6 (b), respectively. A decrease in the SC thicknesses to keep the additional mass, ΔM, to a minimum, leads to a decrease in the flapwise bending stiffness, ΔEI_x. However, the decrease in ΔEI_x for FW configuration 2 is much lower than that for FW configuration 1. This is because of the differences in the positioning of the piston accumulators in the cross-section and their distances to the cross-sectional center of gravity, see Figure 6 (a) and (b). The gas containers are installed between blade stations 10 m and 20 m without any replacement of the material of the SCs. Therefore, the cross-sectional masses and stiffnesses increase at these blade stations. The increases in the flapwise bending stiffness at the installation blade stations for the gas containers can be used to counteract the decrease in the blade stiffness at the installation blade stations for the piston accumulators.

(a)   (b)
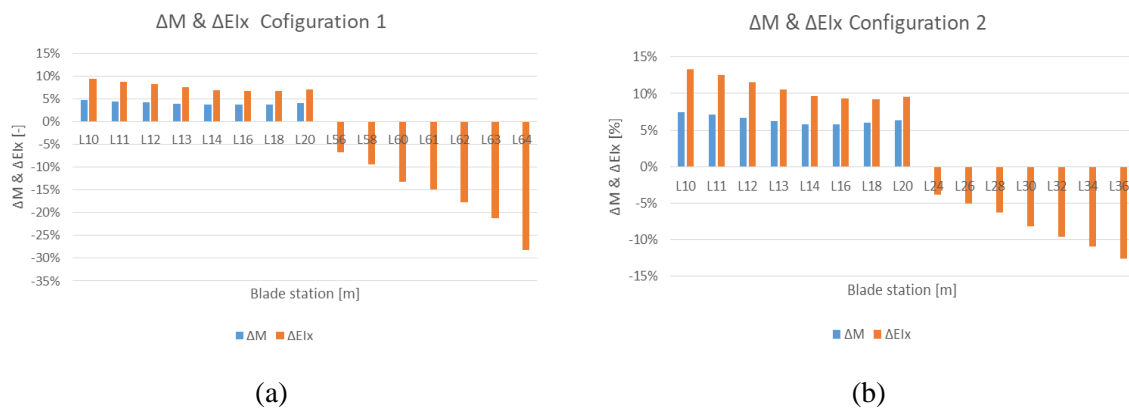
Figure 6. The impact of FW configuration 1 (a), and FW configuration 2 (b) on the cross-sectional mass and bending stiffness in flapwise direction. The FW is in a discharged state.

Relocating the fluid mass along the blade leads to changes in the eigenfrequencies of the blade. As the 1st eigenmodes are those which have the largest impact on behaviour of the rotor blades [8], Figure 7 (a) compares a percentage change in the 1st flapwise eigenfrequencies of the FW configurations 1 and 2 to the initial eigenfrequencies of the AE 4.0-68.7 blade. Both configurations in the discharged state lead to a minimum decrease in the 1st flapwise eigenfrequency by less than –1%. However, the decrease in the 1st flapwise eigenfrequency of FW configuration 1 in the charged state is –20%. This decrease is much lower than for FW configuration 2 in the charged state, which is only –2%. Depending on the FW application, the change in the blade eigenfrequencies can be actively used to detune the blade eigenfrequencies in order to mitigate fatigue from vibrations. For completeness sake, Figure 7 (a) also

shows the change in the 1st edgewise frequencies, as these are also relevant for the mechanical loads on the whole WT. Figure 7 (b) shows examples of the effect of the change in the blade tip masses on the blade tip deflection for FW configurations 1 and 2. The change in the tip deflection in the charged state compared to the discharged state for FW configuration 1 (in blue) and 2 (in orange) is depicted in percentage terms in Figure 7 (b). The tip deflection of configuration 1 is reduced by more than –4%, whereas it is only negligibly reduced in the case of configuration 2. The reason for this behavior is centrifugal stiffening where the fluid mass in the accumulator increases the blade tip masses, leading to greater centrifugal force. The analyses of the eigenfrequency and the blade tip deflections were computed with the load simulation tool HAWC2.
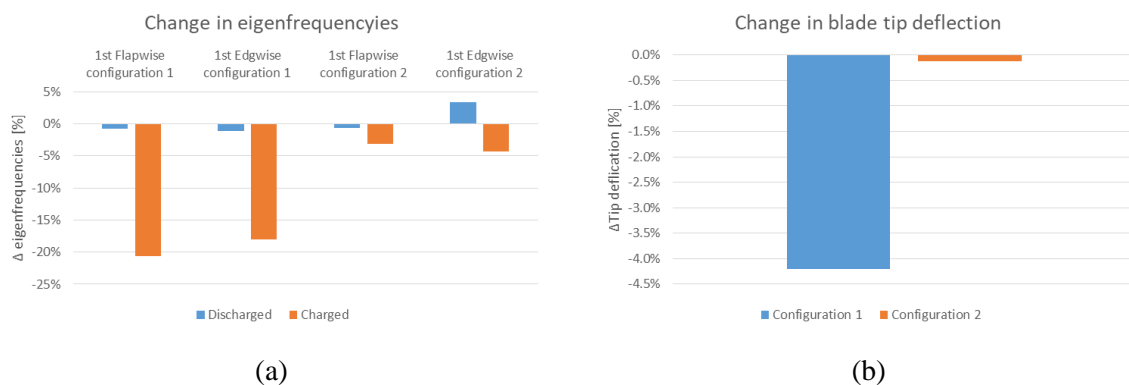

Figure 7. The impact of the FW configurations on (a) the first eigenfrequency, (b) the blade tip deflection when the FW is in a discharged state.

6. Conclusion

Previous studies of a hydraulic-pneumatic FW considered the piston accumulators to be foreign components inside the rotor blades of WTs [3-4]. This is because the piston accumulators were made of steel, which made them heavy and unbendable. Moreover, such heavy steel components increased the weight of the rotor blades significantly. Hence, these are two aspects which define the novelty of the methodologies presented in this paper: (I) piston accumulators can be used as a support structure in the rotor blade of a wind turbine and (II) the additional masses resulting from incorporation of piston accumulators can be minimized by replacing parts of the blade support structures with material from the piston accumulators.

An iterative process is performed to configure the geometry, position and number of the flexible hybrid piston accumulators of the hydraulic-pneumatic FW in order to obtain an increase of 15% in the rotor inertia of the AE 4.0-68.7 blade design. As a result, two configurations were selected which can satisfy the requirements of the various applications of the hydraulic-pneumatic FW. Configuration 1 has 4 piston accumulators of different radii positioned at the end installation blade station of 64 m; and configuration 2 has 4 piston accumulators of equal radii at the end installation blade station of 36 m.

A comparison of the change in flapwise bending stiffness between FW configuration 1 and 2 shows that the decrease in flapwise bending stiffness for FW configuration 2 is much lower than that for FW configuration 1. This is because of the differences in the positioning of the piston accumulators in the cross-section and their distances to the cross-sectional center of gravity.

To quantify the impact of the changes in blade bending stiffness on blade bending behaviour, analyses of the static eigenfrequency of the blade and the change in the blade tip deflection at the rated power were conducted. The eigenfrequency analysis of the FW configurations 1 and 2 clearly shows that the impact of the FW in the discharged state on the blade behavior is negligible. This indicates that the presented methodologies enable the incorporation of a hydraulic-pneumatic FW in a WT's rotor without the requirement for a complete redesign of the blade.

Previous work of the author shows that a hydraulic–pneumatic FW in the rotor of a WT can serve the grid as well as the WT itself [6]. This conclusion was based on simulations with a simplified first-eigenmodes simulation model of a WT [8]. Future work will focus on a combination of the FW configurations resulting from the present study with FW applications from a previous study [6] and apply this combination in a state-of-the-art mechanical load simulation tool such as HAWC2 or OpenFAST. These load simulation tools will be modified to validate the rotor blade design with the hydraulic–pneumatic FW. As a logical consequence, future work in collaboration with WT manufactures will aim to validate the feasibility of the hydraulic–pneumatic FW in WT rotor blades.

References

[1] Jauch C 2015 A flywheel in a wind turbine rotor for inertia control *Wind Energy* **18** 1645-1656

[2] Jauch C, Hippel S 2016 Hydraulic–pneumatic flywheel system in a wind turbine rotor for inertia control *IET Renewable Power Generation* **10** 33-41

[3] Hippel S, Jauch C, Ritschel U 2019 Hydraulic-pneumatic flywheel configurations for controlling the inertia of a wind turbine rotor *Wind Engineering* **43** 114-132

[4] Hippel S, Jauch C 2019 Load analysis of hydraulic-pneumatic flywheel configurations integrated in a wind turbine rotor *Wind Energy* **22** 1190-1202

[5] Alhrshy L, Jauch C, Kloft P 2020 Development of a Flexible Lightweight Hydraulic-Pneumatic Flywheel System for Wind Turbine Rotors *Fluids* **5** 162

[6] Jauch C 2021 Grid Services and Stress Reduction with a Flywheel in the Rotor of a Wind Turbine *Energies* **14** 2556

[7] Resor B, Definition of a 5MW/61.5m wind turbine blade reference model, [Online] Available: http://www.osti.gov/servlets/purl/1095962/. [Accessed 2022 Jan 21].

[8] Jauch C, First Eigenmodes Simulation Model of a Wind Turbine - for Control Algorithm Design, [Online] Available: https://www.researchgate.net/publication/344154941_First_Eigenmodes_Simulation_Model_of_a_Wind_Turbine_-_for_Control_Algorithm_Design. [Accessed 2022 Jan 21]

energies

Article

Implementation of Variable Blade Inertia in OpenFAST to Integrate a Flywheel System in the Rotor of a Wind Turbine

Laurence Alhrshy

Special Issue

Grid Services with Wind Turbines and the Resulting Mechanical Loads

Edited by
Prof. Dr. Clemens Jauch

MDPI

Article

Implementation of Variable Blade Inertia in OpenFAST to Integrate a Flywheel System in the Rotor of a Wind Turbine

Laurence Alhrshy

Wind Energy Technology Institute, Flensburg University of Applied Sciences, Kanzleistraße 91-93, 24943 Flensburg, Germany; laurence.alhrshy@hs-flensburg.de; Tel.: +49-461-48161-407

Abstract: In this paper, the integration of the dynamic behavior of the flywheel system into the load simulation tool OpenFAST is presented. The flywheel system enables a wind turbine to vary the inertia of its rotor blades to control the power production and, most importantly, to affect the vibratory behavior of wind turbine components. Consequently, in order to simulate the behavior of a wind turbine with a flywheel system in its rotor, the variable blade characteristics need to be considered in the load simulation tool. Currently, computer-aided engineering tools for simulating the mechanical loads of wind turbines are not designed to simulate variable blade inertia. Hence, the goal of this paper is to explain how variable inertias of rotor blades are implanted in such load simulation tools as OpenFAST. OpenFAST is used because of it is free, publicly available, and well documentation. Moreover, OpenFAST is open source, which allows modifications in its source code. This add-on in the load simulation is applied to correct rotor mass imbalance. It can also be applied in many cases related to the change in the inertia of wind turbine rotor blades during its operation as, for example, atmospheric ice accretion on the blades, smart blades, etc.

Keywords: flywheel; flywheel torque; load simulation; mechanical loads; OpenFAST; rotor imbalance; wind turbine

1. Introduction

The general idea of the flywheel (FW) system is based on the inertia variation of wind turbine (WT) rotor blades. This is done by shifting a fluid mass between two-piston accumulators in the rotor blade of a WT. The physical description of such an energy storage system is presented in previous works of Jauch et al. and this covers the kinetic [1] and hydraulic [2] aspects.

The initial application of the FW system was developed to allow a certain variation of the electrical power of the WT, independent of the prevailing wind conditions [3]. Meanwhile, the impact of the FW system on the vibratory behavior of the WT and on the natural frequencies of the rotor blades has become one of the most important applications of this system, because of its influence on the operation life of the WT [4].

In order to analyze the impact of the FW system on the vibratory behavior of the WT components, the dynamic behavior of the FW system should be first implemented in the load simulation tool. Due to the fact that all state-of-the-art load simulation tools for WTs are unable to represent variable rotor blade inertias as they happen in the FW system, the dynamic behavior of the FW system cannot be represented without changing the source code of these load simulation tools. Therefore, all the previous mechanical load simulations, either for the conventional steel FW accumulators design [5] or for the flexible carbon fiber-reinforced plastics (CFRP) FW accumulators design [4], could only be done under two conditions: the FW statically fully charged and the FW statically fully discharged.

The previous load simulations were done for several FW configurations. These configurations were derived via a methodology, which was used to determine the positions and dimensions of the FW accumulators into the rotor blades [6]. However, since the goal of this paper is not to analyze the load impact of all the CFRP FW configurations published

in previous work by the author [4], the load analysis is limited in this paper to only one relevant FW configuration. This configuration is the same one used by the first eigenmodes simulation tool of a WT [7]. This tool is developed for control algorithm design at the Wind Energy Technology Institute (WETI) of Flensburg University of Applied Sciences, Germany. In the following, the considered FW configurations are named "types" and are identified with Roman numerals, as introduced in Hippel et al. [6]. Hence, the properties of the CFRP position accumulators of the FW type VI, mentioned in Table 1, are used to implement the variable blade inertia.

Table 1. Properties of the CFRP piston accumulators of FW type VI.

No. of Tip Accums	Rotor Radius m	Total Length of Tip Accums mm	Stationary Weight of Tip Accums kg	Total Length of Root Accum mm	Stationary Weight of Root Accum kg	Fluid Weigh kg
2	Each at 46.6	5047 and 4923	402.47	4437	276.86	925.46 [1]

[1] The fluid mass of 925.46 kg is shifted between the root and tip accumulators.

The stationary masses in Table 1 are added to the distributed mass densities of the rotor blade regarding the total length of the root and tip accumulators. For the Sandia 61.5 m rotor blade design (Sandia National Lab., Albuquerque, USA) [8] that is used in this paper, where the mechanical properties of the rotor blades are distributed over 17 elements, the stationary masses of the root and tip accumulators are added to the first two elements and to the 11th, 12th, and 13th elements, respectively. Whereas the stationary masses of the tip and root accumulators are considered as constant masses, the fluid mass is the mass that is varying along the root and tip elements. Varying the fluid mass is determined by so-called charge-index-factors (K). These factors can be steplessly varied between the limit values of 0 and 1 for the discharged and charged states, respectively. If K in one blade equals 0, the FW is fully discharged and the total fluid mass is added to the root elements of this blade and, if K equals 1, the FW is fully charged and the total fluid mass is added to the tip elements of the same blade.

Due to the public availability of the 5 megawatt (MW) reference WT, and the extensive use of its data in studies by the wind energy research community as a system that represents the current and future state-of-the-art offshore systems, the FW system was adapted to this WT. The Sandia 61.5 m rotor blade design is also applied in the original design of the 5 MW reference WT developed by the National Renewable Energy Laboratory (NREL), USA [9].

First of all, before discussing the code adjustment of a load simulation tool to implement the dynamic behavior of the FW system, it must be decided in which load simulation tool this adjustment should be performed. FLEX5 [10], FAST [11], and Bladed [12] are all recognized WT load simulation tools which are used by the WT industry. However, in this paper, OpenFAST is selected because of it is free, publicly available, and well documented. OpenFAST is a computer-aided engineering tool, which is developed by NREL for simulating the coupled dynamic response of WTs [13]. This software is also used by thousands of WT designers, manufactures, consultants, certifiers, researchers, students, and educators all over the world [11]. Moreover, OpenFAST has the advantages of a self-sustaining community-developed software by working with OpenFAST on a GitHub repository. This feature offers a good opportunity to communicate with the NREL OpenFAST team and other developers throughout the OpenFAST community [14]. All of these advantages make it obvious that OpenFAST is a suitable load simulation tool to implement the dynamic behavior of the FW system in WT. However, the high complexity of the structure of OpenFAST requires a good understanding of the architecture of this program before any modifications to its source code. Hence, the architecture of OpenFAST is briefly introduced in the next section. More details about the program are described in a previous project report of the author [15].

This paper begins with the introduction about the program structure, which helps to understand where and how the variable blade inertias are implemented in the source code

of OpenFAST. Subsequently, the computation and integration of the resulting loads from the change in rotor blade inertia are discussed in two following sections. Consequently, the modified code is tested using a simple simulation scenario of a WT without aerodynamic loads and controllers. This test aims to verify the implementation correctness of the modified code and to illustrate the impact of the variable blade inertia on the WT rotor speed behavior. Finally, the applicability of the FW system to correct a rotor mass imbalance is tested during the WT operation with enabled aerodynamic and controller modules.

2. Architecture of OpenFAST

OpenFAST is a multi-physics, multi-fidelity tool for simulating the coupled dynamic response of wind turbines. The theory of OpenFAST is based on the coupled interactions of several computational modules which are responsible for structural dynamics, aerodynamics, control and electrical system dynamics, and hydrodynamics for offshore structures to enable coupled nonlinear aero-hydro-servo-elastic simulation in the time domain [16].

Basically, the architecture of OpenFAST consists of a driver program (glue code), which couples several individual submodules together, see Figure 1. These submodules (AeroDyn, SevoDyn, ElastoDyn, BeamDyn, etc.) correspond to different physical domains of the coupled aero-hydro-servo-elastic solution [16].
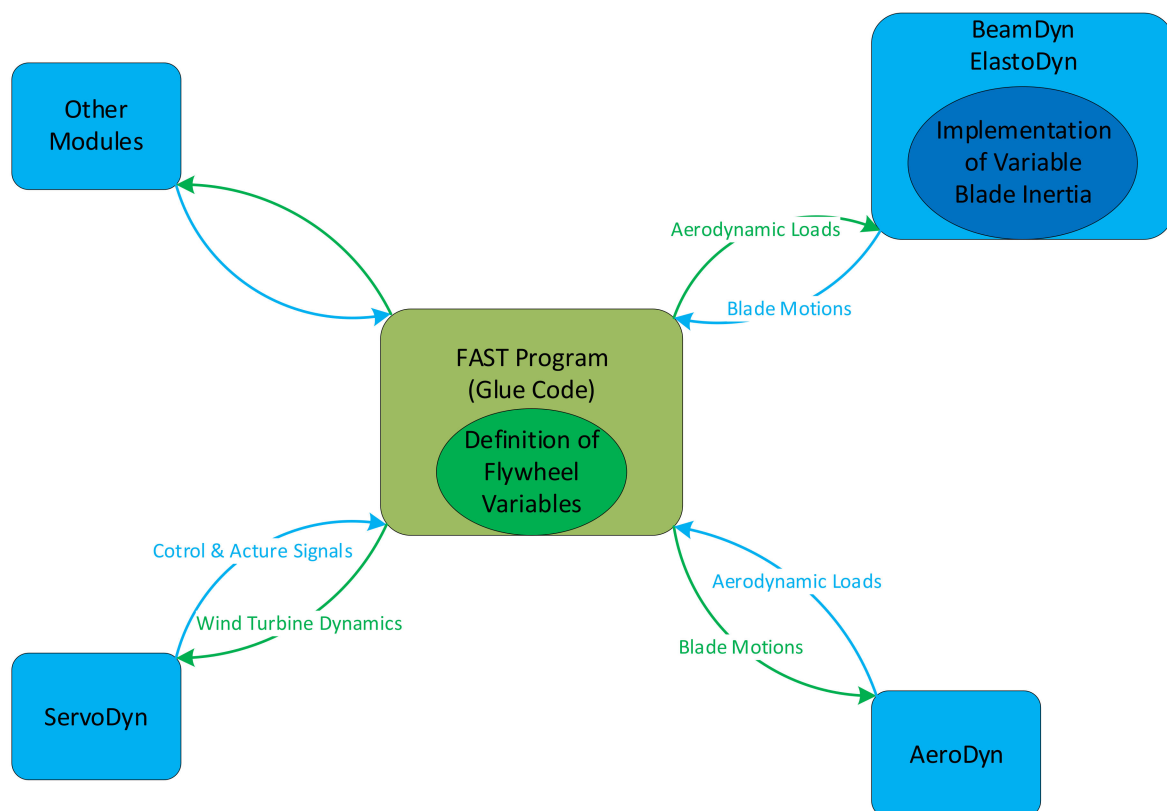
Figure 1. Coupled interaction between FAST and submodules.

ElastoDyn and BeamDyn in Figure 1 are those submodules that are responsible for the blade structural dynamics. The major difference between these two modules lies in the implementation of beam theory. The model underlining BeamDyn is based on the geometrically exact representation of the beam theory (GEBT), whereas ElastoDyn uses Bernoulli-Euler beam theory under bending [16].

ElastoDyn uses Kane's method [17] to set up equations of motion, which can be put into Newton's Second Law (see Equation (1)).

$$F = m \cdot a \tag{1}$$

This method simplifies the equation of motion, which makes the equations easier to solve than the method of GEBT.

The GEBT used by BeamDyn makes no approximation on the geometries in formulating the equation of motions (see Equation (2))

$$\dot{\underline{h}} - \underline{F}' = \underline{f}$$
$$\dot{\underline{g}} + \tilde{\underline{u}}\underline{h} - \underline{M}' + (\tilde{x}_0' + \tilde{u}')^T \underline{F} = \underline{m} \tag{2}$$

where $\underline{m}$ and $\underline{f}$ are the distributed moment and force applied to the beam structure, respectively; $\underline{g}$ and $\underline{h}$ are the angular and linear moment resolved in the inertial coordinate system, respectively; $\underline{M}$ and $\underline{F}$ are the beam's sectional moment and force, respectively; $\underline{u}$ and x_0 are the one-dimensional displacement and the position vector of a point along the beam's reference line, respectively; the notation $(\bullet)'$ and $(\dot{\bullet})$ indicates a derivative with respect to beam axis x_1 and to time, respectively; the tilde operator $(\tilde{\bullet})$ defines a skew-symmetric tensor corresponding to the given vector [16].

Since the goal of this paper is not to support a full geometric nonlinearity solution or to simulate a large deflection of an anisotropic composite material of a rotor blade with a pre-bended reference axis, it is obvious to choose ElastoDyn to implement the dynamic behavior of the FW system in OpenFAST. Although ElastoDyn uses a simpler mathematical theory than BeamDyn, the exact solutions of ElastoDyn meet the needs in this paper. A detailed comparison between ElastoDyn and BeamDyn is introduced in a previous project report of the author's [15]. Figure 1 shows that the implementation of variable blade inertia takes place within the module of ElastoDyn, whereas the additional variables of the FW system are defined into the glue code of OpenFAST. This enables the FW variables to be passed through the local and external modules of OpenFAST, as discussed later in the next sections.

The executable files, as well as the configuration libraries of the program, are available online on the homepage of OpenFAST [18]. Since variable rotor blade inertias are not considered in the original source code of OpenFAST, the currently available executable cannot be used for the proposed tasks in this paper. Hence compiling from the source code must be done in order to obtain an executable, which includes the add-on of variable blade inertias in its code.

Different methods to obtain the OpenFAST executable from the source code are presented on the homepage of OpenFAST [18]. One of these methods uses Visual Studio (VS) to build OpenFAST on Windows. Building OpenFAST on Windows with VS gives Windows users better options for developing and debugging the source code because of its streamlined manner in solving and maintaining programing errors.

3. Implementation of Variable Blade Elements Masses

Since the main idea of the FW system is based on the variation of rotor blade inertias during the WT operation, this variation is translated in the source code of ElastoDyn by varying the blade element mass within a given simulation. The masses of the blade elements are stored in ElastoDyn blade input files as a part of the blade's mechanical properties. The main challenge facing the implementation of variable blade elements' masses is that the blade's mechanical properties are used as time-invariant input parameters, which are called only once at the module initialization and then they are erased directly after that. Moreover, the data type definition of the blade elements' masses in the programming language of OpenFAST does not allow any change in its value during the whole simulation time. These difficulties and their iterative solutions are discussed in detail in [15]. Nevertheless, the iterative solution is briefly depicted in Figure 2.
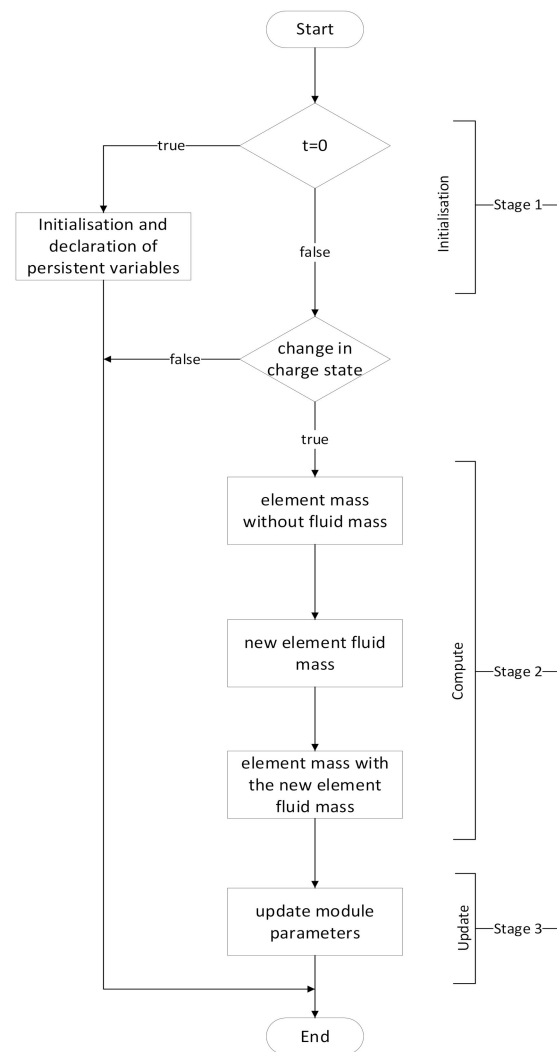
Figure 2. Iterative process for initializing, computing, and updating the change in a blade element mass, and their related parameters.

The flow-chart diagram in Figure 2 divides the iterative solution of the above-mentioned problems in three stages:

- Stage 1: As soon as the simulation starts in OpenFAST at simulation time zero, the variables that declare the initial conditions of the FW system are defined. The detention of these variables is based on the blade input parameters of ElastoDyn, before they are erased after the initialization. This procedure allows access to these variables at any time during the simulation.

- Stage 2: This stage is responsible for the change in the masses of the blade elements regarding the charge-index-factor (K). At first, the masses of the blade elements are calculated without the additional fluid mass. Consequently, the new fluid mass of each blade element is calculated depending on the current value of K. Finally, the newly calculated fluid mass is added to the corresponded blade element mass. The entrance in this stage is conditional on the change in K, i.e., the $K\_t\text{-}1$ from the previous simulation step must not be equal to the K_t from the current simulation step in order to enter this stage. Such a condition helps to speed up the simulation when no change in the charge state of the FW in any blade is happening.

- Stage 3: After changing the masses of the blade elements in stage 2 all the parameters that are related to the blade elements' masses must be updated, in order to follow the new values of the changed masses of the blade elements.

These stages are translated in the programming language of OpenFAST as additional subroutines, which are called in the main dynamic calculation of ElastoDyn.

4. Integration of Flywheel System in OpenFAST Simulink Interface

As Simulink is a popular simulation tool for the design and development of control algorithms, OpenFAST has also been implemented as a library that can be called from a Simulink S-Function block, using predefined inputs from Simulink. Therefore, modules such as Generator torque control, nacelle yaw control, pitch control, high-speed shaft brake, and other external modules can be designed in the Simulink environment and, meanwhile, they can use the complete nonlinear aeroelastic wind turbine equations of motion available in OpenFAST [19].

The wind turbine sample model, as shown in Figure 3, contains the S-Function block with the OpenFAST equations of motion. It also contains the control signals that are implanted in the above-mentioned control models. These models are deactivated in the Flywheel_System.mdl model in Figure 4, as the focus is only on the implementation of the FW system. Figure 4 shows the FW system block, which includes the equations of the additional loads and the charge-index-factors for each rotor blade. The next section will discuss in detail which loads are generated by the FW system and not considered in the OpenFAST equations of motion. The function block *f(u)* shown in Figure 4 is used to select certain data from OpenFAST outputs, which are required for the equations in the FW system model.
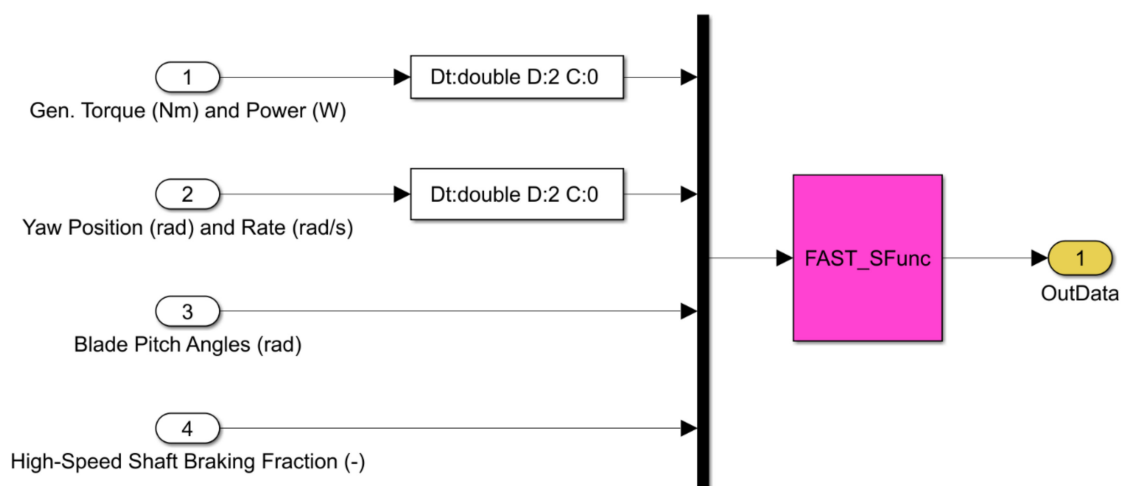

Figure 3. OpenFAST wind turbine sample model in Simulink.

However, since the OpenFAST Simulink interface is currently set up to receive only the control signals as inputs, as shown in Figure 3, both the OpenFAST glue code and Simulink Interface must be modified. This modification is needed, in order to pass the outputs of the FW system model through the Simulink interface, and then to use them in OpenFAST glue code. Moreover, it must be noted that the largest array of inputs that can be accepted from Simulink interface and passed to OpenFAST glue code must not be more than 11 elements, otherwise, a segmentation fault is transmitted. Both of these issues are discussed in detail on OpenFAST GitHub [20]. Moreover, all source code modifications of OpenFAST that are performed in this paper are available on ResearchGate [21]. However, compiling from the source code is needed in order to obtain an OpenFAST executable with the add-on of variable blade inertia. For compiling from the source code, the NREL OpenFAST team has developed an approach that uses CMake to generate build files for all platforms [18].
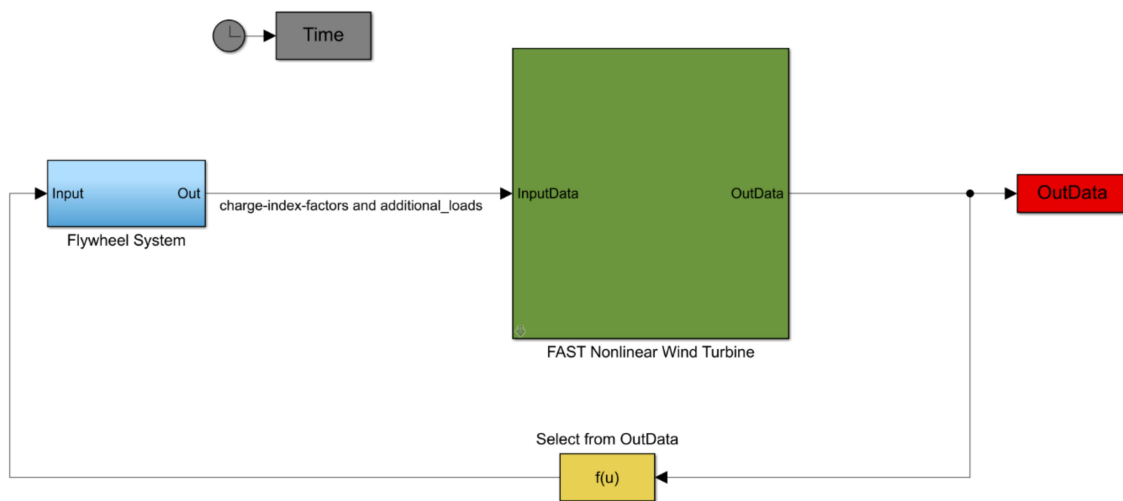
Figure 4. Flywheel_System.mdl model in OpenFAST Simulink interface.

5. Impact of the Variable Blade Elements' Masses on Wind Turbine Loads

In general, the theory basics of ElastoDyn blade structural dynamics does account for the blade loads in two main categories: generalized inertia forces, F_r; and generalized active forces, F_r^*; including the external forces acting on the body, such as blade aerodynamic forces, blade and tower elastic bending forces, gravity, and drive train forces. These are described in Equations (3) and (4) [16].

$$F_r + F_r^* = 0 \tag{3}$$

$$F_r^*|_{Total} = F_r^*|_{Tower} + F_r^*|_{Nacelle} + F_r^*|_{Hub} + F_r^*|_{Blades} \tag{4}$$

Consequently, the resulting velocities and accelerations due to the blade and tower deflections are expressed as partials in the main kinematics and kinetics routines in ElastoDyn. Hence, every force that is based on the acceleration of the blade body is intrinsic to the kinematics and kinetics. This means that the additional loads resulting from the FW system due to the stationary change of the blade elements' masses are intrinsically included in the kinematics and kinetics of ElastoDyn. However, the load that is resulting from the portable mass between two blade elements in a certain time is not considered in the structural dynamics of ElastoDyn. This is because variations in the inertia of the rotor do not happen in state-of-the-art WTs.

This load is already explained in the previous work of Jauch [1] as an additional torque, which is resulting from the change in angular momentum. The law of the conservation of the angular momentum presented in Equations (5)–(7) describes the fact that a torque, T, results if the angular momentum, L, changes, in order to keep the kinetic energy, E_{kin}, constant.

$$E_{kin} = \frac{1}{2} \cdot J \cdot \omega^2 \tag{5}$$

$$L = J \cdot \omega \tag{6}$$

$$T = \frac{dL}{dt} \tag{7}$$

where J is the mass moment of inertia, and ω is the rotational speed.

Equation (8) expresses the FW torque, T_{FW_bl}, in one blade in terms of change in the FW inertia in a rotor blade, $\frac{d}{dt}(J_{FW\_bl})$.

$$T_{FW\_bl} = -\frac{d}{dt}(J_{FW\_bl}) \cdot \omega_{rot} \tag{8}$$

The inertia of the FW in one blade, J_{FW_bl}, changes if the centre of gravity, R_{var}, of the FW fluid, m_{fluid}, changes.

$$J_{FW\_bl} = R_{var}^2 \cdot m_{fluid} \tag{9}$$

The value of the rotational speed, ω_{rot}, in Equation (8) is derived from the outputs of OpenFAST using the select function *f(u)*, as shown in Figure 4. However, before any outputs are generated in OpenFAST, the FW torque must be implanted correctly in the dynamic calculation of OpenFAST. It must be ensured that the added load does not double count terms that are already added by the change in the masses of the blade elements in the source code of ElastoDyn. This can be accomplished by implementing the FW torque as an external additional torque at the hub since ElastoDyn has a model-level input point mesh for external loads applied at the hub. The FW torque is already calculated in the FW system model in Simulink (see Figure 4) by using Equations (8) and (9), therefore, the value of this additional torque can be used to set the value of the external loads at the hub. Normally, this load is set to zero, in case no external loads have been applied at the hub.

In order to verify the implementation correctness of the FW system in the structural dynamics of the load simulation tool, load simulations are performed for a WT with a deactivated control system and without the impact of the aerodynamic loads. This allows clarification of the impact of variable blade inertia on the behavior of the WT rotor speed independent of any influences from aerodynamic loads and controllers. Therefore, in the following simulation scenario, the aerodynamic, as well as the control modules of OpenFAST are disabled. However, in the next section, these modules are enabled again to cover the impact of the FW system on the behavior of the WT during its power production.

As mentioned in the introduction, blade spans, those that are close to the location of the blade root and tip accumulators of the FW type VI, are selected according to the Sandia 61.5 m rotor blade design. Therefore, blade elements 1 and 2 as well as blade elements 11, 12, and 13 are selected to represent the positions of the root and tip accumulators of the FW type VI, respectively. Figure 5 shows the span locations and the mass of these elements. The definition of the mechanical properties of the blade elements in the source code of ElastoDyn is based on the distributed sectional properties of the Sandia 61.5 m blade design. This design follows the characteristics of the NREL 5 MW reference turbine blade. The NREL 5 MW reference WT has three blades. The structural properties of each blade are distributed in sectional properties along the blade pitch-axis [9]. The distributed blade section mass is based on the geometry and the material selection for each blade section. Regarding the Sandia 61.5 m blade design, the dimensions of the blade root sections are much bigger than the geometry of the blade body and the blade tip sections. Therefore, most of the blade mass is concentrate near to the blade root. This difference in the mass distribution along the rotor blade can also be seen in the difference between the mass of the blade elements in Figure 5, where blade element 1 at a span location of 3.6 m is much heavier than blade element 13 at a span location of 47 m. Figure 5 also shows a fluid mass of 925.46 kg, which is corresponding to the total fluid mass of the FW type VI (see Table 1), which is shifted between the root and tip accumulator. The charge-index-factors determine when and where how much fluid mass must be shifted and which is baled. For the simulation scenario in Figure 5, the FW is charged and discharged simultaneously in the rotor, therefore, the charge-index-factors of the three blades are identical. Unsynchronized charging/discharging is discussed in the next section.
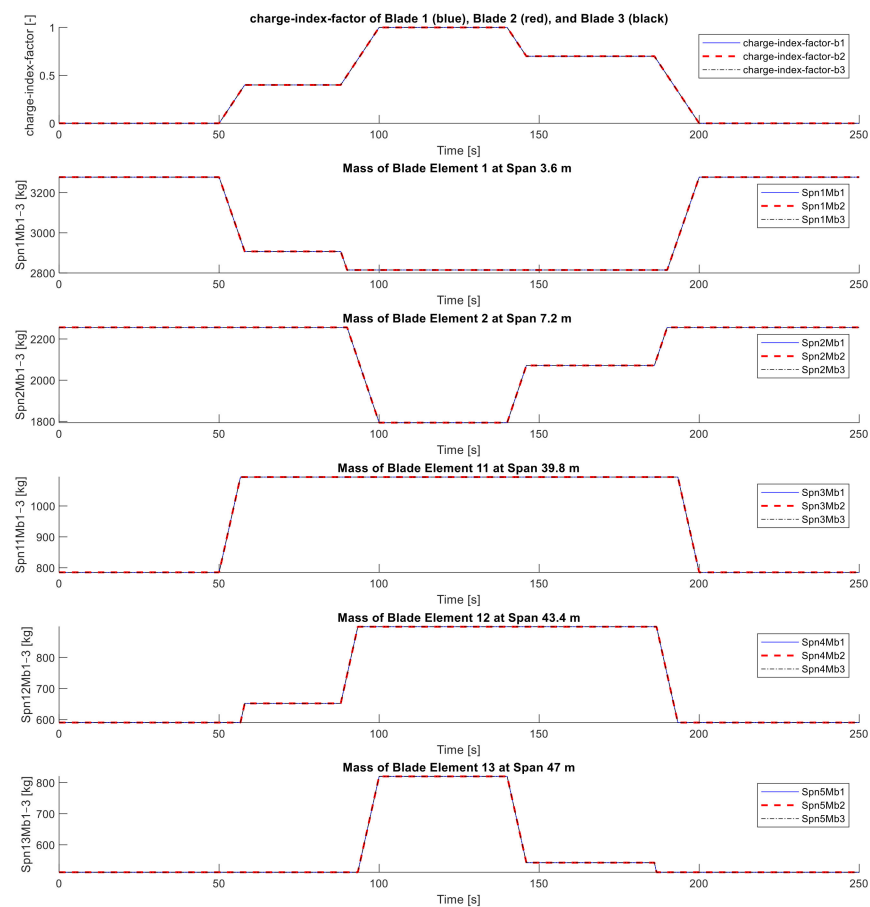
Figure 5. Mass change of blade element 1, 2, 11, 12 and 13 depending on the charge-index-factor of each rotor blade.

The FW starts to charge at 50 s and it is fully charged at 100 s, whereas discharging starts at 140 s and ends at 200 s. Meanwhile, the charge/discharge process is interrupted twice: at 58 s as the FW is 40% charged, and at 146 s as the FW is 30% discharged, see subplot 1 in Figure 5. As a response to the changes in the charge-index-factors subplots, 2–6 in Figure 5 show the change in the masses of the above-selected blade elements.

The resulting total FW torque from the three blades, T_{FW_bl}, and its relation to the change in the FW inertia, $\mathrm{d}/\mathrm{d}t(J\_FW\_bl)$ are illustrated in Figure 6. Figure 6 also shows the change in the value of the variable center of gravity, *R_var*, of the FW type VI in relation to the values of the charge-index-factors in Figure 5.

The impact of variable blade inertia on the rotor speed of the WT due to the application of the FW system is illustrated in Figure 7. Where it is obvious that the increase of the blade inertia by charging the FW system leads to slowing down the rotor speed on the one hand and, on the other hand, the decrease of the blade inertia by discharging the FW system leads to speed up the rotor speed. As mentioned above, since the control system and the aerodynamic loads of the WT are deactivated, the decrease of the rotor speed is not recovered by the aerodynamics or by pitching the rotor blades. This can be obviously seen in Figure 7 as the pitch angle is still unchanged during the whole simulation time, even when the rotor speed changes due to the change in the blade inertia.
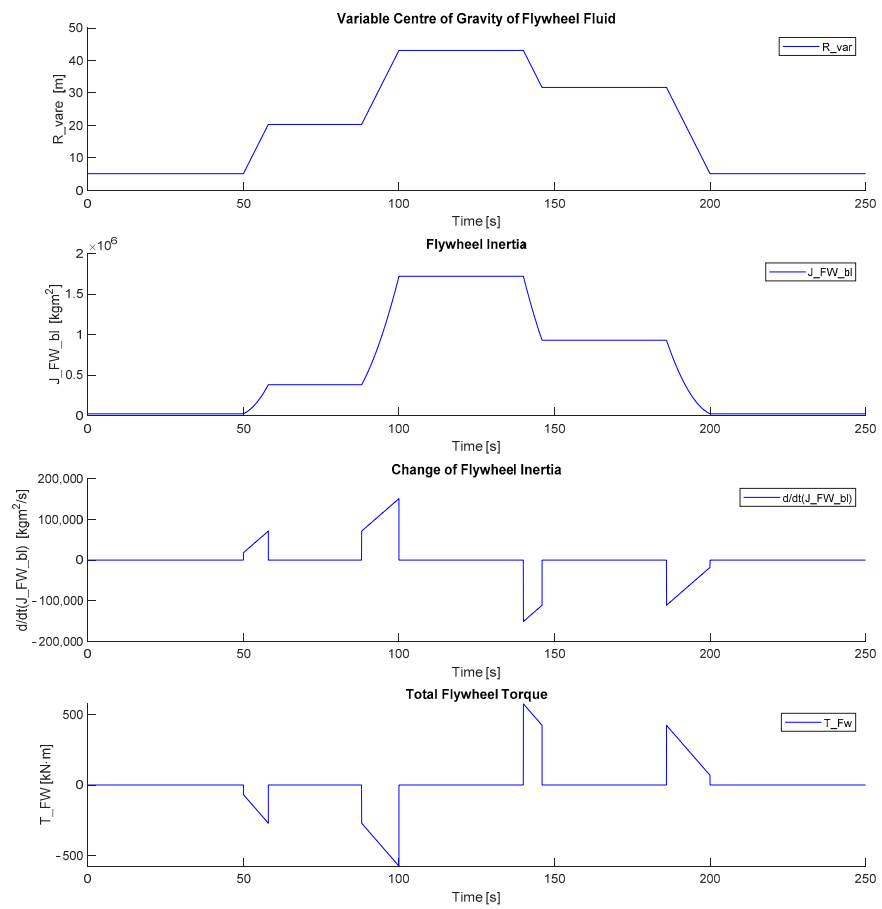
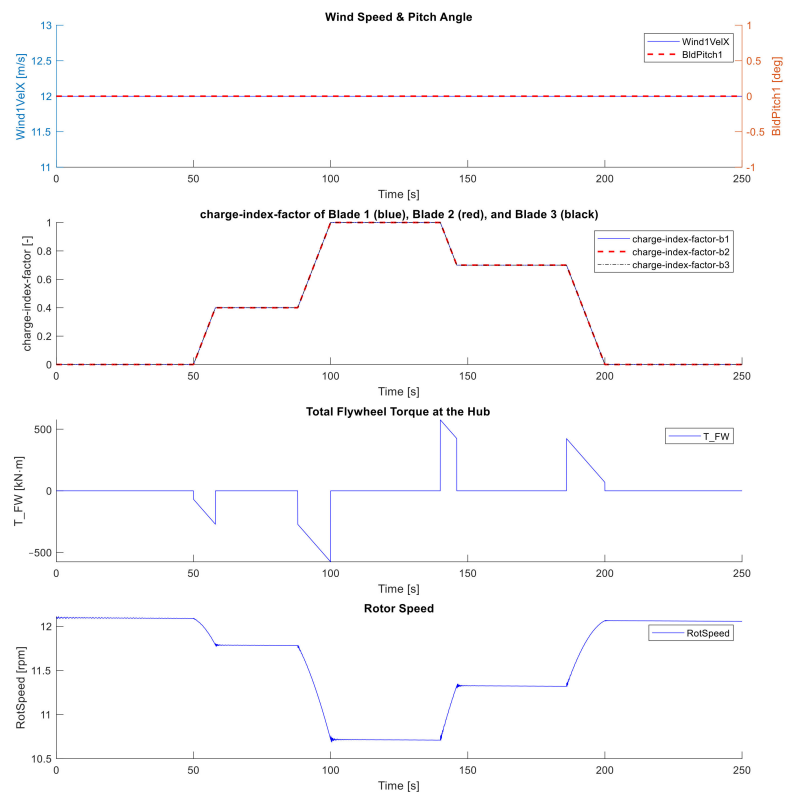**Figure 6.** Resulting FW torque of FW type VI.

Figure 7. The effect of the FW torque on the rotor speed due to the change in blade elements' masses.

As the response of the rotor speed to the change in the rotor blade inertia shown in Figure 7 meets the physical basics of the law of the conservation of the angular momentum [22], this verifies that the implementation of the FW system in the structural dynamics of OpenFAST is correct. Hence, the modified code can be applied on a WT model during its power production.

6. Analysis of Rotor Imbalance of Wind Turbine with Flywheel System

A rotating system is imbalanced when its center of mass is out of alignment with the center of rotation [23]. In WT, rotor imbalance may be the result of aerodynamic imbalances which could be caused by pitch misalignment of one blade with respect to the other blades, or it may be the result of mass imbalance due to a number of causes, for example, ice accretion, blade damage, poor blade manufacturing tolerances, etc. [24]. Vibrations resulting from rotor imbalances significantly affect WT fatigue, which may reduce the efficiency and the operation life of a WT.

Therefore, there is a need to correct rotor imbalances depending on their causes as soon as possible. Different literature sources contain detailed descriptions on the determination and correction of aerodynamic [25] as well as mass imbalances [24,26]. The rotor imbalance correction methods are generally based on the adjustment of the pitch angle of WT rotor blades, which leads to a reduction in the power output of the WT. Since the FW system has the ability to operate variable blade inertias, this advantage can be applied to correct rotor mass imbalances without the need to adjust the pitch angle. This ability is illustrated in the next simulation scenario.

At first, if the applicability of the FW system to correct mass imbalances to be simulated, the rotor imbalance needs to be represented in a simulated WT model. Therefore, the 5 MW reference WT model presented in the following simulation scenario contains one rotor blade with an additional mass at a certain span location. Since The Sandia 61.5 m blade design is used to implement the FW type VI, this design is also used to represent the rotor imbalance.

Figure 8 shows the rotor imbalance in terms of additional mass of circa 191 kg in blade 1 element 11 at a span location of 39.8 m (see subplot 4 in Figure 8 Spn3Mb1 in blue). The additional mass weight and location are set to those values in order to generate a mass imbalance for this simulation scenario, and they can be varied for other simulation scenarios. This mass difference in blade 1 from the other two blade masses leads to rotor imbalance. In the following simulation scenario, the WT model starts with fully charged FW tip accumulators and with a rotor imbalance simulation time of 150 s. From that time, the FW system is set to discharge not simultaneously in all blades until the three blades have the same inertia. This is done by stopping the FW to discharge in blades 2 and 3 at a simulation time of 163 s, whereas the discharging process is continuing in blade 1 until the mass of blade element 11 in all blades is equal, which is achieved at a simulation time of 167 s. At this point, the total additional mass of blade 1 is shifted from the blade body at a span of 39.8 m to the blade root at a span of 3.6 m. This is how the rotor imbalance is corrected using the FW system, which allows the minimization of the lever arm of the additional mass in one or more blades, and thus, reduces the impact of the mass imbalance on WT behavior. However, since the rotor blades are balanced, the tip FW accumulators in blades 2 and 3 are not allowed to be fully discharged, in order to keep the balance in blade element 11 of all blades.

For the above simulation scenario of rotor imbalance, the WT runs under rated steady wind conditions with a constant horizontal wind speed of 12 m/s. The FW system is initially fully charged in the rotor and is discharged not simultaneously in the three blades, see Figure 9. Such initial rotor imbalance is a 1p excitation, which excites the tower to a later vibration. Figure 9 shows this vibration in terms of side-to-side deflection of the tower top, where the vibration amplitudes of the tower top side-to-side deflections are obviously much greater within the period of the rotor imbalance than the period after the imbalance correction at a simulation time of 167 s. The reason for this is essentially that

there is a grater tower-top yaw bearing roll moment before rather than after the correction of rotor imbalance.
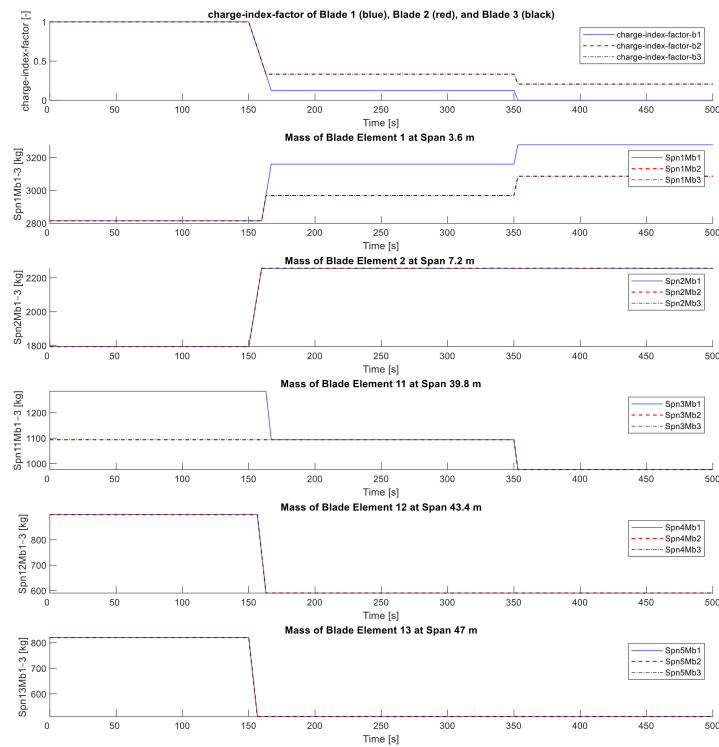

Figure 8. Rotor imbalance due to the additional mass in blade 1, element 11, and elimination of the imbalance by partly charging the flywheel system.
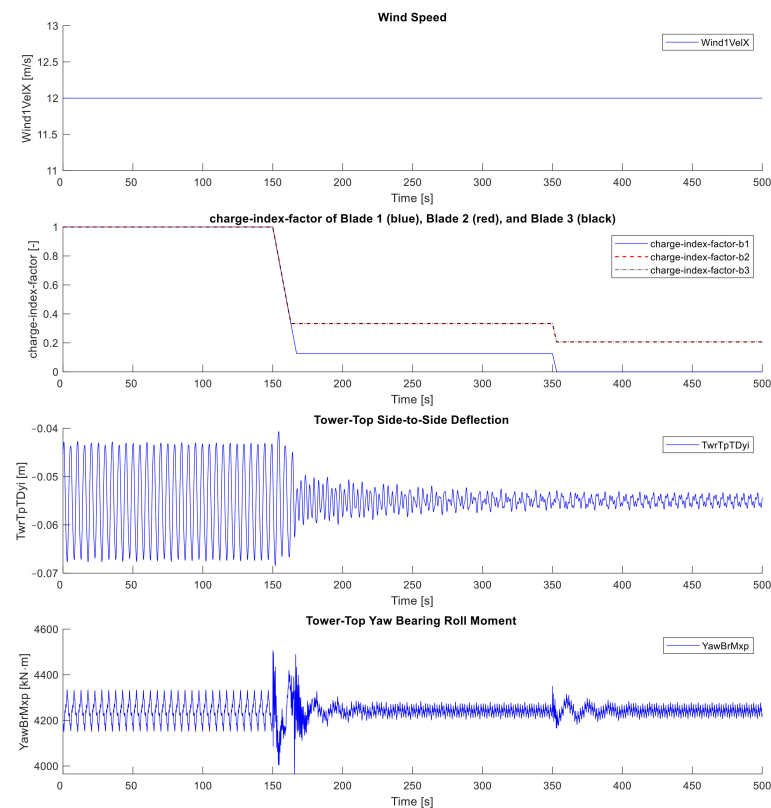

Figure 9. Impact of the flywheel system on a tower-top side-to-side deflection by imbalance in the rotor blade.

In Section 5 it is shown how the WT behaves with the FW system when its aerodynamic loads and control system are disabled. By contrast with Figure 7, Figure 10 shows the impact of the FW system on the WT behavior with enabled aerodynamics and controller modules. Moreover, the presented WT in this section gets excited with a 1p excitation, due to the previously mentioned rotor imbalance. This excitation obviously affects the behavior of rotor speed, pitch angle, and generator power in the first 150 s, where continuous oscillations in the signals are seen in this period. After that, the rotor imbalance correction procedure starts by discharging the FW system asymmetrically in the three blades. The FW torque, T_{FW}, generated by discharging the FW speeds up the rotor over the rated value of rotor speed, and thus, the power production increases over the rated value of 5 MW. Consequently, the pitch controller raises the pitch angle in order to slow down the rotor to the rated rotor speed again. The original pitch controller of the NREL 5 MW reference WT is designed to maintain the balance between power generation and rotor speed at rated conditions. Therefore, such changes in the rotor speed due to the change in blade inertia are immediately maintained by the pitch controller, and thus, the released kinetic energy by discharging the FW system is wasted through the pitch control.
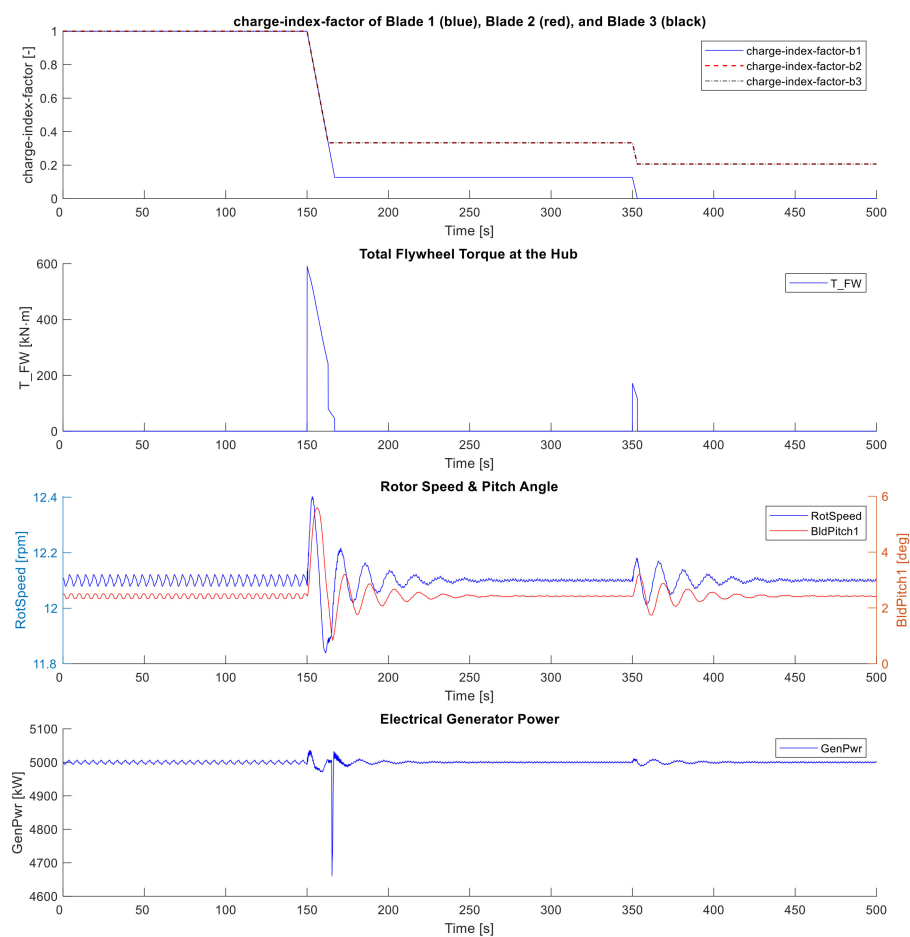
Figure 10. Impact of the flywheel torque on rotor speed and generator power.

Hence, in future, a controller has to be designed that uses the stored kinetic energy, for example, to support grid frequency. The developed controller should also consider the power consumption of the FW system since its tip accumulators are charged with electric pumps, which are supplied from the power production of the WT.

7. Conclusions

In the present paper, variable blade inertia was implemented in the source code of the load simulation tool OpenFAST, in order to integrate an FW system in WT rotor blades. The

FW configurations used to represent the change in blade inertia are those corresponding to the FW type VI. The stationary masses of the root and tip accumulators are added at the respective location of the FW type VI within the blade mechanical properties of the Sandia 61.5 m rotor blade design, whereas the fluid mass of the FW type VI is implanted in the source code of the blade's structural dynamic module of OpenFAST to be shifted in- and outboard.

ElastoDyn and BeamDyn are those two modules that are represented by OpenFAST to implement the structural dynamics of rotor blades. Since the goals of this paper are not to support a full geometric nonlinearity solution, or to simulate a large deflection of a rotor blade, which is supported by BeamDyn, ElastoDyn is used for implanting the variable blade inertia. Moreover, the exact solutions of ElastoDyn fulfill the requirements of the simulated WT scenarios.

However, such implementation needs a good understanding of the source code of the load simulation program. Therefore, an algorithm is prepared to illustrate the major modifications of the source code. The code that the algorithm is based on is described in detail in a previous research project of the author [15], and it is available on ResearchGate [21].

Since OpenFAST is also implemented as a dynamic library that can be called from MATLAB/Simulink, this feature is used to implement the mathematical operations of the FW system as a Simulink model. However, passing outputs from the FW model through the Simulink interface of OpenFAST needs to modify both OpenFAST glue code and Simulink Interface.

The outputs of the FW Simulink models includes inter alia, the FW torque, T_{FW}, This torque represents the additional rotor torque that results from the change in angular momentum. Although this additional load is not considered in the structural dynamics of ElastoDyn, ElastoDyn offers a model-level input point mesh for external loads to be applied at the hub. This model is used to apply the FW toque to the hub.

As the source code, modifications are done. It is, therefore, necessary to verify the implementation correctness of the FW system in the structural dynamics of OpenFAST. This verification is done by simulating a WT with the integrated FW system and without the interaction of the aerodynamic loads and controllers. This simulation scenario aims to illustrate that the implemented variable blade inertia can lead to speeding up the rotor when the FW discharges, and to slowing down the rotor when the FW charges, as provided by the law of the conservation of the angular momentum.

Finally, as one of the several FW system advantages, the change of the blade inertia is applied to correct a rotor mass imbalance. The simulated mass imbalance is produced by adding an additional mass to one blade at a certain span location. The impact of the 1p excitation of rotor imbalance on the vibratory behavior of the WT is shown before and after the imbalance correction by using the FW system.

The impact of the FW system on the WT during its power production is also illustrated, where it was clear that future works should focus on developing control designs which manage the energies that are released and consumed by the FW system. Moreover, it is advantageous to validate the implementation of variable blade inertia in BeamDyn or in different load simulation tools, which will be the focus of future works.

Institutional Review Board Statement: Not applicable.

Informed Consent Statement: Not applicable.

Data Availability Statement: All source code modifications of OpenFAST (FAST_ Library.f90, FAST_Registry.txt, ElastoDyn.f90, ElastoDyn Registry.f90, FAST_Solver.f90) that are performed in this paper are available on ResearchGate "https://www.researchgate.net/profile/Laurence-Alhrshy-2".

Conflicts of Interest: The author declare no conflict of interest.

References

1. Jauch, C. A Flywheel in a Wind Turbine Rotor for Inertia Control. *Wind Energy* **2015**, *18*, 1645–1656. [CrossRef]
2. Jauch, C.; Hippel, S. Hydraulic–Pneumatic Flywheel System in a Wind Turbine Rotor for Inertia Control. *IET Renew. Power Gener.* **2016**, *10*, 33–41. [CrossRef]
3. Jauch, C. Controls of a Flywheel in a Wind Turbine Rotor. *Wind Eng.* **2016**, *40*, 173–185. [CrossRef]
4. Alhrshy, L.; Jauch, C.; Kloft, P. Development of a Flexible Lightweight Hydraulic-Pneumatic Flywheel System for Wind Turbine Rotors. *Fluids* **2020**, *5*, 162. [CrossRef]
5. Hippel, S.; Jauch, C. Load Analysis of Hydraulic-Pneumatic Flywheel Configurations Integrated in a Wind Turbine Rotor. *Wind Energy* **2019**, *22*, 1190–1202. [CrossRef]
6. Hippel, S.; Jauch, C.; Ritschel, U. Hydraulic-Pneumatic Flywheel Configurations for Controlling the Inertia of a Wind Turbine Rotor. *Wind Eng.* **2019**, *43*, 114–132. [CrossRef]
7. Jauch, C. First Eigenmodes Simulation Model of a Wind Turbine—For Control Algorithm Design. 2020. [CrossRef]
8. Resor, B. *Definition of a 5MW/61.5m Wind Turbine Blade Reference Model*; Technical Report No. SAND2013–2569; Sandia National Lab.: Albuquerque, NM, USA, 2013; p. 947422.
9. Jonkman, J.; Butterfield, S.; Musial, W.; Scott, G. *Definition of a 5-MW Reference Wind Turbine for Offshore System Development*; Technical Report No. NREL/TP-500-38060; National Renewable Energy Laboratory: Golden, CO, USA, 2009; p. 947422.
10. Jørgensen, M.F. *Aerodynamic and Mechanical System Modelling*; Department of Mechanical Engineering, Technical University of Denmark: Lyngby, Denmark, 2013; ISBN 978-87-7475-370-4.
11. FAST. Available online: https://www.nrel.gov/wind/nwtc/fast.html (accessed on 13 January 2021).
12. Wind Turbine Design Software | Bladed. Available online: https://www.dnvgl.com/services/wind-turbine-design-software-bladed-3775 (accessed on 13 January 2021).
13. FAST v8 and the Transition to OpenFAST—OpenFAST v2.3.0 Documentation. Available online: https://openfast.readthedocs.io/en/master/source/user/fast_to_openfast.html (accessed on 13 January 2021).
14. OpenFAST/Openfast. Available online: https://github.com/OpenFAST/openfast (accessed on 13 January 2021).
15. Alhrshy, L.; Jauch, C.; Bünning, N.; Schaffarczyk, A. Development of a Lightweight Hydraulic-Pneumatic Flywheel System for Wind Turbine Rotors. 2021. [CrossRef]
16. National Renewable Energy Laboratory. OpenFAST Documentation. Available online: https://openfast.readthedocs.io/_/downloads/en/main/pdf/ (accessed on 12 May 2021).
17. Kane, T.R.; Levinson, D.A. Dynamics: Theory and Applications. Available online: File:///C:/Users/Alhrshy/AppData/Local/Temp/Dynamics-Theory_opt-1.pdf (accessed on 25 March 2021).
18. Installing OpenFAST—OpenFAST v2.3.0 Documentation. Available online: https://openfast.readthedocs.io/en/master/source/install/index.html#compile-from-source (accessed on 14 January 2021).
19. Jonkman, J.M.; Buhl, M.L., Jr. *FAST User's Guide—Updated August 2005*; Technical Report No. NREL/TP-500-38230; National Renewable Energy Laboratory: Golden, CO, USA, 2005; p. 15020796.
20. Issue When I Run Simulink Model Which Depends on Openfast S-Function Mex Issue #548 OpenFAST/Openfast. Available online: https://github.com/OpenFAST/openfast/issues/548 (accessed on 12 October 2020).
21. Alhrshy, L. OpenFAST Modified Codes. 2021. [CrossRef]
22. Conservation of Angular Momentum Review (Article). Available online: https://www.khanacademy.org/science/high-school-physics/torque-and-angular-momentum/conservation-of-angular-momentum/a/conservation-of-angular-momentum-ap-physics-1 (accessed on 23 February 2021).
23. Kelm, R.; Kelm, W. Rotor Balancing Tutorial. Available online: https://rotorlab.tamu.edu/me459/Rotor%20Balancing/2016%20TPS%20Tut%20ROTOR%20BALANCING%20Pavelek.pdf (accessed on 12 May 2021).
24. Cacciola, S.; Agud, I.M.; Bottasso, C.L. Detection of Rotor Imbalance, Including Root Cause, Severity and Location. *J. Phys. Conf. Ser.* **2016**, *753*, 072003. [CrossRef]
25. Bertelè, M.; Bottasso, C.L.; Cacciola, S. Automatic Detection and Correction of Pitch Misalignment in Wind Turbine Rotors. *Wind Energy Sci.* **2018**, *3*, 791–803. [CrossRef]
26. Jeffrey, M.; Melsheimer, M.; Liersch, J. Method and System for Determining an Imbalance of a Wind Turbine Rotor. Available online: https://patents.google.com/patent/US8261599B2/en (accessed on 30 January 2021).

energies

Article

Variable Blade Inertia in State-of-the-Art Wind Turbine Structural-Dynamics Models

Laurence Alhrshy, Alexander Lippke and Clemens Jauch

MDPI

Article

Variable Blade Inertia in State-of-the-Art Wind Turbine Structural-Dynamics Models

Laurence Alhrshy [1],[*] , Alexander Lippke [2] and Clemens Jauch [1]

1   Wind Energy Technology Institute, Flensburg University of Applied Sciences, Kanzleistraße 91-93, 24943 Flensburg, Germany; clemens.jauch@hs-flensburg.de
2   AEROVIDE GmbH, Provianthausstr. 9, 24768 Rendsburg, Germany; info@aerovide.com
*   Correspondence: laurence.alhrshy@hs-flensburg.de; Tel.: +49-461-48161-407

Abstract: This paper presents a comparison of two methods to represent variable blade inertia in two codes for aero-servo-elastic simulations of wind turbines: the nonlinear aeroelastic multi-body model HAWC2 and the nonlinear geometrically exact beam model BeamDyn for OpenFAST. The main goal is to enable these tools to simulate the dynamic behavior of a wind turbine with variable blade inertia. However, current state-of-the-art load simulation tools for wind turbines cannot simulate variable blade inertia, so the source code of these tools must be modified. The validity of the modified codes is proven based on a simple beam model. The validation shows very good agreement between the modified codes of HAWC2, BeamDyn and an analytical calculation. The add-on of variable blade inertias is applied to reduce the mechanical loads of a 5-megawatt reference wind turbine with an integrated hydraulic-pneumatic flywheel in its rotor blades.

1. Introduction

The mechanical properties of wind turbines rotor blades should not change during their operational life. However, in many cases, these properties can be changed, e.g., in smart blades [1], by using a hydraulic-pneumatic flywheel [2] or structural control (StC) [3], or as a result of atmospheric ice accretion on the blades [4]. Such changes in the mechanical properties of rotor blades affect the behavior of wind turbines significantly. To analyze the effect of variable blade mechanical properties on the dynamic behavior of a WT, rotor blades with varying mechanical properties must be first implemented in wind turbine load simulation tools. Since state-of-the-art load simulation tools for wind turbines are designed to deal with constant mechanical blade properties only, the source code of these tools must be modified to allow for variation of mechanical properties during a simulation. This variation depends on the aforementioned cases. The case investigated in this paper is a flywheel. This is due to the possibility of applying this case exactly to other cases, e.g., atmospheric ice accretion on the blades and rotor imbalance or with small modifications for the StC and smart blade cases.

The flywheel used in this paper varies the inertia of the rotor blades by moving a fluid mass between a piston accumulator near the blade root and one or more piston accumulators near the blade tip [5,6]. Consequently, the eigenfrequencies of the rotor blades and, thus, the drive train and the tower of the wind turbine can be varied by the flywheel. Additionally, the flywheel causes a driving or braking torque independent of the aerodynamic torque. This enables the rotor to be accelerated or decelerated without pitching the rotor blades [2,6,7]. To vary the rotor inertia at any arbitrary operating point of a WT, the flywheel comprises electrically-driven pumps, which support the centrifugal forces by moving the fluid from the root to the tip accumulators [2,5,6,8].

Previous investigations of the implementation of variable blade mechanical properties in aero-elastic codes of wind turbines are limited to passive StC [3,9–13]. The application of StC in wind turbines refers to the addition of tuned mass dampers (TMDs) to a point in the blades, nacelle, tower, or substructure. The main purpose of TMDs is to enhance damping or to generate forces to control the structural response, e.g., reduce the variability in the platform, pitch, and tower top fore-aft displacement. The proposed flywheel can, in addition to its various StC applications, also support a power system in providing different gird services [14]. Examples of flywheel's StC applications are damping in-plane vibrations of the blades and tower, mitigating excitations from gravitation and wind shear, balancing rotors, and emergency braking [14]. The main flywheel's grid services are power system stabilization, steadying power infeed, fast frequency response, continuous inertia provision and low voltage ride-through [14]. However, implementing the flywheel in the aero-elastic code of a wind turbine requires a simultaneous variation of the inertia of several blade nodes. Moreover, all additional forces that result from the fluid movement along the rotating blades must be applied to the correct blade nodes.

The implementation of variable blade inertia in aero-elastic codes of wind turbines has been developed in the last nine years at the Wind Energy Technology Institute (WETI) at Flensburg University of Applied Sciences, Germany. Initially, a First Eigenmodes simulation model of a wind turbine was developed to enable the design of control algorithms [15]. The model was implemented in MATLAB/Simulink and consisted of different subsystems, which described the main components of a WT. The description level of the wind turbine components was very simple to facilitate quick simulations. Consequently, an exact response of a wind turbine with variable inertia at several nodes along the blade length could not be provided by this model. To do this, a load simulation tool is required that can describe the structural dynamics of the rotor blades in more detail. One such tool is ElastoDyn, a model developed by the National Wind Technology Centre at the National Renewable Energy Laboratory (NREL), USA, which is implemented within the aeroelastic modularization framework OpenFAST [16,17]. ElastoDyn is based on the Bernoulli-Euler beam theory and describes the mechanical properties of a rotor blade in greater detail than the First Eigenmodes simulation model. Like the First Eigenmodes simulation model, ElastoDyn is free, publicly available, and well-documented. The source code of Elasto-Dyn has previously been modified to implement variable blade inertia [18]. Although ElastoDyn uses a simple mathematical theory based on Kane's method [19] to establish equations of motion, the exact solutions of ElastoDyn met the needs of previous research, which also dealt with the hydraulic-pneumatic flywheel [18]. However, the method used in ElastoDyn to implement the resulting forces from the fluid movement simplifies these forces by applying a total (accumulative) torque at the hub [18]. This simplification does not consider the forces' impact on the blade nodes, which inhibits several applications of the flywheel, e.g., damping of in-plane vibrations of blades and mitigation of excitations from gravitation and wind shear, from being simulated. Furthermore, ElastoDyn only supports beams constructed from isotropic material without mass or elastic offsets, axial or torsional DOFs and shear deformation. For these reasons, it was obvious that the method of variable blade inertia had to be implemented in a more complex structural dynamics model of wind turbine rotor blades.

Two advanced structural dynamics models, HAWC2 [20] and BeamDyn [21] were chosen to compare and validate the implementation method of variable blade inertia. Both models utilize finite beam element theory to enable a very complex and advanced modelling methods of non-linear beam structural dynamics of the blade structure. The mechanical properties of several blade cross-sections are defined in these models by tabular mass and stiffness matrices. These are used in the numerical solution of the dynamic equations during a given simulation. In addition to the extensive description of the blade's mechanical properties, a previous comparison of HAWC2 and BeamDyn showed that both models are capable of computing accurate solutions for highly nonlinear effects [22].

The method used to implement variable blade inertia and the differences obtained by applying this method in HAWC2 and BeamDyn are presented in detail in the following section. In Section 3, the modified HAWC2 and BeamDyn models are shown to be valid for analytical calculations of three benchmarking cases of increasing complexity. An application of variable blade inertia is presented for both models in Section 4, where emergency braking is supported with the hydraulic-pneumatic flywheel.

2. Implementation of Variable Blade Inertia in HAWC2 and BeamDyn

Although the definition of beam elements in the HAWC2 and BeamDyn models differs, the mathematical description of the implementation of variable blade inertia is the same in both models. However, due to the differences in the program structure and the accessibility of the source codes of these models, two distinct implementation methods are required.

It should be noted that in this section, the matrix notation is used to denote vectorial or vectorial-like quantities. For example, vectors are denoted by an underline ($\underline{\bullet}$), a double underline ($\underline{\underline{\bullet}}$) denotes a tensor, and an overline ($\overline{\bullet}$) denotes a unit vector.

2.1. Superordinate Model Calculations

As discussed in the introduction, this study focuses on the variation of blade inertia resulting from a change in the global charge state of the tip accumulator, γ_{tip}, of a hydraulic-pneumatic flywheel. This control variable indicates whether the tip accumulators of individual blades are empty $(\gamma_{tip} = 0)$, or either partly $(0 < \gamma_{tip} < 1)$ or fully charged with fluid $(\gamma_{tip} = 1)$. Based on this variable, its derivatives and the flywheel geometry, the variable properties of the flywheel, such as fluid velocity, mass flow, and Coriolis forces, can be calculated. The equations used in this calculation are presented in Sections 2.1.1 and 2.1.2. They are implemented identically in HAWC2 and BeamDyn.

2.1.1. Local Charge State

The flywheel in each blade has three main components: root accumulator, pipe, and tip accumulator. Each component consists of one or more elements. These elements' geometrical and mechanical parameters are integrated into the beam element's properties, which are defined in the input file of the model initialization. The integration comprises the definition of the start, $\underline{R}_{n1,i}$, and the end, $\underline{R}_{n2,i}$, node positions of every flywheel element, i, within each flywheel component, j. The geometrical and mechanical parameters for the tip accumulator are shown in Figure 1.

Using the start, $\underline{R}_{n1,i,j}$, and end, $\underline{R}_{n2,i,j}$, positions of the flywheel elements, the single element lengths, $l_{i,j}$, as well as the total lengths, L_j, of each of the three flywheel components can be determined using Equations (1) and (2).

$$l_{i,j} = \left| \underline{R}_{n1,i,j} - \underline{R}_{n2,i,j} \right| \tag{1}$$

$$L_j = \sum_i l_{i,j} \tag{2}$$

Equation (3) expresses the global charge state of the tip accumulator, γ_{tip}, as the ratio of the volume filled by a fluid, V_{fl}, to the total volume of the tip accumulator, V_{tip}.

$$\gamma_{tip} = \frac{V_{fl}}{V_{tip}} \tag{3}$$

$$V_{tip} = \frac{\pi}{4} \cdot D_{tip}^2 \cdot L_{tip} \tag{4}$$

$$V_{fl} = \frac{\pi}{4} \cdot D_{tip}^2 \cdot L_{fluid\_tip} \tag{5}$$

where V_{tip} and V_{fl} in Equations (4) and (5), respectively, are determined from the diameter, D_{tip}, the fluid length, L_{fluid_tip}, and the total length of the tip accumulator, L_{tip}. The global charge state of the root accumulator, γ_{root}, and the local charge state, $\gamma_{i,j}$, in each element of the flywheel components, can subsequently be derived from the global charge state of the tip accumulator, γ_{tip}.
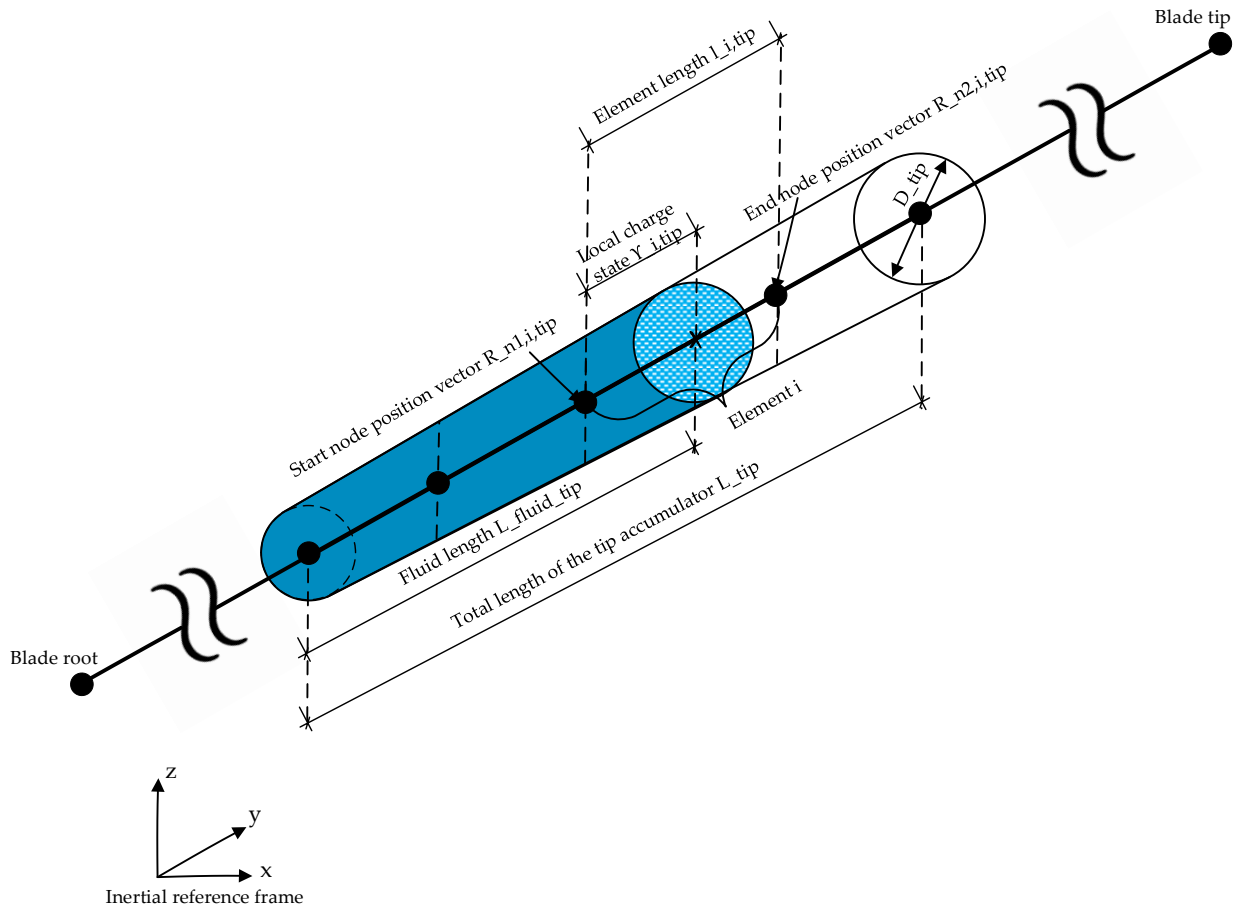

Figure 1. Geometrical input parameters of the tip accumulator.

The flow rate in the pipe, root and tip accumulators is constant due to the continuity and incompressibility of the fluid. Thus, the rate of change of the tip charge state, $\dot{\gamma}_{tip}$, can be used in Equation (6) to determine the fluid velocities, v_{fl}, based on the cross-sectional area, A_j, of the flywheel component j:

$$v_{fl,i,j} = \frac{V_{tip} \cdot}{A_j} \tag{6}$$

Similarly, the fluid acceleration, a_{fl}, can be calculated from from Equation (7):

$$a_{fl,i,j} = \frac{\partial v_{fl,i,j}}{\partial t} = \frac{V_{tip} \cdot \ddot{\gamma}_{tip}}{A_j} \tag{7}$$

where $\ddot{\gamma}_{tip}$ is the rate of change of $\dot{\gamma}_{tip}$.

2.1.2. Additional Forces Induced by the Flywheel

Three forces are induced by the relative motion of the fluid inside the flywheel components. The forces correspond to the exchange of the angular momentum between the blade's stationary structure and the fluid masses. Therefore, the implementation of these forces in

HAWC2 and BeamDyn is crucial for a correct representation of the operating flywheel. The three forces are graphically presented in Figure 2 and are briefly explained below:
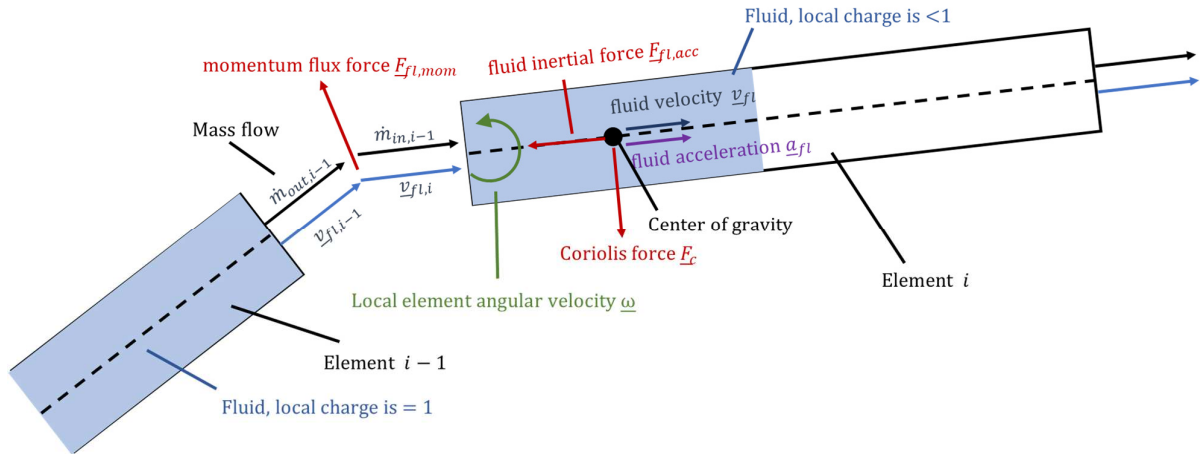
1. **Coriolis forces**

Figure 2. Coriolis force, fluid inertial force, and momentum flux force induced by the flywheel in a free body diagram of two adjacent flywheel elements.

The radial movement of the fluid in the flywheel as the blades rotate produces Coriolis forces. Equation (8) expresses the Coriolis force, $\underline{F}_c$, that is applied to the center of gravitation (COG) of a considered element in terms of the cross product, $\times$, the rotational speed of the element, $\underline{\omega}$, with the fluid translational velocity, $\underline{v}_{fl}$, of a fluid mass, m, that is crossing this element.

$$\underline{F}_c = -2 \cdot m \cdot \left(\underline{\omega} \times \underline{v}_{fl} \right) \tag{8}$$

2. **Fluid inertial forces**

Acceleration or deceleration of fluid in time causes fluid inertial forces. These forces balance the change of the stored momentum inside the fluid due to the change in the mass flow. Equation (9) expresses the fluid inertial forces in terms of multiplication of the fluid mass, m, with the fluid acceleration, $\underline{a}_{fl}$.

$$\underline{F}_{fl,acc} = -m \cdot \underline{a}_{fl} \tag{9}$$

3. **Momentum flux forces**

The change of flow direction or local flow speed of a fluid due to a sudden change in the cross-sectional area causes hydraulic reaction forces to balance the difference in the transported momentum between the inlet and the outlet of a control volume. These forces are called momentum flux forces, $\underline{F}_{fl,mom,i}$, and shown in Equation (10) as a difference in the hydraulic reaction forces between two neighbors elements.

$$\underline{F}_{fl,mom,i} = \left(\dot{m}_{out} \cdot \underline{v}_{fl} \right)_{i-1} - \left(\dot{m}_{in} \cdot \underline{v}_{fl} \right)_i \tag{10}$$

where $\left(\dot{m}_{out} \right)_{i-1}$ is the fluid mass flow at the outlet of the previous element, $i-1$, and $\left(\dot{m}_{in} \cdot \underline{v}_{fl} \right)_i$ is the fluid mass flow at the inlet of the considered element, i.

If these three forces are treated correctly within the HAWC2 and BeamDyn models, the conservation law of momentum and angular momentum of a wind turbine with a flywheel in its rotor should still hold.

Other forces, which are related to the stationary effects of the additional fluid masses inside the blade, are independent of the translational motion of the fluid. These forces, e.g., gravitational, centrifugal, gyroscopic, and inertial forces from fluid without relative

motion in any arbitrary direction, are handled inside the original implementation methods in HAWC2 and BeamDyn.

2.2. Implementation of Variable Blade Inertia in HAWC2

HAWC2 is a state-of-the-art aeroelastic code developed by DTU [20] and used in academia and industry. The structural dynamics model of HAWC2 is based on the flexible multibody approach using interconnected bodies consisting of Timoshenko finite-element beams. The body motions are described by a method called 'floating frame of reference' [20], described in [23]. The equations of motion (EOM) use a redundant set of coordinates consisting of the body reference motion DOFs, the relative elastic motion DOFs and a set of algebraic constraints [20].

Since HAWC2 is a closed source, users cannot create more complex models by changing the source code. For this reason, the HAWC2 developers created a DLL programming interface called the External System interface [24]. This allows the user to define general second-order dynamic equations and general algebraic constraints outside the HAWC2 core in user-written DLL files. The added external DOFs defined in the DLL files are solved as additional generalized coordinates with the HAWC2 coordinates in a common equation system [25]. This approach has previously been applied to simulate a planetary gearbox and dynamic mooring lines along with the HAWC2 beam models [24] and was chosen in the present work as the basis for developing a flywheel model extension with variable inertia.

The general second-order differential-algebraic dynamic equation system of the External System's DOFs and external constraints in a user-written DLL takes the form of Equations (11) and (12) [24]:

$$\underline{\underline{M}} \cdot \ddot{\underline{q}} + \underline{\underline{C}} \cdot \dot{\underline{q}} + \underline{\underline{K}} \cdot \underline{q} - \underline{F} + \underline{\underline{G}}_e \cdot \underline{\lambda} = \underline{0} \tag{11}$$

and

$$\underline{g} = \underline{0} \tag{12}$$

where $\underline{M}$, $\underline{C}$ and $\underline{K}$ are the External System's mass, damping and stiffness matrices, respectively. The generalized acceleration, velocity, and coordinates (consisting of the External System's DOFs) are represented by $\ddot{q}$, $\dot{q}$ and q, respectively. $\underline{F}$ is the vector of the sum of generalized external forces. The constraint Jacobian matrix, $\underline{\underline{G}}_e$, and the vector of Lagrange Multipliers, $\underline{\lambda}$, are associated with the algebraic constraint equations $\underline{g}$. $\underline{\underline{G}}_e$ and $\underline{\lambda}$ represent constraint reaction forces and transfer loads between the External System and HAWC2 bodies.

The HAWC2 solver solves the set of Equations (11) and (12) together with the internal equations of the multibody system with respect to time. This ensures a tight coupling of the External Systems' dynamic models with the original multibody system.

2.2.1. Model Idea and Assumptions

The main idea of the flywheel implementation in HAWC2 is based on the fact that variable inertia can be added via External System, which uses Equations (11) and (12) to describe the physical properties.

The overall implementation concept consists of the following ideas and assumptions:

a. By applying fluid dynamics theory using the Eulerian description, the fluid in the flywheel can be subdivided into several elements forming control volumes (CV), which are fixed relative to the blade beams. Each element is then modeled as an External System.

b. The effects of the contained (static) fluid mass in the CV, which can vary over time, can be addressed by changing the mass matrices $\underline{M}$ and forces $\underline{F}$ associated with the contained mass.

c. The effects associated with the change of the fluid mass (cf. Section 2.1.2) must be added as external forces $\underline{F}$ acting on the CV. These effects are otherwise not covered by elements with constant properties, and they are crucial to fulfil the conservation law of momentum.

d.   To simplify the momentum balance and calculation of mass matrices, a 'lumping' approach was chosen. This means that the flexible pipes and accumulators are approximated as piecewise rigid segments, and the deformation of a single element as the blade bends is neglected. Thus, each element is of constant size and not deformable, implying it can be reduced to a rigid body. The bending of the pipes and accumulators with blade bending is modeled as relative rotation between the rigid elements rather than modelling deformations. This also implies that the stiffness matrix $\underline{K}$ and the damping matrix $\underline{C}$ in Equation (11) are 0, and are no DOFs needed to model deformations.

e.   Because the constant-sized CVs are chosen to be cylindrical and straight, stream tube theory can be applied to model the forces from fluid dynamics. Fluid is assumed to change its flow direction only at the connection between two adjacent flywheel elements. From these assumptions, it follows that Equations (8)–(10) are sufficient to satisfy the conservation of momentum in the flywheel.

The implementation concept for the flywheel is shown schematically in Figure 3 for a simple HAWC2 simulation model with flywheel elements as External Systems at one blade. This concept uses DLLs developed by AEROVIDE GmbH. The flywheel can be independently controlled by external control software. The only control signals required during simulation are the global charge state of each blade and its derivatives.
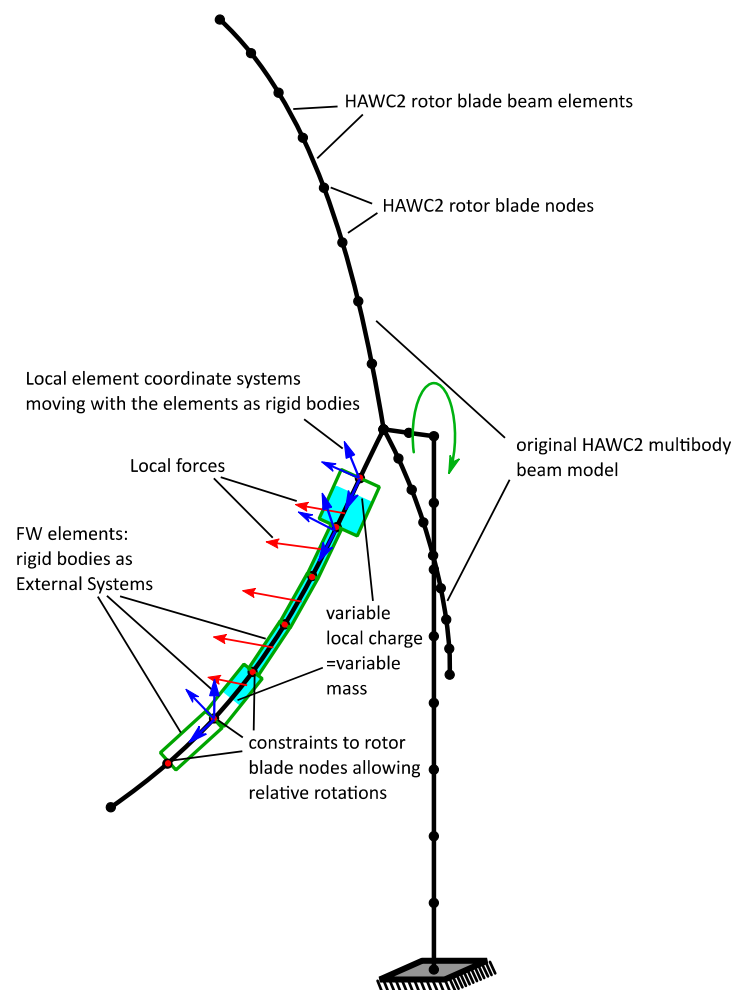

Figure 3. Schematic of a simple HAWC2 simulation model and the additional External System model with flywheel elements shown at one rotor blade.

2.2.2. Equations of Motion and the Definition of DOFs

As each flywheel element is assumed to represent a rigid body in 3D space, the Newton-Euler equations are suitable [23] to model their motion and were used in the implementation of the flywheel model. There are six Newton-Euler equations, (three for translation and three for rotation), which can be seen in Equation (13) as a specific form of the general dynamic equations of the External System's DOFs.

$$\underline{\underline{M}} \cdot \begin{pmatrix} \ddot{\underline{R}} \\ \dot{\underline{\omega}} \end{pmatrix} = \begin{pmatrix} \underline{F}_v \\ \underline{M}_v \end{pmatrix} + \begin{pmatrix} \underline{F}_g \\ \underline{M}_g \end{pmatrix} + \begin{pmatrix} \underline{F}_c \\ \underline{M}_c \end{pmatrix} + \begin{pmatrix} \underline{F}_{fl} \\ \underline{0} \end{pmatrix} - \underline{\underline{G}}_e \cdot \underline{\lambda} \tag{13}$$

where the newly introduced variables in the equation are defined as follows. $\underline{F}_g$ is the gravitational force. $\underline{F}_c$ is the Coriolis force from Equation (8). $\underline{F}_{fl}$ is the sum of the fluid inertial force and the moment force at the element, see Equations (9) and (10). $\underline{M}_g$ and $\underline{M}_c$ the offset moments of the gravitational force and the Coriolis force, respectively, caused by the variable COG offset to the element's origin. $\underline{F}_v$ and $\underline{M}_v$ are the centrifugal and gyroscopic force and moment terms, respectively, which occur in the Newton-Euler equations [23]. The vector $\underline{R}$ denotes the element origin's position and is discussed further in the following paragraph.

The Newton-Euler equations are characterized by a specific choice of coordinates for the description of rigid body motion with geometric meanings: The three translational motion DOFs are described by the element origin's position vector $\underline{R}$ and the acceleration $\ddot{\underline{R}}$, measured in global HAWC2 coordinates. The global HAWC2 coordinates are fixed in space at the ground and thus serve as the inertial reference frame (see HAWC2 manual [20]). The three rotational DOFs are described by the local angular velocity vector $\underline{\omega}$ and the local angular acceleration $\dot{\underline{\omega}}$, measured around the element's axes. These axes are rigidly fixed to the element and thus always rotate with the element relative to the global HAWC2 coordinates.

As the integrated local rotation coordinates, see Equation (14), do not contain unique 3D orientation information of the local element's axes [23], the rotations need to be calculated in another way to define the orientation of the local element's axes. To do so, Euler parameters, θ, are used as extra rotation coordinates, as the time derivates of the Euler parameters, $\dot{\theta}$, are related to the local angular velocity vector $\underline{\omega}$ [23]. During each HAWC2 solver update of the 6 External System DOFs ($\underline{R}$, $\dot{\underline{R}}$, $\ddot{\underline{R}}$, φ, $\underline{\omega}$, and $\ddot{\underline{\omega}}$), the associated Euler parameters can be updated by integration, accordingly. The Euler parameters can then be transformed into an element rotation matrix, $\underline{A}$, for each time step. The rotation matrix $\underline{\underline{A}}$ finally defines the orientation of the local element's axes with respect to the global HAWC2 coordinate axes [23] (see Figure 3) and is therefore required to transform forces and moments from the local element coordinates to the global HAWC2 coordinates and vice versa.

$$\underline{\varphi} = \int \underline{\omega} \mathrm{d}t \tag{14}$$

The element origin position described by $\underline{R}$ is chosen to be equal to the element's start node position $\underline{R}_{n1,i,j}$. Thus, the origin position and the variable COG position are decoupled. This is a requirement of model assumption (a.), see Section 2.2.1. The local axes relative to the element are defined with the z-axis pointing from the origin to the element's end node position, $\underline{R}_{n2,i,j}$. Consequently, the z-axis always points in the direction of the element's length axis. The x- and y-axis orientations are arbitrarily chosen to be radial to the element, forming a right-handed Cartesian coordinate system (see Figure 4).

The mass matrix of a flywheel element is continuously updated via the superordinate model calculations as the charge state varies. Consequently, the mass matrix in Equation (15) takes the form partitioned into translational and rotational DOFs:

$$\underline{\underline{M}} = \begin{pmatrix} \underline{\underline{I}}_3 \cdot m & -\underline{\underline{A}} \cdot \widetilde{\underline{u}}_g \cdot m \\ -\underline{\underline{A}} \cdot \widetilde{\underline{u}}_g \cdot m & \underline{\underline{J}}_g - m \cdot \widetilde{\underline{u}}_g \cdot \widetilde{\underline{u}}_g \end{pmatrix} \tag{15}$$

where $\underline{\underline{I_3}}$ is the 3×3 identity matrix and m is the contained mass. $\underline{u}_g = \begin{pmatrix} 0 \\ 0 \\ z_g \end{pmatrix}$ is the

center of gravity measured in local element coordinates and $\widetilde{\underline{u}}_g = \begin{pmatrix} 0 & -z_g & 0 \\ z_g & 0 & 0 \\ 0 & 0 & 0 \end{pmatrix}$ is the

skew-symmetric matrix associated with $\underline{u}_g$. Last, $\underline{\underline{J_g}}$ is the inertia tensor measured in local element coordinates referred to as the center of gravity.

In the calculation of the mass properties of the elements, they are considered to be solid fluid cylinders with the calculated height of the fluid in the element and the diameter of the element.
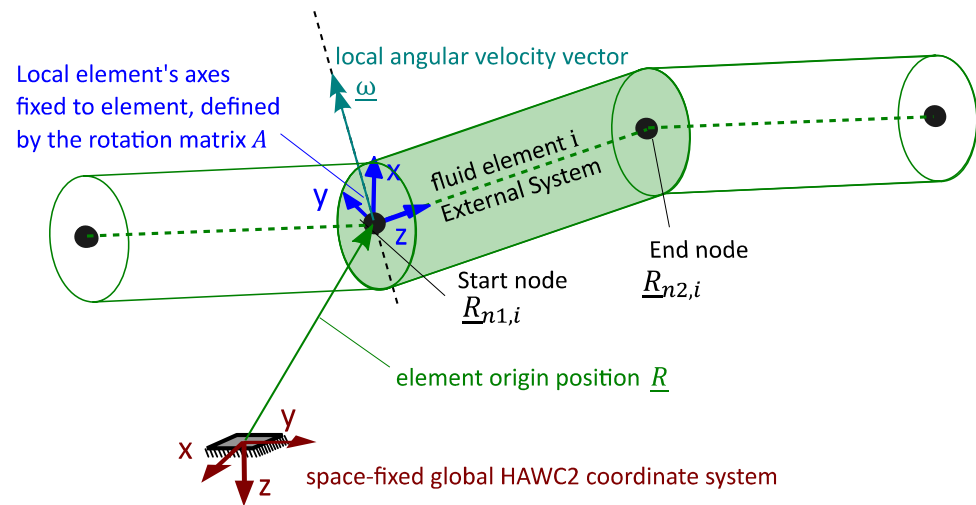

Figure 4. Schematic visualization of a flywheel element modeled as an external system, showing the global HAWC2 coordinate and the local element coordinate systems, as well as the vectors associated with the motion DOFs of the element.

2.2.3. Constraints

Without constraints, the Newton-Euler equations would allow the flywheel elements to move freely in the 3D space. As the flywheel elements represent additional masses inside the rotor blades, the constraints are formulated such that flywheel elements are always moving with the rotor blade. The start and end nodes of adjacent elements are always linked like a chain, even under blade pre-bending and bending. This can be achieved by constraining both the start and the end nodes of each element, $\underline{R}_{n1,i,j}$ and $\underline{R}_{n2,i,j}$, to nearby nodes of the rotor blade body and allowing rotations of the element relative to the rotor blade nodes. One disadvantage of this approach is that a non-tree-like structure is created because of constraints at two positions on each element. The non-tree-like structure is commonly called a 'kinematic loop' [25] and causes increased stiffness of the rotor blade when statically overdetermined constraints are used.

So that the kinematic loop does not change blade stiffness or impose numerical problems, the constraint equations of the flywheel elements are chosen so that each flywheel motion DOF is restricted only once. As in applied mechanics, this is achieved in the model by using algebraic constraint equations as a statically-determined simple support for the flywheel element. The constraints describe a 3-dimensional fixed-floating bearing setup for each flywheel element. Using the fixed-free bearing setup does not lead to constraint reaction forces at the bearings by bending, axial elongation or torsion between two rotor blade nodes, and thus, there is no influence on the stiffness.

The start and end node positions of the elements, $\underline{R}_{n1,i,j}$ and $\underline{R}_{n2,i,j}$ respectively, can be chosen to coincide with the nodes of the rotor blade body. However, placing the flywheel elements near the rotor blade nodes with a radial offset is also possible. This might be

desired, e.g., to let the flywheel element's length axis coincide with the blade's mass axis or to follow the real geometric position of the flywheel component. Both may have an offset to the axis formed by the blade nodes.

The constraint setup and the allowed relative motions are visualized in Figure 5. The required constraint equations can be taken from multibody simulation and robotics textbooks (e.g., [23]).
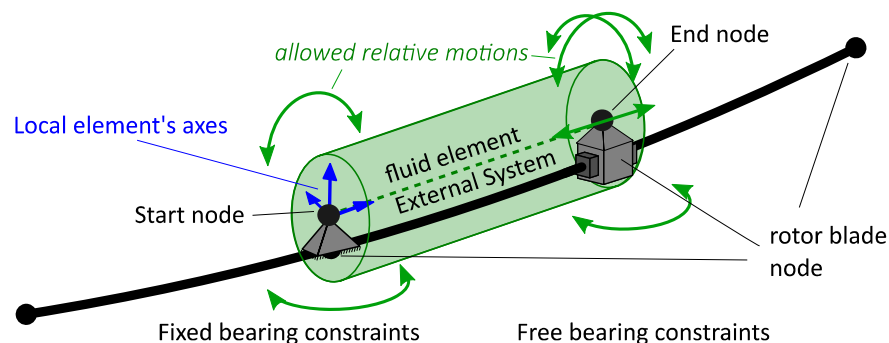

Figure 5. Constraint setup of one exemplary flywheel element constraint to a rotor blade in the HAWC2 implementation.

The fixed bearing restricts relative translational motion between the flywheel element's start node and a rotor blade node, and additionally rotation around the length axis. The floating bearing only restricts relative translational motion between the flywheel element's end node and a rotor blade node radial to the element's length axis.

2.3. Implementation of Variable Beam Inertia in BeamDyn

BeamDyn is a nonlinear beam finite element model for simulating slender structures created by the National Wind Technology Center at the National Renewable Energy Laboratory (NREL), USA [21]. The model is used by the FAST aero-hydro-servo-elastic wind turbine multi-physics engineering tool to model blade structural dynamics. BeamDyn uses geometrically exact beam theory (GEBT) [26]. A spatial discretization for the GEBT beam equations is accomplished with Legendre spectral finite elements (LSFEs) [27]. The combination of GEBT and LSFEs enables BeamDyn to model long, flexible, composite wind turbine blades with a single high-order element [21].

BeamDyn is open-source software, which can be used to model the flywheel directly in its source code. The modelling concept is based on a variable change of the cross-sectional mass matrices during a given simulation and the addition of the forces induced by the flywheel to the external distributed forces, e.g., aerodynamic forces, hydrodynamic forces, and user-defined loads in the BeamDyn input file.

2.3.1. Modification of the Mass Matrix

A blade input file defines the mechanical parameters of the blade in the form of cross-sectional mass and stiffness matrices at various stations along a blade and six damping coefficients for the whole blade. These parameters are defined as constants in the initialization source code of BeamDyn. Hence, these parameters, e.g., the mass matrix, $\underline{M}$, in Equation (16), do not change their values during a simulation. The source code of BeamDyn is modified so the cross-sectional mass matrix parameters are changed from time-invariant parameters to time-variant variables. This modification takes place at the beginning of the dynamic solution of BeamDyn to ensure that all forces associated with the additional fluid masses are updated correctly.

The original, $\underline{\underline{\mathcal{M}}}$, and the modified, $\underline{\underline{\mathcal{M}}}^*$, sectional mass matrices are given by Equations (16) and (17), respectively.

$$\underline{\underline{\mathcal{M}}} = \begin{bmatrix} m & 0 & 0 & 0 & 0 & -mY_{cm} \\ 0 & m & 0 & 0 & 0 & mX_{cm} \\ 0 & 0 & m & mY_{cm} & -mX_{cm} & 0 \\ 0 & 0 & mY_{cm} & i_{Edg} & -i_{cp} & 0 \\ 0 & 0 & -mX_{cm} & -i_{cp} & i_{Flp} & 0 \\ -mY_{cm} & mX_{cm} & 0 & 0 & 0 & i_{plr} \end{bmatrix} \tag{16}$$

$$\underline{\underline{\mathcal{M}}}^* = \begin{bmatrix} m + m_{fluid} & 0 & 0 & 0 & 0 & -mY_{cm} \\ 0 & m + m_{fluid} & 0 & 0 & 0 & mX_{cm} \\ 0 & 0 & m + m_{fluid} & mY_{cm} & -mX_{cm} & 0 \\ 0 & 0 & mY_{cm} & i_{Edg} + i_{fluid} & -i_{cp} & 0 \\ 0 & 0 & -mX_{cm} & -i_{cp} & i_{Flp} + i_{fluid} & 0 \\ -mY_{cm} & mX_{cm} & 0 & 0 & 0 & i_{plr} + 2i_{fluid} \end{bmatrix} \tag{17}$$

where m and m_{fluid} are the blade structural and the fluid mass density per unit span, respectively. The local coordinates of the sectional center of mass are expressed by X_{cm} and Y_{cm}. i_{Edg}, i_{Flp} and i_{fluid} are the edge, flap, and fluid mass moments of inertia per unit span, respectively. i_{cp} is the sectional cross-product of inertia per unit span; and i_{plr} is the polar moment of inertia per unit span.

2.3.2. Additional External Distributed Forces

Externally applied loads, including uniformly distributed, point, and tip-concentrated forces, can be defined in the input file of BeamDyn. By customizing the source code, BeamDyn can handle more complex external force cases, such as those induced by the flywheel. Hence, the three aforementioned types of forces are in Section 2.2.2. (Coriolis forces, fluid inertial forces and momentum flux forces) They are defined as distributed forces in the dynamic solution subroutines, which are applied at every time step. $\mathcal{F}_{add}$, shown in Equation (18), is the addition of the x, y, and z components of the distributed Coriolis forces, $\underline{\mathcal{F}_c}$, the distributed fluid inertial forces, $\underline{\mathcal{F}_{fl\_acc}}$, and the momentum flux forces, $\underline{\mathcal{F}_{fl\_mom}}$, in the local coordinates.

$$\underline{\mathcal{F}_{add}} = \underline{\mathcal{F}_c} + \underline{\mathcal{F}_{fl\_acc}} + \underline{\mathcal{F}_{fl\_mom}} \tag{18}$$

Since, the source code allows for the input of applied distributed loads in the global coordinate system, the additional forces, $\underline{\mathcal{F}_{add}}$, must be transformed to the global coordinate system. This transformation is shown in Equation (19).

$$\underline{\mathcal{F}_{add}^G} = \underline{\underline{\mathcal{R}}} \cdot \underline{\mathcal{F}_{add}} \tag{19}$$

where $\underline{\mathcal{F}_{add}^G}$ represents the additional forces in the global coordinate system and $\underline{\underline{\mathcal{R}}}$ is the rotation tensor expressed in terms of Wiener-Milenković parameters [28,29]. The additional forces, $\underline{\mathcal{F}_{add}^G}$ can be added to the applied distributed loads.

FAST_SFunc is used to input the global charge state signals and their derivatives in the source code of BeamDyn. FAST_SFunc is a FAST interface to Simulink, implemented as a Level-2 S-Function. The Level-2 S-Function is a Simulink block written in C, and it calls a DLL of FAST routines written in Fortran [30,31]. This interface allows external modules, such as the control and auxiliary systems of the hydraulic-pneumatic flywheel, to be implemented in Simulink. During a simulation, the flywheel can be simulated together with the nonlinear aero-elastic tool OpenFAST [32]. However, to pass the flywheel signals through FAST_SFunc, the source code of the OpenFAST glue code needs to be modified. This is because FAST_SFunc is set up to receive only the control signals from the OpenFAST

standard modules, such as generator torque control, nacelle yaw control, pitch control, and high-speed shaft brake.

3. Validation

In this section, three benchmarking cases are discussed. The complexity of the cases increases gradually. The main objective of these cases is to validate the method used in HAWC2 and BeamDyn to implement variable blade inertia. The validation is based on the proof of the physical laws of the equilibrium conditions and the conservation of angular momentum. The physical laws are analytically computed and compared with simulation results from the modified HAWC2 and BeamDyn models in all three cases.

It needs to be mentioned here that BeamDyn standalone is only set up to define a constant angular rotation of the beam root about its rotation axis. Complex root motions such as those treated in Cases 2 and 3 can only be simulated when BeamDyn is used within the wind turbine simulation tool OpenFAST. However, running BeamDyn within OpenFAST requires the specification of some physically realistic generator rotational inertia, even when the generator model is deactivated. Hence, a generator inertia of 115,926 kg-m^2 is used in the simulation and the analytical calculation.

The HAWC2 models for the benchmarking cases are defined in accordance with the demands from BeamDyn within OpenFAST. Hence the same beam parameters and additional generator rotational inertia are used.

3.1. Case 1: Fixed Rotational Speed of a Fixed, Supported, Straight and Stiff Beam

Case 1 concerns the reaction forces and moments of a fixed supported beam subjected at its fixed end to a constant rotational speed around the x axis and axial fluid movement along the z axis.

The beam is straight and discretized in 15 elements. The length of each element is 1 m. Three hydraulic components are integrated into the beam: pipe, root, and tip accumulators. Each component has five elements. The total fluid mass moved between the root and the tip accumulators equals 500 kg. A schematic drawing of the beam in charge states 0 and 1 is shown in Figure 6a,b, respectively.

When the charge state equals 0, the root accumulator is full, and the tip accumulator is empty. Conversely, the root accumulator is empty, and the tip accumulator is full when the charge state equals 1. The charge state, therefore, varies between 0 and 1 as the fluid moves between the root and the tip accumulators.

The beam's input cross-sectional mass and stiffness parameters are presented in Table 1. In Case 1 and later in Case 2, the beam stiffnesses are set to very high values to prevent the beam from bending. This keeps the local coordinates of the beam elements synchronized with the root coordinates of the beam at the fixed end coordinates of the beam and simplifies the analytical calculation of the reaction forces and moments.

Table 1. Cross-sectional mechanical properties of the straight and stiff beam.

Beam Elementmass Density	Flap and Edge Mass Moments of Inertia per Unit Span	Flap Stiffness	Edge Stiffness	Flap Shear Stiffness	Edge Shear Stiffness	Torsional Stiffness
kg/m	kg·m	N·m^2	N·m^2	N·m^2	N·m^2	N·m^2
50	50	1.00×10^{10}	1.00×10^{10}	5.00×10^8	5.00×10^8	1.00×10^9

For Case 1, the simulation scenario presented in Figure 7 sets the rotational speed to a constant value of 10 rpm. The charge state rises from 0 to 1 between 10 s and 50 s and remains constant till 60 s. Between 60 s and 100 s the charge state is reduced from 1 to zero and remains at 0 until the end of the simulation. Reaction forces and moments result from the fluid movement. The x, y and z components of these forces and moments

are analytically calculated and compared with the corresponding simulation results from HAWC2 and BeamDyn. The comparisons in Figure 7 show a very good agreement between the analytical and the simulated results of all components. The increase/decrease of the y component of the reaction force is due to the Coriolis forces that result from the change in the charge state. Hence, a reaction moment around the x axis results from these Coriolis forces. The z component of the reaction force illustrates the sum of the centrifugal and fluid inertial forces. The variation in the centrifugal forces results from the change in the COG of the beam due to the fluid motion. The fluid inertial forces (Equation (9)) can be seen, when the fluid accelerates, e.g., from 10 to 11 s, or deaccelerates, e.g., from 50 to 51 s.
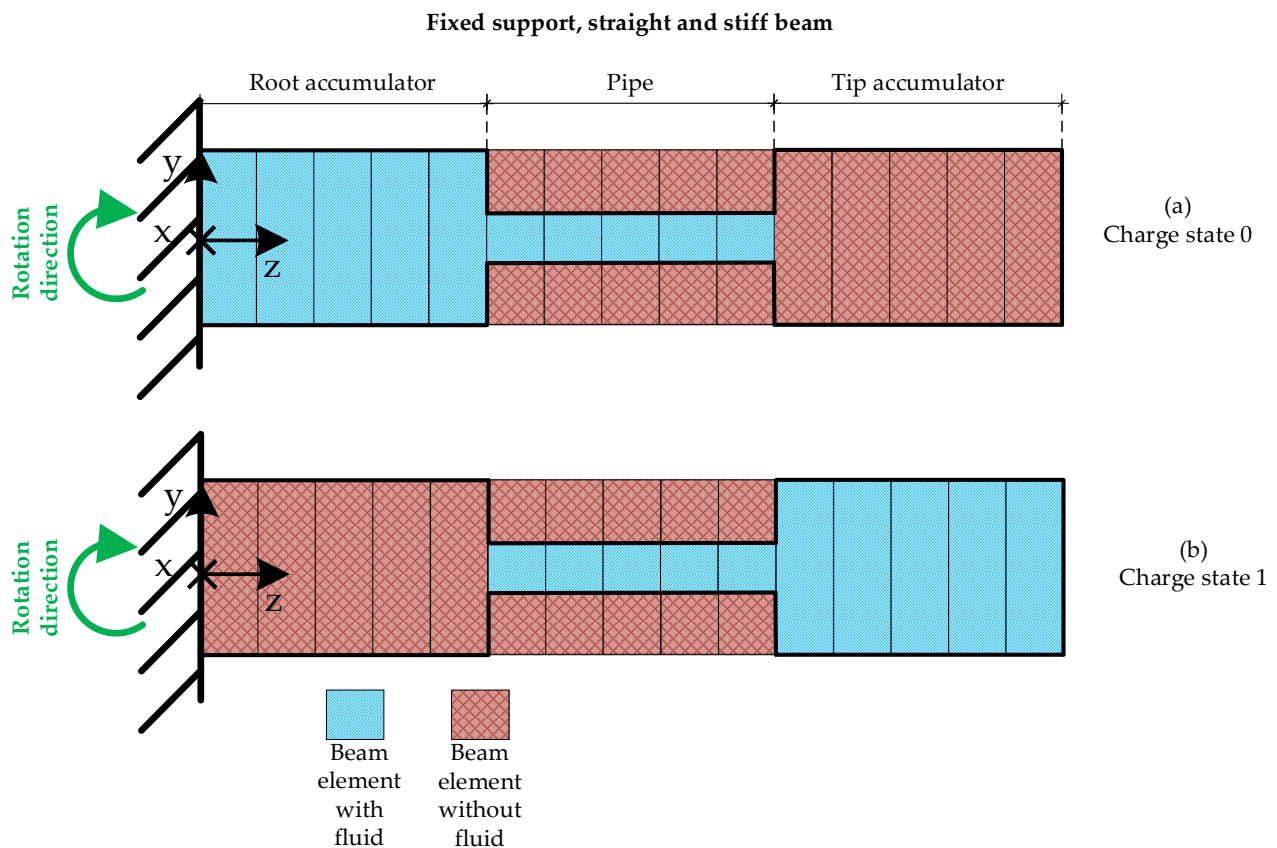

Figure 6. Schematic drawing of the pipe, root and tip accumulators in a fix supported, straight and stiff beam in (**a**) a discharged state and (**b**) a fully charged state.

3.2. Case 2: A Pinned-Supported, Straight and Stiff Beam

The purpose of Case 2 is to prove the conservation of angular momentum when the beam inertia changes in a free rotational system. Case 2 uses the same beam used in Case 1, pinned supported. See Figure 8. This support enables the beam to rotate freely and prevents translational movement at the supported end. Since the angular momentum in a free rotational system remains constant, the rotational speed of the beam decreases when the beam inertia increases, and vice versa. On this basis, the variable rotational speed of the beam can be analytically calculated. The analytically calculated rotational speed can be used as a reference value to validate the simulated rotational speed from HAWC2 and BeamDyn. Case 2 uses the same simulation scenario used in Case 1. Figure 9 shows that the increase in charge state leads to an increase in beam inertia and, thus, to a decrease in rotational speed. Conversely, the rotational speed increases when the charge state decreases. The comparison of the analytical calculation with the simulated results in Figure 9b shows a very good agreement.
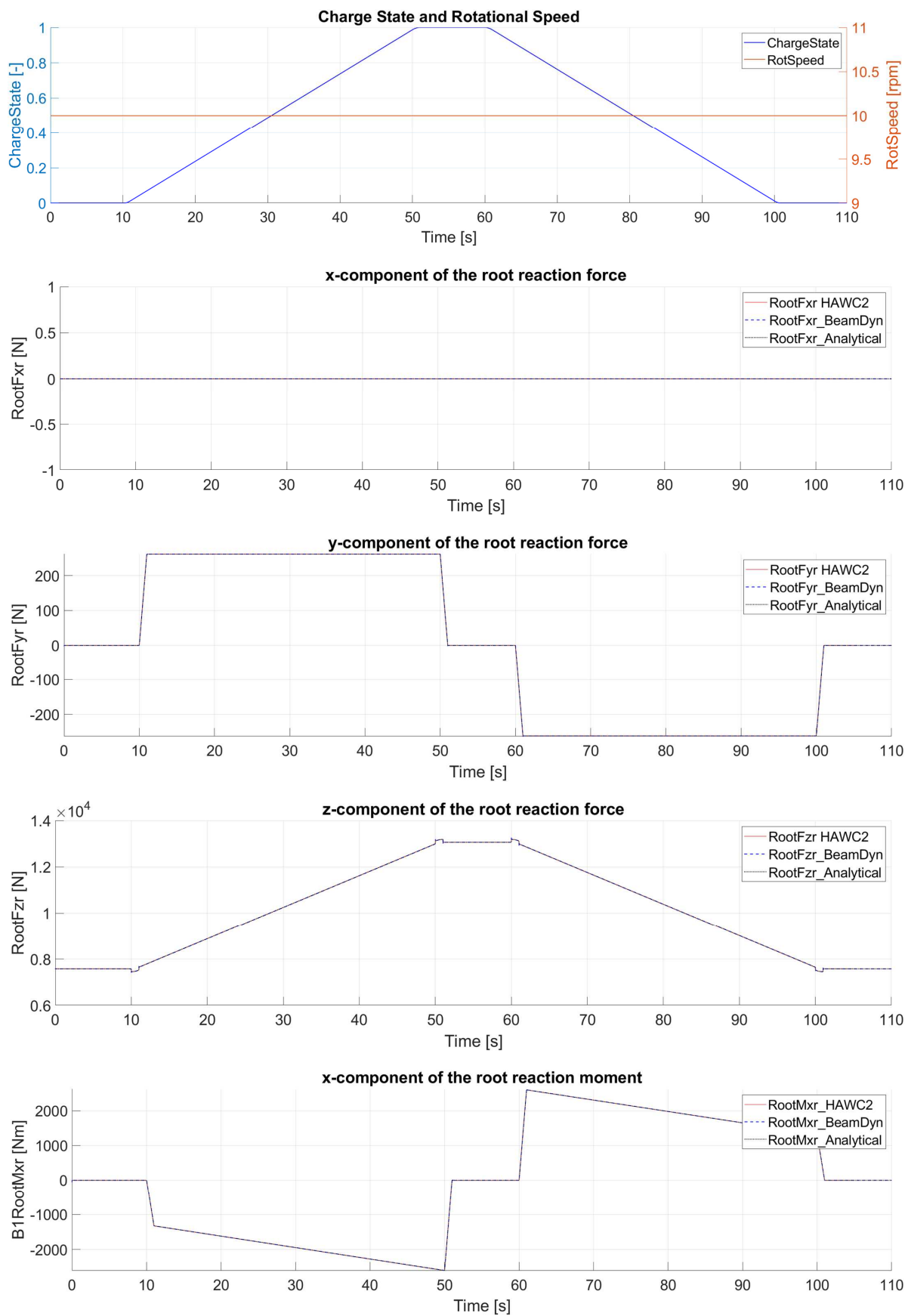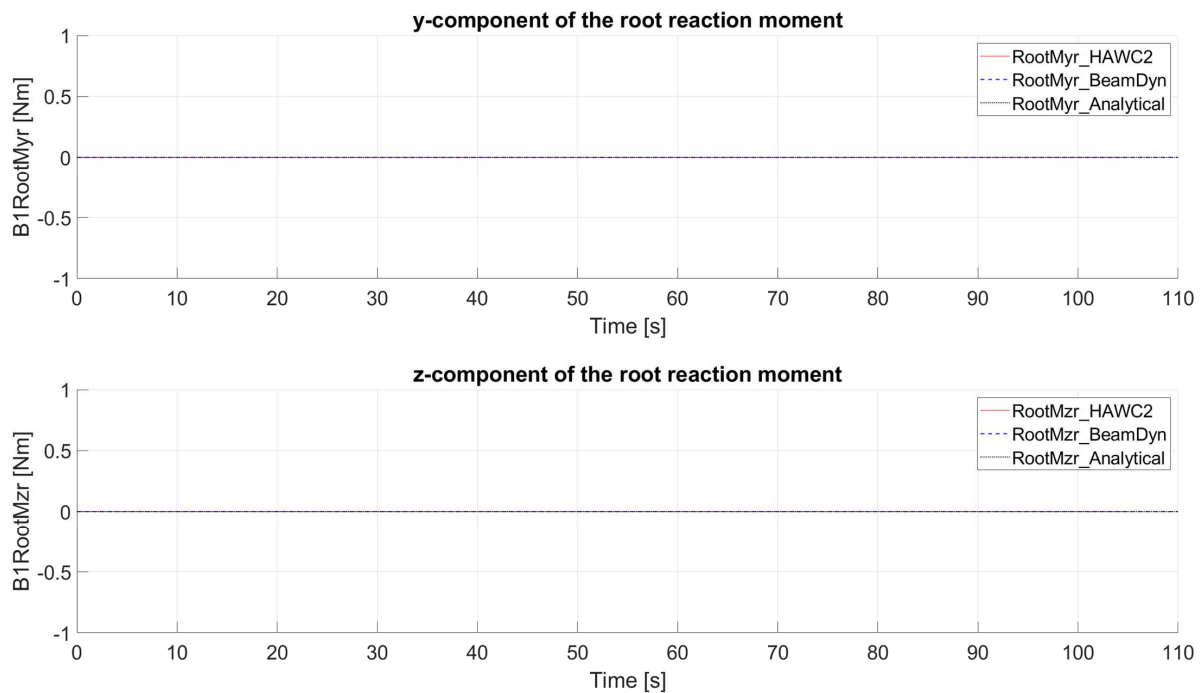
Figure 7. *Cont.*

Figure 7. Change in the charge state with a fixed rotational speed. Comparison of the x, y and z components of the analytical reaction forces at the fixed support (dotted black) with the simulated root reaction forces and moments from HAWC2 (red) and BeamDyn (blue dashed).
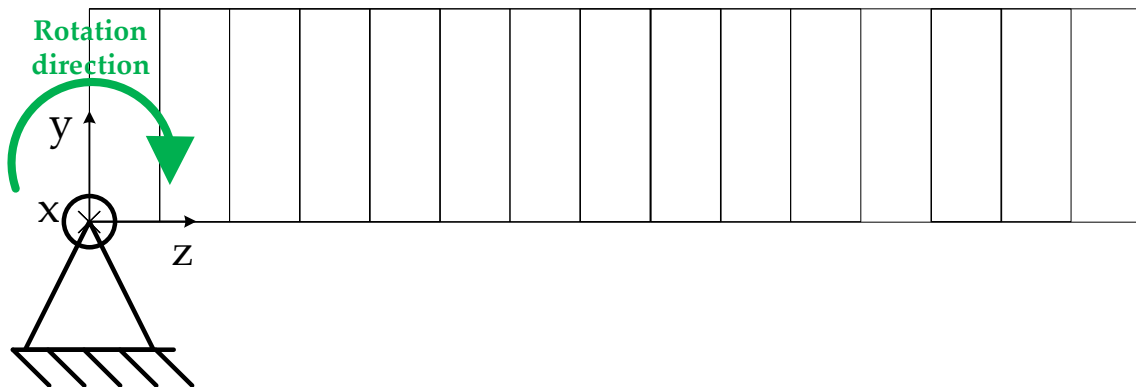
Pinned support, straight and stiff beam

Figure 8. Schematic drawing of a pinned support, straight and stiff beam.

3.3. Case 3: A Flexible and Initially Curved Beam

Rotor blades of wind turbines are manufactured from flexible composite materials using pre-bend or swept designs. Hence, the objective of Case 3 is to compare the ability of the modified HAWC2 and BeamDyn to simulate the variable inertia of flexible and initially curved beams. The geometry and the mechanical properties of the beam are shown in Tables 2 and 3.

Case 3 uses the same pinned support and the same simulation scenario used in Case 2. Figure 10b shows that the initial rotational speed of 10 rpm decreases and increases with the increase and decrease of the beam inertia, respectively. The vibration behavior of the beam (shown in Figure 10b) is identical in simulations in HAWC2 and BeamDyn. The angular momentum around the rotational axis of all elements is calculated and shown in Figure 10c. It shows that the total angular momentum is conserved even when local variations of angular velocities are produced by vibrations.
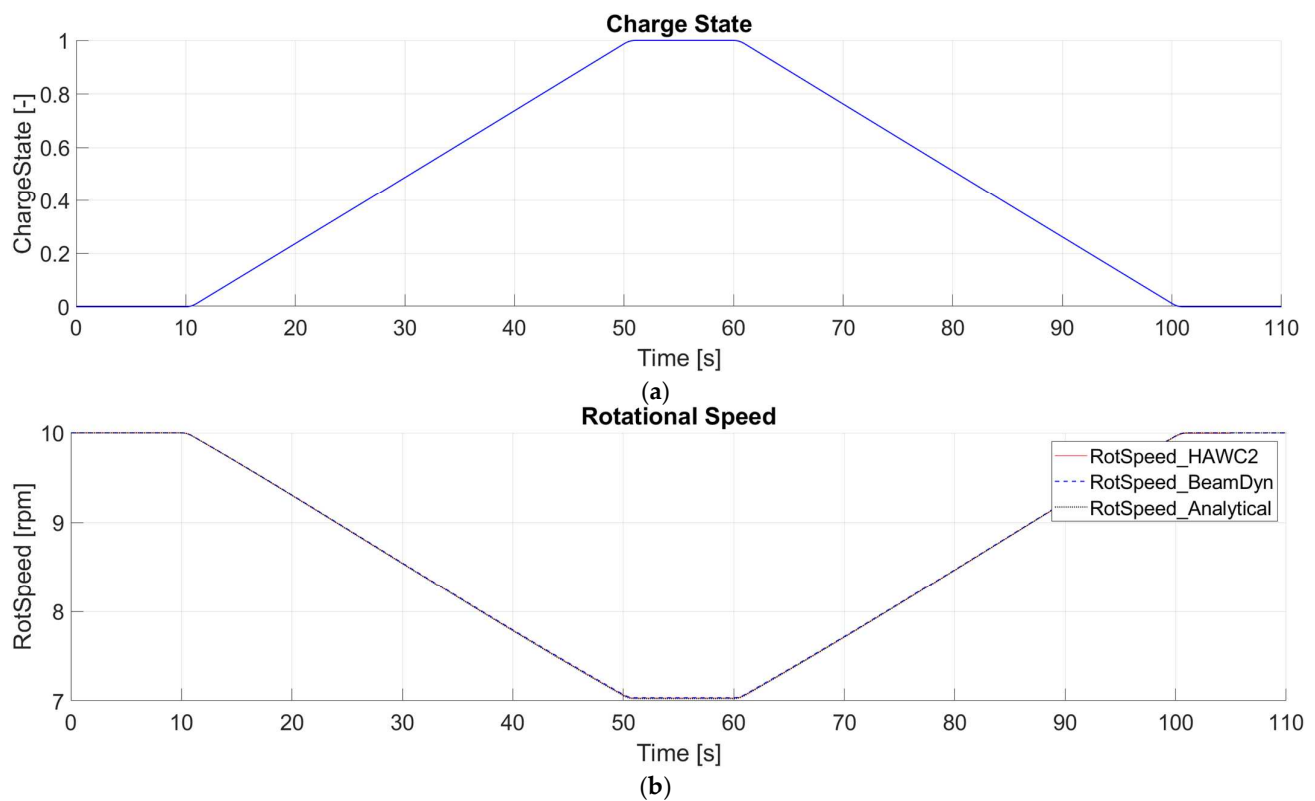
Figure 9. (**a**) Change in the charge state; (**b**) Comparison of the analytical rotational speed (dotted black) with the simulated rotational speed from HAWC2 (red) and BeamDyn (blue dashed) in a pinned-supported, straight and stiff beam.

Table 2. Coordinates of the unloaded beam, showing the pre-bending of the beam.

Section No.	x	y	z
-	m	m	m
1	0.00	0.00	0.00
2	0.00	0.01	1.00
3	0.00	0.04	2.00
4	0.00	0.09	3.00
5	0.00	0.16	4.00
6	0.00	0.25	5.00
7	0.00	0.56	7.50
8	0.00	1.00	10.00
9	0.00	1.21	11.00
10	0.00	1.44	12.00
11	0.00	1.69	13.00
12	0.00	1.96	14.00
13	0.00	2.25	15.00

Table 3. Cross-sectional mechanical properties of the flexible and curved beam.

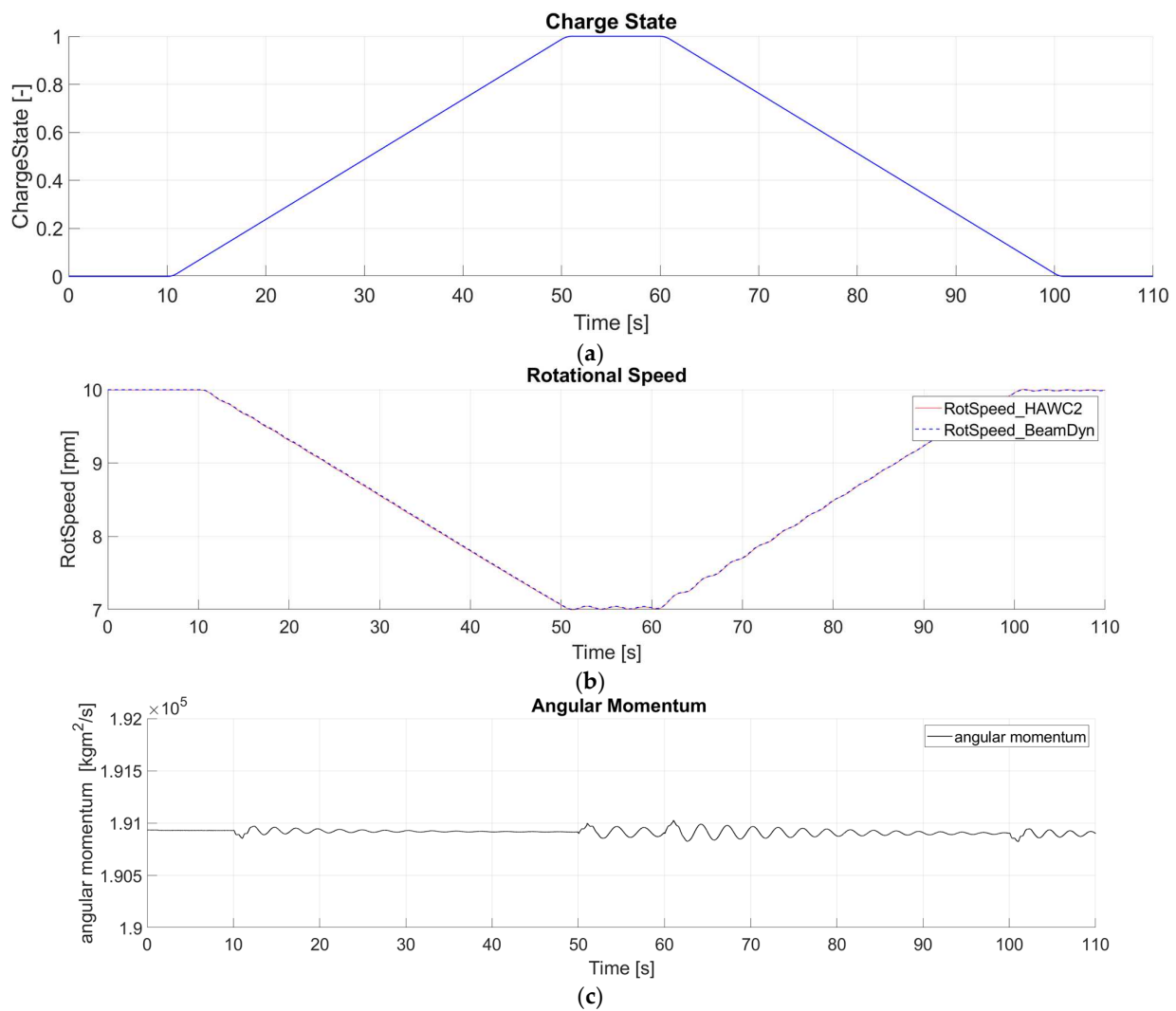| Beam Elemntmass Density	Flap and Edge Mass Moments of Inertia per Unit Span	Flap Stiffness	Edge Stiffness	Flap Shear Stiffness	Edge Shear Stiffness	Torsional Stiffness
kg/m	kg·m	N·m^2	N·m^2	N·m^2	N·m^2	N·m^2
50	50	1×10^6	1×10^6	5×10^8	5×10^8	1×10^9

Figure 10. (**a**) Change in the charge state; (**b**) Comparison of the simulated rotational speed from HAWC2 (red) and BeamDyn (blue dashed) in a free-supported, curved, and flexible beam; (**c**) Conservation of total rotational angular momentum (black) calculated from the results of the HAWC2 simulation.

4. Application of the Flywheel When the Wind Turbine Performs an Emergency Braking

Numerous functionalities of the flywheel can be applied to deal with various grid events and to reduce the mechanical loads on the structure of wind turbines [14]. These functionalities are developed via the First Eigenmodes simulation model [15]. However, as discussed in the introduction, this model is not suitable for evaluating the impact of the flywheel on the mechanical loads of WTs. Since the validation in Section 3 proved that the modified HAWC2 and BeamDyn models can simulate the dynamic behavior of the flywheel, these modified models can be used to analyze the stress reduction functionalities of the flywheel on wind turbine components.

Emergency braking is one of the most drastic events for a WT. It causes a significant burden on the support structures of the WT, especially on the tower bottom and foundation. A worst-case scenario, in which the wind turbine has to be brought to a standstill, is presented in the design load case (DLC) 2.3 in the IEC-61400-1 standards [33]. DLCs are simulation scenarios defined in wind turbine guidelines and used to verify wind turbine designs. DLC 2.3 is a combination of a significant wind event, i.e., extreme operation gust (EOG), with an internal or external electrical system fault, i.e., loss of electrical grid. According to the IEC-61400-1 standards, a study of several combinations of different wind speeds and times of grid loss events with respect to the EOG needs to be simulated to

determine which combination has the most critical effect on the simulated WT. Hence, a study was performed for different combination scenarios on the NREL 5 megawatt (MW) reference wind turbine [34]. The study showed that the combination of a rated wind speed of 11.6 m/s with a time of grid loss at the lowest wind speed in the EOG (see the event start in Figure 11a) had the greatest load effect on the wind turbine support structure. Based on this finding, DLC 2.3 is simulated initially in the original codes of HAWC2 and OpenFAST. Figure 11a,b shows that even when the wind speed, generator torque, and pitch control outputs from OpenFAST and HAWC2 are identical, the rotor speeds slightly deviate. This deviation is due to the differences in the implementation of the blade element momentum (BEM) theory in the aerodynamics models in HAWC2 [35] and OpenFAST [36]. Consequently, Figure 11c illustrates the difference in the aerodynamic torque values generated by HAWC2 and OpenFAST.

Since the aerodynamics models of HAWC2 and OpenFAST are not in the scope of the study presented in this paper, the difference in these aerodynamics models is not further investigated. However, to evaluate the effect of the flywheel on the 5 MW wind turbine without the effect of the difference in the aerodynamics models, two comparisons are presented in Figure 12: 5 MW wind turbine with and without flywheel in OpenFAST (Figure 12 right-hand side), and 5 MW wind turbine with and without flywheel in HAWC2 (Figure 12 left-hand side).

As the generator torque disappears due to the sudden grid loss, see Figure 11a, the wind turbine has to be brought to a standstill fast to avoid excessive overspeed. This is done by quickly pitching the blade to a feather position from 0° to 90°, see Figure 11b, i.e., aerodynamic emergency braking. However, the quick pitching at high rotor speeds leads to an increase in the mechanical loads on the wind turbine support structures. This can be seen in Figure 11d as an increase in the tower base fore-aft moment.

The flywheel can support the aerodynamic emergency breaking in the case of DLC 2.3 by charging the flywheel to reach its maximum charge state in all three blades, see Figure 12a,b. Charging the flywheel produces two decelerating torques: a mechanical decelerating torque resulting from the Coriolis forces, see Section 2.2.2, and an electrical decelerating torque at the generator by the electric pumps, see Figure 12c,d. The pumps support the charging process of the flywheel and draw their power from the wind turbine generator, even when the wind turbine is no longer connected to the grid. In this state of operation, the generator with its frequency converter and the motors of the pumps is an electric island. Figure 12c,d illustrates the damping effect of the flywheel mechanical decelerating torque on the out-of-plane blade tip deflection. Figure 12a,b shows that the rotor speed accelerates less when the flywheel is applied. The flywheel can decrease the tower base fore-aft moment by up to 12.5%, see Figure 12e,f.
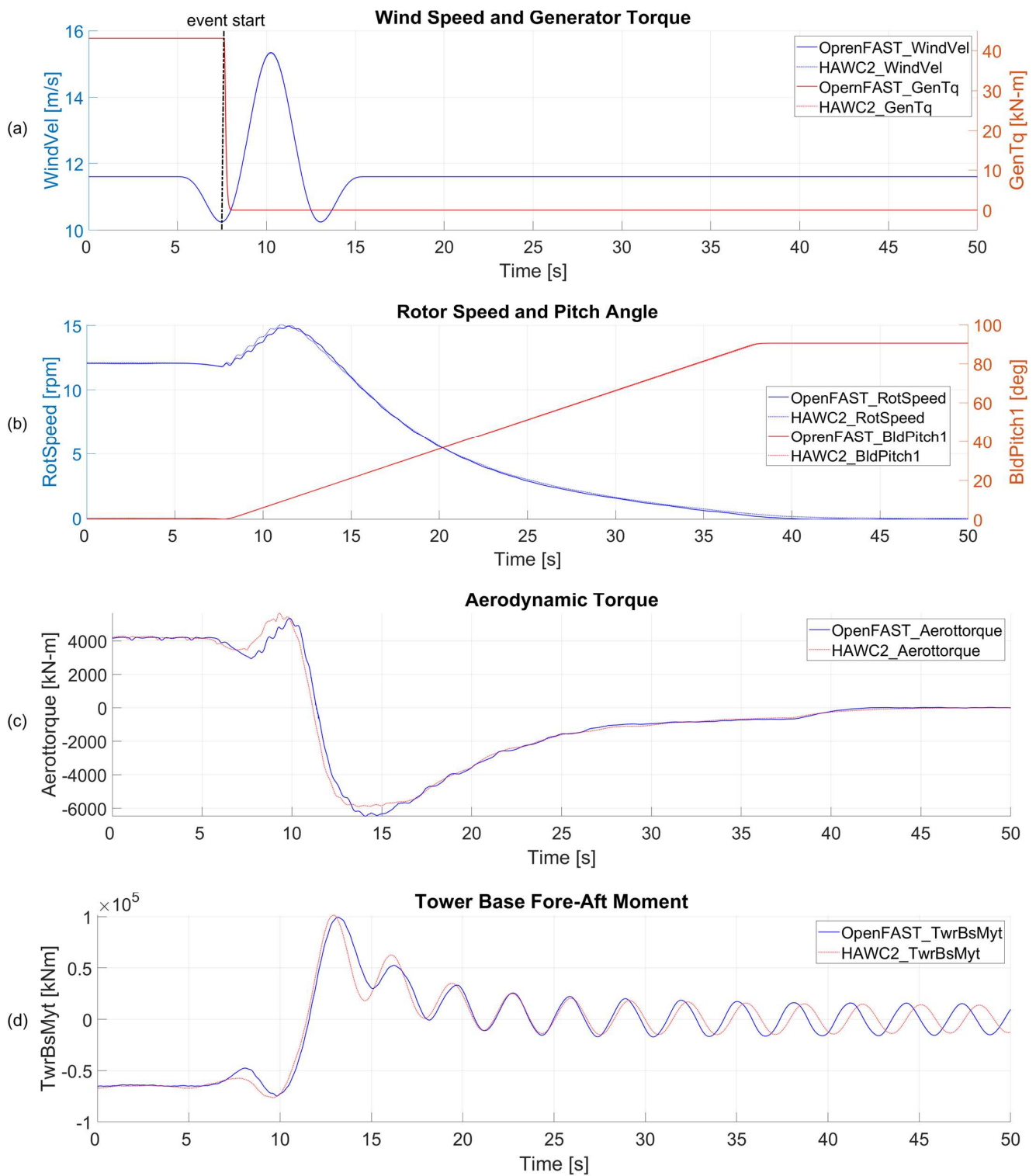
Figure 11. DLC 2.3 effect on a 5 MW reference wind turbine simulated with OpenFAST and HAWC2. (**a**) EOG with a rated wind speed of 11.6 m/s and grid loss at the lowest wind speed in the gust. (**b**) rotor speed and pitch angle. (**c**) aerodynamic torque. (**d**) the tower base fore-aft moment.
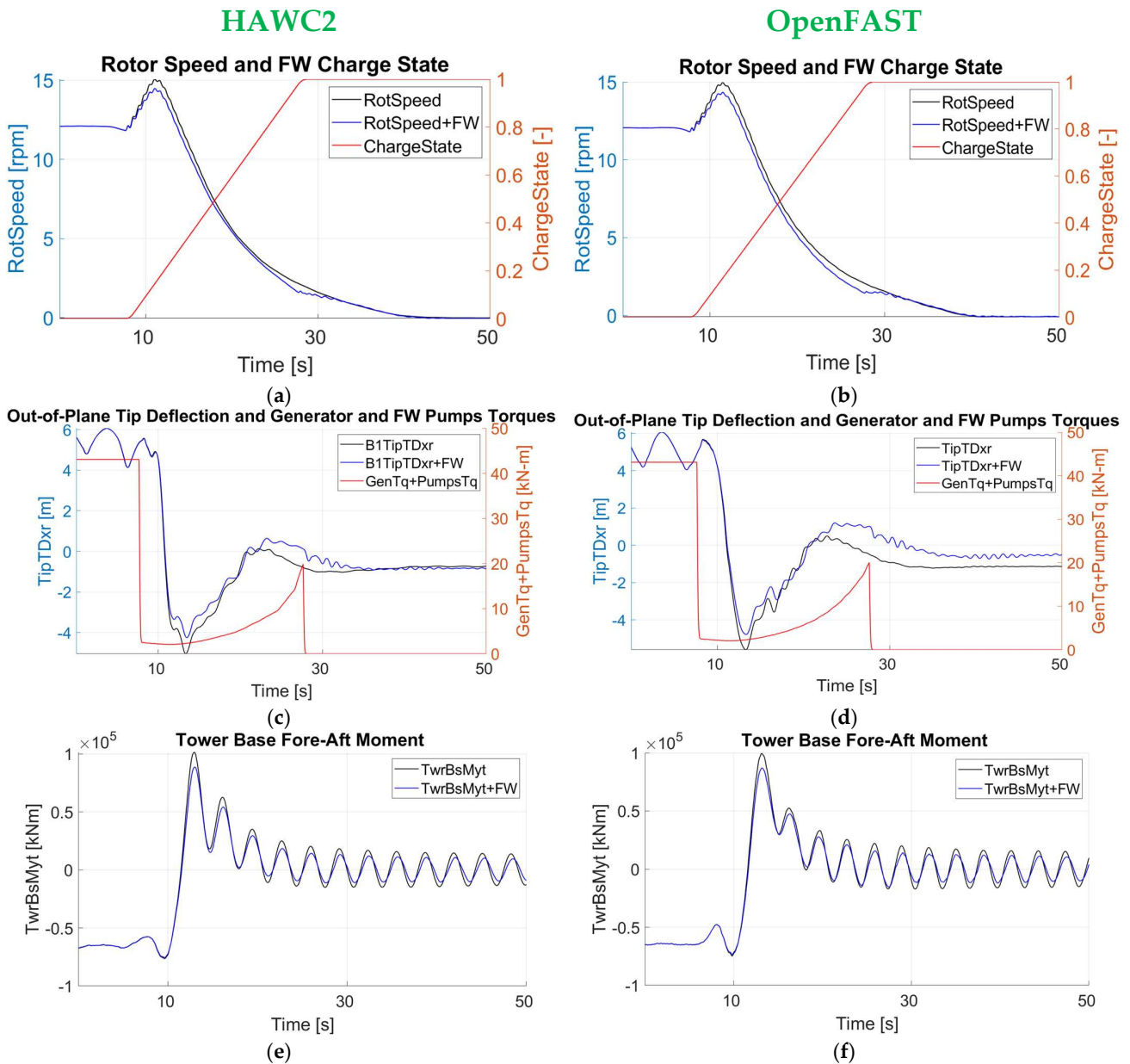
Figure 12. Comparison of the effect of DLC 2.3 on the 5 MW WT with flywheel (blue & red) and without flywheel (black) in OpenFAST and HAWC2. (**a**,**b**) rotational speed and charge state of the flywheel. (**c**,**d**) out-of-plane tip deflection and generator and flywheel pumps electrical torque. (**e**,**f**) tower base fore-aft bending moment.

5. Conclusions

Previous studies have investigated the effect of variable blade inertia on wind turbines using the First Eigenmodes simulation model [15] and the modified code of ElastoDyn [18]. The restrictions of these models and the simplified assumptions about the method used to implement variable blade inertia have necessitated an improvement to this method in more advanced structural dynamics models of wind turbine rotor blades. This paper presents a comparison, validation, and application of two improved methods to enable the structural dynamics models of HAWC2 and BeamDyn to simulate wind turbines with variable blade inertia. These two advanced models were developed to represent the nonlinear structural behavior of modern wind turbine composite blades. Hence, they are the ideal choice for representing the extended functionality of variable blade inertia presented in this paper.

This paper focuses on the variation of the blade inertia from the application of flywheels in wind turbine rotors. Two methods were developed to be implemented in HAWC2 and BeamDyn. These methods were validated based on three benchmarking cases of increasing complexity. The validation showed very good agreement between BeamDyn, HAWC2, and analytical calculations for all three cases.

Simulating the application of the flywheel in the rotor blades of the NREL 5 MW reference wind turbine when it is subject to DLC 2.3 shows that the flywheel reduces the tower base fore-aft bending moment by 12%. This result can be yielded with both HAWC2 and OpenFAST. With the variable blade inertia, the simulated effect of the flywheel shows good agreement between HAWC2 and OpenFAST in the rotor blade motions, e.g., the rotor speed and the out-of-plane motion, as well as in the tower base torque.

The focus of the current research project is on the enhancement of HAWC2 and BeamDyn to simulate wind turbines with hydraulic-pneumatic flywheels. Since this paper shows that this goal is achieved, future work will focus on the applications of these tools to simulate different wind turbine types with flywheels.

Data Availability Statement: The modified source code of BeamDyn is available online on ResearchGate https://www.researchgate.net/profile/Laurence-Alhrshy-2 (accessed on 16 August 2023). The External Systems generated by AEROVIDE GmbH are no self-contained programs but can only be used in combination with HAWC2, which is a commercial and not open-source software. Therefore, and due to AEROVIDE's competitive interests, the source code of the External System cannot be published. However, the raw data of the simulation results presented in this paper, with full-time series from HAWC2 and BeamDyn, are also available ResearchGate. These time series contain many additional signals which are not contained in this paper.

Conflicts of Interest: The author declares no conflict of interest.

References

1. Smart Blades. Available online: https://www.iwes.fraunhofer.de/en/press/archive-2016/smart-blades{-}{-}new-ideas-for-making-rotor-blades-more-stable-and-0.html (accessed on 30 January 2023).
2. Jauch, C.; Hippel, S. Hydraulic–Pneumatic Flywheel System in a Wind Turbine Rotor for Inertia Control. *IET Renew. Power Gener.* **2016**, *10*, 33–41. [CrossRef]
3. Lackner, M.A.; Rotea, M.A. Passive Structural Control of Offshore Wind Turbines. *Wind Energy* **2011**, *14*, 373–388. [CrossRef]
4. Hudecz, A.; Koss, H.; Hansen, M.O.L. Ice Accretion on Wind Turbine Blades. In Proceedings of the 15th International Workshop on Atmospheric Icing of Structures (IWAIS XV), St. John's, NL, Canada, 8–11 September 2013.
5. Jauch, C. Grid Services and Stress Reduction with a Flywheel in the Rotor of a Wind Turbine. *Energies* **2021**, *14*, 2556. [CrossRef]
6. Jauch, C. A Flywheel in a Wind Turbine Rotor for Inertia Control. *Wind Energy* **2015**, *18*, 1645–1656. [CrossRef]
7. Hippel, S.; Jauch, C. Hydraulic-Pneumatic Energy Storage in a Wind Turbine for Enhancing the Power System Inertia. In Proceedings of the 13th Wind Integration Workshop, Berlin/Heidelberg, Germany, 11–13 November 2014.
8. Jauch, C. Controls of a Flywheel in a Wind Turbine Rotor. *Wind Eng.* **2016**, *40*, 173–185. [CrossRef]
9. Alhrshy, L.; Jauch, C.; Bünning, N.; Schaffarczyk, A. *Development of a Lightweight Hydraulic-Pneumatic Flywheel System for Wind Turbine Rotors*; Wind Energy Technology Institute: Flensburg, Germany, 2021. [CrossRef]
10. Lackner, M.A.; Rotea, M.A. Structural Control of Floating Wind Turbines. *Mechatronics* **2011**, *21*, 704–719. [CrossRef]
11. Active Structural Control with Actuator Dynamics on a Floating Wind Turbine. Available online: https://arc.aiaa.org/doi/10.2514/6.2013-455 (accessed on 15 March 2023).
12. Stewart, G.; Lackner, M. Offshore Wind Turbine Load Reduction Employing Optimal Passive Tuned Mass Damping Systems. *IEEE Trans. Control. Syst. Technol.* **2013**, *21*, 1090–1104. [CrossRef]

13. Stewart, G.M.; Lackner, M.A. The Effect of Actuator Dynamics on Active Structural Control of Offshore Wind Turbines. *Eng. Struct.* **2011**, *33*, 1807–1816. [CrossRef]

14. Stewart, G.M.; Lackner, M.A. The Impact of Passive Tuned Mass Dampers and Wind–Wave Misalignment on Offshore Wind Turbine Loads. *Eng. Struct.* **2014**, *73*, 54–61. [CrossRef]

15. Jauch, C. *First Eigenmodes Simulation Model of a Wind Turbine—For Control Algorithm Design*; Wind Energy Technology Institute: Flensburg, Germany, 2020. [CrossRef]

16. 4.2.7. ElastoDyn Users Guide and Theory Manual—OpenFAST v3.4.1 Documentation. Available online: https://openfast.readthedocs.io/en/main/source/user/elastodyn/index.html#elastodyn-users-guide-and-theory-manual (accessed on 28 March 2023).

17. Jonkman, J. The New Modularization Framework for the FAST Wind Turbine CAE Tool. In Proceedings of the 51st AIAA Aerospace Sciences Meeting Including the New Horizons Forum and Aerospace Exposition, American Institute of Aeronautics and Astronautics: Grapevine (Dallas/Ft. Worth Region), Grapevine, TX, USA, 7–10 January 2013.

18. Alhrshy, L. Implementation of Variable Blade Inertia in OpenFAST to Integrate a Flywheel System in the Rotor of a Wind Turbine. *Energies* **2021**, *14*, 2783. [CrossRef]

19. Kane, T.R.; Levinson, D.A. *Dynamics, Theory and Applications*; McGraw Hill: New York, NY, USA, 1985; ISBN 978-0-07-037846-9.

20. Larsen, T.J.; Hansen, A.M. How 2 HAWC2, the User's Manual. Available online: https://tools.windenergy.dtu.dk/HAWC2/manual/How2HAWC2_12_9.pdf (accessed on 16 August 2023).

21. Wang, Q.; Sprague, M.A.; Jonkman, J.; Johnson, N.; Jonkman, B. BeamDyn: A High-Fidelity Wind Turbine Blade Solver in the FAST Modular Framework. *Wind Energy* **2017**, *20*, 1439–1462. [CrossRef]

22. Pavese, C.; Kim, T.; Energy, D.W. *HAWC2 and BeamDyn: Comparison between Beam Structural Models for Aero-Servo-Elastic Frameworks*; National Renewable Energy Lab. (NREL): Golden, CO, USA, 2016.

23. Shabana, A.A. *Dynamics of Multibody Systems*, 1st ed.; Cambridge University Press: Cambridge, UK, 2020; ISBN 978-1-108-75755-3.

24. Hansen, A.M.; Larsen, T.J. Gear Dynamics. In *Research in Aeroelasticity EFP-2007-II*; Danmarks Tekniske Universitet, Risø Nationallaboratoriet for Bæredygtig Energi: Lyngby, Denmark, 2009; pp. 134–142.

25. Featherstone, R. Contact, Impact, and Kinematic Loops. In *Robot Dynamics Algorithms*; Featherstone, R., Ed.; The Springer International Series in Engineering and Computer Science; Springer: Boston, MA, USA, 1987; pp. 153–195. ISBN 978-0-387-74315-8.

26. Hodges, D.H. *Nonlinear Composite Beam Theory*; Progress in astronautics and aeronautics; American Institute of Aeronautics and Astronautics: Reston, VA, USA, 2006; ISBN 978-1-56347-832-1.

27. Patera, A.T. A Spectral Element Method for Fluid Dynamics: Laminar Flow in a Channel Expansion. *J. Comput. Phys.* **1984**, *54*, 468–488. [CrossRef]

28. Bauchau, O.A.; Epple, A.; Heo, S. Interpolation of Finite Rotations in Flexible Multi-Body Dynamics Simulations. *Proc. Inst. Mech. Eng. Part K J. Multi-Body Dyn.* **2008**, *222*, 353–366. [CrossRef]

29. Wang, Q.; Yu, W. Geometrically Nonlinear Analysis of Composite Beams Using Wiener-Milenković Parameters. *J. Renew. Sustain. Energy* **2017**, *9*, 033306. [CrossRef]

30. What Is an S-Function?—MATLAB & Simulink—MathWorks Deutschland. Available online: https://de.mathworks.com/help/simulink/sfg/what-is-an-s-function.html (accessed on 26 June 2023).

31. Write Level-2 MATLAB S-Functions—MATLAB & Simulink—MathWorks Deutschland. Available online: https://de.mathworks.com/help/simulink/sfg/writing-level-2-matlab-s-functions.html (accessed on 26 June 2023).

32. Jonkman, J.M.; Buhl, M.L., Jr. *FAST User's Guide—Updated August 2005*; No. NREL/TP-500-38230; National Renewable Energy Lab. (NREL): Golden, CO, USA, 2005; p. 15020796.

33. IEC 61400-1:2019 RLV | IEC Webstore | Rural Electrification, Wind Power. Available online: https://webstore.iec.ch/publication/64648 (accessed on 12 June 2023).

34. Jonkman, J.; Butterfield, S.; Musial, W.; Scott, G. *Definition of a 5-MW Reference Wind Turbine for Offshore System Development*; National Renewable Energy Lab. (NREL): Golden, CO, USA, 2009; Volume 75. [CrossRef]

35. Madsen, H.A.; Larsen, T.J.; Pirrung, G.R.; Li, A.; Zahle, F. Implementation of the Blade Element Momentum Model on a Polar Grid and Its Aeroelastic Load Impact. *Wind Energy Sci.* **2020**, *5*, 1–27. [CrossRef]

36. Jonkman, J.M.; Hayman, G.J.; Jonkman, B.J.; Damiani, R.R.; Murray, R.E. AeroDyn V15 User's Guide and Theory Manual. *Renew. Energy* **2015**, 46.